# Shrinkage Of Alkali-Activated Slag: Mitigation Techniques

Wala'a Al Makhadmeh

A Thesis

In the Department

of

Building, Civil and Environmental Engineering

Presented in Partial Fulfillment of the Requirements

For the Degree of

Doctor of Philosophy (Civil Engineering) at

Concordia University

Montreal, Quebec, Canada

July 2021

**CONCORDIA UNIVERSITY**

**SCHOOL OF GRADUATE STUDIES**

This is to certify that the thesis prepared.

By: Wala'a Al Makhadmeh

Entitled: Shrinkage of Alkali-Activated Slag: Mitigation Techniques

and submitted in partial fulfillment of the requirements for the degree of

DOCTOR OF PHILOSOPHY (Civil Engineering)

complies with the regulations of the University and meets the accepted standards with respect to originality and quality.

Signed by the examining committee:

Dr. Arash Mohammadi ——————————————Chair

Dr. Shahria Alam ——————————————— External Examiner

Dr. Lyes Kadem——————————————————External to Program

Dr. Michelle Nokken——————————————————Examiner

Dr. Chunjiang An——————————————————Examiner

Dr. Ahmed Soliman——————————————————Thesis Supervisor

Approved by ——————————————————————

Dr. Michelle Nokken, Graduate Program Director

July 23, 2021

_____

Dr. Mourad Debbabi, Dean
Gina Cody School of Engineering and Computer Science

# ABSTRACT

**Shrinkage Of Alkali-Activated Slag: Mitigation Techniques**

**Wala'a Al Makhadmeh, Ph.D.**

**Concordia University, 2021**

This thesis presents a simultaneous investigation of the autogenous and total drying shrinkage behavior of Alkali-activated slag (AAS) as a binder. AAS binders are receiving global interest as a potentially sustainable alternative binding material due to their environmental benefits, impressive mechanical properties performance, and non-heat curing requirement. However, high shrinkage and cracking tendencies are hindering the effectiveness of AAS binders and are the main obstacles that must be addressed before widespread use.

This dissertation addresses the substantial shrinkage in the AAS system by simultaneously investigating the autogenous and total drying shrinkage behavior of AAS. Applying three main mitigation strategies, this research presents novel findings to which show significant reductions in AAS's shrinkage. Firstly, the effect of activator nature on shrinkage was studied, which highlighted the sensitivity of AAS systems to various levels of silicate modulus (Ms) and sodium oxide ($Na_2O$%).

The findings highlighted the critical interactions between AAS pore solution compositions and shrinkage-reducing admixture (SRA) efficiencies as a shrinkage mitigation technique. Overall, a 62% and 41% reduction in the measured autogenous and total drying shrinkage were acheived, respectively.

The second mitigation strategy is the internal curing of AAS by superabsorbent polymers (SAPs). Specifically, the influence of SAPs on reaction kinetics, pore structure, and microstructure of AAS was studied based upon the SAPs desorption kinetics (i.e., concentrations and release timing). SAPs significantly mitigated the autogenous and total drying shrinkage up to 90% and 30%, respectively.

Finally, the third strategy combines the benefits of both SRAs and SAPs to address the shrinkage behavior of AAS. At the time of submission, this combination approach has not been investigated to the best of our knowledge. This novel approach investigated the potential interactions between SRA molecules and SAPs networks, yielding enhancement in mitigation of the total drying shrinkage by around 69%. This effect is attributed to the comprehensive influence of both the surface tension and internal relative humidity.

# ACKNOWLEDGMENT

All praise and thanks are due to “ALLAH” for giving me the patience and perseverance to accomplish my Ph.D.

Dedicated To:

The soul of my Father (may Allah Almighty bless him) who left us three weeks ago.

**DADDY** …. I did it, as you wished, but success doesn’t have a taste without you.

To my beloved Mother who is always there for me and without her unconditional love and care I would never have made it.

I thank the person who enlightens my life, day after day, my husband, Tariq. I could not have asked for a better soul mate than him. Tariq has been giving all his love and sacrifice to support me. I also wish to acknowledge my Kids, Sarah, Salma, and Karam who were the motivation for me to complete this research. I won’t forget to thank my sister and brothers, for being ever-present with their love and constant encouragement. Their support was invaluable in completing this thesis. I also thank my third family.

I thank my thesis supervisor, Dr. Ahmed Soliman, for his continuous support and valuable advice for the past four years. Thank you for being a great guide and motivator, and for your ever-caring attitude. Through thick and thin, you have always given me your full support, for which I will always be grateful.

Finally, I am also indebted to the juror's committee members and chair of my examinations committee, namely Dr. Shahria Alam, Dr. Michelle Nokken, Dr. Lyes Kadem, and Dr. Chunjiang An

**Wala’a Almakhadmeh, June 2021, Montreal, Canada**

# Table of Contents

## LIST OF FIGURES

# LIST OF TABLES

## LIST OF ABBREVIATIONS

| Term | Explanation |
|---|---|
| (AAMs) | Alkali activated materials |
| (AAS) | Alkali activated slag |
| (AFm) | Alumina, ferric oxide, mono-sulfate |
| (Aft) | Alumina, ferric oxide, tri-sulfate |
| (CAO) | Calcium Oxide |
| (C-A-S-H) | Calcium-alumino-silicate-hydrate |
| (C-S-H) | Calcium-silicate-hydrate |
| (EA) | Expansive agent |
| (FA) | Fly ash |
| (HT) | Hydrotalcite |
| (LWA) | Lightweight aggregate |
| (Ms) | Activator modulus |
| (N-A-S-H) | Alkali- alumino-silicate- hydrate |
| (OPC) | Ordinary Portland cement |
| (RH) | Relative humidity |
| (SF) | Silica Fume |
| (BET) | Brunauer, Emmett, and Teller |
| (IRH) | Internal relative humidity |
| (NMR) | Nuclear magnetic resonance |
| (SAP) | Superabsorbent polymers |
| (SRA) | Shrinkage reducing admixture |
| (TGA) | Thermogravimetric analysis |
| (XRD) | X-ray diffraction |

# Chapter 1 - Introduction

As the planet goes through unprecedented changes caused by global warming, a consistent offender to climate change has consistently been greenhouse gas (GHG) emissions. As the concentration of GHG increases in the atmosphere, so does the temperature. Interestingly, a major contributor to greenhouse gas emissions is cement manufacturing, which is responsible for 5 to 7% of total global greenhouse gas emissions (Ye, and Radlinska, 2016a). There is a clear necessity to find an alternative, more environmentally friendly option to reduce the GHG emissions and the environmental impact of the cement industry. One clear option to reduce the environmental impact of cement manufacturing would be to use an alternative binder, such as alkali-activated materials (AAM) (Pacheco-Torgal et al., 2008). Alkali-activated materials utilize industrial waste materials, which leads to both economic and environmental benefits (Davidovits, 1989) by reducing the need to manufacture new binding components. It is mainly composed of alkali activating agents mixed with a calcium-rich precursor (e.g., Ground granulated blast furnace slag (GGBS)) or alumina abundant precursor (e.g., Class F fly ash and metakaolin).

Alkali-activated slag (AAS) is one of the most common types of AAM. Ground-granulated blast-furnace slag (GGBS) is considered a calcium-rich aluminosilicate precursor in alkali-activated materials (Luukkonen et al., 2018), and it is a by-product of pig iron manufacturing consisting of the silicate and aluminate impurities that exist in the iron coke. AAS is formed by activating the aluminosilicate powders in the GGBS, resulting in different types of amorphous phases including calcium-silicate-hydrate (C-S-H) and calcium-aluminosilicate-hydrate (C-A-S-H), which cause the binding characteristics (Ben Haha et al., 2011; Ye and Radlinska, 2016b). Generally, the efficiency of the binder activation process depends on the type of activator and its pH value, which controls the degree of hydration and product formation (Puertas et al., 2004). Liquid sodium silicate solution is the preferred activator in AAS systems due to its high compressive strength (Wang et al., 1994). In comparison to OPC, AAS concrete has a very high compressive strength (up to 130 MPa) and superior durability against acid, sulfate, and fire attacks (Sarker et al., 2014).

Although many activators had been used to activate GGBS, a mix of sodium silicate and sodium hydroxide (waterglass) showed promising mechanical properties (Fernandez-Jimenez et al., 2007). The reactivity of this activator is mainly controlled by the sodium oxide content ($Na_2O$%) and activator modulus (Ms). The sodium oxide content reflects the ratio of sodium oxide in the activator to the binder by weight, while Ms is the ratio of silicon oxide to sodium oxide ($SiO_2$/ $Na_2O$) (Atis et al., 2009).

Shrinkage is an important property in alkali-activated slag systems input as a concrete binder as it can impact the durability of concrete by inducing cracks (Bakharev et al. 1999). It has been a major limitation in their wider application in the construction industry. The common types of shrinkage are chemical, autogenous, drying and carbonation shrinkage (Ye and Radlińska, 2007). The cracking of AAS concrete is highly related to the autogenous and drying shrinkage, where the autogenous shrinkage is more linked to chemical shrinkage and self desiccation (Collins and Sanjayan, 1999). Both autogenous and drying shrinkage phenomena are related to water loss inside the AAS system, either through self desiccation or by evaporation (Neto et al., 2008). Studies attributed this high shrinkage to the higher capillary pressure, finer pore size distribution, lower stiffness of AAS, and a higher degree of saturation than the OPC system (Cartwright et al., 2015; Neto et al., 2008). Moreover, the hydrated calcium silicate gel's characteristics had an important effect on the shrinkage of AAS (Chen et al., 2021; Ye and Radlińska, 2016b).

The main hydration products in the AAS system are C-A-S-H with a low calcium/ silica ratio (C/S) than that formed in OPC systems. This kind of C-A-S-H is less stable and experiences more intense syneresis, which tends to shrink more under capillary pressure (Chen et al., 2021; Hu et al., 2019; Kutti, 1992). Different shrinkage mitigation strategies have been proposed to reduce the substantial shrinkage strains in AAS systems, namely internal curing, heat curing, and shrinkage reducing admixtures (Kumarappa et al., 2018; Bakharev et al., 1999). Internal curing is a common process that can mitigate the autogenous shrinkage by including a saturated porous agent (i.e., saturated lightweight aggregate or superabsorbent polymer) during the mixing process (Bentz and Snyder, 1999). As reported by Ye and Radlińska (2017) and Bakharev et al. (1999), high-temperature curing (60–80 °C) was effective in reducing the drying shrinkage of AAS systems. This technique may also be sufficient to mitigate the autogenous shrinkage since the C-A-S-H gels become more stable at higher curing temperatures (Ye and Radlińska, 2017).

However, heat curing requires additional energy consumption, and in terms of energy cost to benefit, these curing methods are impractical in-situ.

The shrinkage behavior of AAS and applied mitigation techniques have been well researched and reported. However, limited studies have been done to assess the effect of shrinkage-reducing admixtures (Kumarappa et al., 2018; Palacios and Puertas, 2007) and superabsorbent polymer on the AAS systems (Song and Choi 2016; Oh and Choi 2018). Hence, understanding the working mechanism of these techniques can contribute to maximizing the benefits of their usage in AAS to achieve adequate shrinkage performance, thereby reducing the environmental impact of this binding process.

### 1.1 Problem definition

A major contributor to greenhouse gas emissions is cement manufacturing, which is responsible for 5 to 7% of total global greenhouse gas emissions (Ye, and Radlinska, 2016a). There is a clear necessity to find an alternative, more environmentally friendly option to reduce the GHG emissions and the environmental impact of the cement industry. Furthermore, the energy inputs for the cement manufacturing supply chain account for 58% of the total cost production (Lang, 1993). The calcination (decarbonization) of limestone at 1400–1450 °C contributes around 50–60% of OPC-production-related $CO_2$ emissions, which may not be affected by improving energy efficiency (Damtoft *et al*. 2012). Additionally, millions of tons of blast-furnace slag (i.e., pig iron manufacturing) and other by-products have been generated annually. The reuse and recycling of these industrial by-products is a vital need to remove them from landfills. According to a life cycle assessment study, AAS concrete can considerably reduce the environmental impacts of concrete products by lowering emissions by 73% (GHGs) and a reduction of 43% in energy demand compared to that in OPC concrete (Jiang et al., 2014).

Generally, AAS systems have major challenges in shrinkage and insufficient durability against shrinkage and micro-cracking. Studies reported that AAS experiences high autogenous, and drying shrinkage can be 4-6 times greater than OPC (Ye and Radlińska 2017; Palacios and Puertas 2007). This means that the substantial autogenous or drying shrinkage creates significant cracking risks for AAS. Once a crack is formed, the effect is compounded as these cracks can serve as paths for salts/gas ingression, which further impacts its durability.

This can be overcome by understanding the shrinkage mechanisms in AAS and the strategies to mitigate it. The goal of this work is to understand and assess the efficiency of the shrinkage mitigation techniques for AAS systems.

## 1.2 Motivations and Objectives

The motivation of this research comes from clearly seeing the environmental benefits of using AAS as a binding material in cementitious materials. This research is motivated by increasing the efficiency of the manufacturing of cementitious materials and alternative binders, which thereby reduces the environmental impact.

Waterglass activators are used in this work, and it is controlled by two parameters that have a great influence on the shrinkage of AAS, namely the alkali dosage ($Na_2O$%) and the silicate modulus (Ms). Interestingly, the effect of $Na_2O$% and Ms on the autogenous and drying shrinkage of AAS mortars is still under debate. Therefore, part of this dissertation aims to understand the influence of different levels of $Na_2O$% and Ms on the autogenous and drying shrinkage of AAS. Furthermore, an experimental approach was used to account for the sensitivity of AAS property to various levels of Ms and $Na_2O$%. While the results of this study provided vital insight for the sensitivity of AAS property to various levels of Ms and $Na_2O$%, additional research and a comprehensive study is needed to further understand the significance of each parameter and how the activator controls the properties of AAS, especially the shrinkage and compressive strength. This analysis would help in choosing the appropriate levels of both $Na_2O$% and Ms for further research.

Shrinkage-reducing admixtures (SRAs) have been proved to be effective in mitigating the autogenous shrinkage of AAS. SRAs are organic materials that belong to surface-active agents (surfactants). Particularly, the basic behavior of SRAs in an AAS pore solution should be considered and the impact on the surface tension with various SRA dosages should be characterized. The interactions of shrinkage-reducing admixtures and their behavior in alkali-activated slag systems will be further understood through this dissertation. Furthermore, this research will provide a fundamental understanding of the SRA effect on the basic mechanisms of

hydration, which is related to the impact on the shrinkage of AAS. The following investigations steps constitute the objective of the dissertation:

1. As the alkali activation of slag starts, the ions start to dissolve gradually from slag particles. SRA can affect the cations/anions concentrations in the pore solution which can contribute to the strength development reduction rate. Hence, revealing how SRA can impact the alkalinity of the pore solution would be the main objective of this dissertation.
2. There is a knowledge gap for the change of the surface tension in the pore solution of AAS paste when used as a function of SRA dosage. Therefore, it is imperative to identify the critical bulk concentration (CMC) in AAS pore solution at which the surface tension virtually remains constant, identified as a limit for shrinkage reduction.
3. The effectiveness of shrinkage-reducing admixtures in mitigating the autogenous shrinkage of AAS mortars will be evaluated based on the various dosages of SRA. This thesis contributes to the optimized SRA dosage in AAS mixtures.
4. Investigating the impact of SRA on the hydrated phase assemblage and microstructure of AAS, that is considered a crucial need towards having fair discrimination between SRA main and side effects on AAS shrinkage. A deep and comprehensive understanding of the working mechanism of SRA can help in optimizing the SRA concentration in the AAS system.

Recently, superabsorbent polymers (SAPs) have been considered as straightforward internal curing (IC) methods and performance tests on AAS systems proved the efficiency of SAPs in restraining the autogenous shrinkage (Oh and Choi, 2018). The present work aims to shed light on the SAP role in the AAS system focusing on the following objectives:

1. SAPs have different absorption capacities depending on the liquid chemical characteristics. This dissertation will examine the absorption/desorption mechanisms of SAP in AAS pastes, or more specifically, the desorption kinetics of SAP during sealed AAS hydration
2. This dissertation reveals the interaction tendency of SAPs with the extracted AAS pore solution which contains a significant concentration of divalent cations.

3. The role of internal curing water entrained by SAP differs from the role of adding free mixing water. Thus, specific emphasis to highlight the effects of the internal curing entrained by SAPs, by contrast with additional free mixing water on AAS properties, is another important objective.
4. SAPs are reported to maintain the internal humidity (IRH) level inside the matrix. Therefore, examining the impact of various SAP contents/concentrations on the IRH and autogenous phenomena is important to specify the optimal SAP content that provides near-saturated conditions to the AAS.
5. In more arid regions, the relative humidity is usually around 40%-50% and water evaporation is expected to reduce the moisture inside the AAS concrete, particularly in the outer layer. This dissertation focuses on understanding the impacts of poor dry conditions on AAS properties, mainly the effects of SAP on AAS shrinkage and the pore structure of AAS. This work highlights the applicability of SAPs internal cured AAS systems under drying conditions and allowing for optimizing the optimal dosage of SAPs in AAS.

Shrinkage-reducing admixtures (SRAs) and superabsorbent polymer (SAP) were utilized individually to mitigate the shrinkage of AAS. Each strategy exhibits a different role in mitigating the shrinkage of AAS. Internally cured AAS by SAPs has finely distributed water reservoirs, which would help in keeping the matrix humid, yielding a lower amount of shrinkage. Also, SRA can effectively reduce the surface tension of AAS pore solution, which results in lower capillary tension. Therefore, it is hypothesized that the co-existence of both SRA and SAP could be beneficial and compensate for the drawbacks of each technique. More specifically, this dissertation shall:

1. Examine the synergistic effect of SAP and SRA in AAS by incorporating a hybrid system of both strategies. The synergistic effect of both techniques may reduce the impact of SAP on the properties of AAS.
2. SRA is classified as an amphiphilic compound consisting of a polar functional group (i.e. a hydrophilic head) connected to a non-polar hydrocarbon chain (i.e., a hydrophobic tail). Therefore, one of the main concerns is the potential interaction expected between

the SRA and SAPs polymeric networks. This work shall examine the effect of the interactions between SAPs and SRA and how can this interaction influence the main role of each of them.

3. In this hybrid SAP-SRA system, it is anticipated that combining both SRA and SAP will prove to be more beneficial and helps in reaching the goal of decreasing the AAS shrinkage to a level of that in OPC which contributes to a broader application of AAS.

## 1.3 Thesis organization

Shrinkage and micro-cracking of alkali-activated slag (AAS) can affect the durability of concrete significantly. This dissertation provides a comprehensive understanding of basic shrinkage mechanisms, shrinking mitigation techniques, and the physical impact of shrinkage for AAS. Attaining and understanding beneficial enhancement techniques allow the development of optimum designs for this AAS application. The dissertation provides comprehensive coverage of the mentioned research targets through eight chapters.

**Chapter 1** presents the problem definition and the research objectives.

**Chapter 2** shows comprehensive data on the shrinkage mechanisms of AAS, the factors affecting AAS shrinkage behavior, and the applied mitigation strategies to enhance performance.

**Chapter 3** presents the used materials, preparation of specimens, testing, and analytical methods that have been conducted in this thesis.

**Chapter 4** clarifies the influence of waterglass parameters ($Na_2O$% and Ms) and the significance of each parameter, as well as how the activator controls the properties of AAS. Statistical analysis was performed to quantify the contribution effect of $Na_2O$% and Ms on AAS properties.

**Chapter 5** focuses on applying the first mitigation strategy which is shrinkage reducing admixture. The first part of this chapter proposed how the presence of SRA impacts the AAS pore solution and its interactions in the AAS system. This was achieved by conducting a chemical analysis for the extracted pore solution and the surface tension measurements in the presence of SRA. Further, this chapter focuses on providing a fundamental understanding of the SRA effects on AAS basic hydration mechanisms and the reasons behind the retardation effect. Moreover, SRA's behavior in AAS was related to its impact on autogenous shrinkage. Extensive

hydrated phase analysis is conducted by various tests to reveal the impact of SRA on the microstructure and phase assemblage composition of AAS.

**Chapter 6** applies superabsorbent polymers as an internal curing agent to enhance the shrinkage behavior of AAS. First, individual experimental series were performed to understand the absorption capacity of SAPs in an extracted AAS pore solution, considering the potential screening effect of divalent ions that exist in the extracted pore solution. Furthermore, the desorption mechanism of AAS paste under sealed hydration conditions was investigated by computed tomography (Micro CT). The effect of water entrained by SAPs on the hydration evolution, pore structure, and compressive strength was investigated and compared with ordinarily added water. The role of various SAPs contents on the internal relative humidity development and the free autogenous deformation was investigated. Taking a step further, the desorption process in AAS was related to autogenous shrinkage development. Finally, the unreported shrinkage behavior while AAS was incorporated by SAPs under drying conditions was revealed in this work. The microstructural investigation was performed by SEM and EDX.

**Chapter 7** was intended to combine and enhance the benefits of both SRA and SAPs after extensive investigations were performed identifying the optimized content of each SAPs and SRA in AAS. The application of the hybrid system utilizing SAPs and SRA in AAS was studied in this chapter. Tests were performed to reveal how SAP and SRA can counteract each others' shortcomings. SAPs absorption in various liquids was measured by optical microscope images. Furthermore, the absorption in AAS paste was evaluated by X-ray tomography and further analysis by ImageJ was performed to measure the size distribution of macrovoids. The surface tension was evaluated with various content of SAPs and SRA. Moreover, the combined effect of both on hydration, compressive strength, autogenous, and drying shrinkage were examined.

**Chapter 8** summarizes the main achievements, contributions, and recommended future work resulting from this research.

# Chapter 2 -Literature review

Research regarding AAS for the purpose of mitigating shrinkage has been receiving significant interest globally. The theoretical concepts, experimental measurements, and background information will be discussed in this chapter. Research related to the main factors affecting shrinkage in cementitious materials and, more specifically, the main causes of the shrinkage of AAS and will be reviewed. Furthermore, a summary of current studies on various mitigation techniques that have been applied to compensate for the shrinkage of AAS is presented.

## 2.1 Suggested mechanisms of AAS Shrinkage

### 2.1.1 The capillary pore pressure mechanism

The capillary tension mechanism is typically used to explain the shrinkage of AAS at medium to high levels of relative humidity conditions (e.g., RH ≥ 40%) (Ye and Radlińska, 2016a). Autogenous shrinkage happens under sealed conditions, and so this mechanism is considered the main cause of autogenous shrinkage. As the activation process of AAS is taking place, internal moisture is consumed gradually, which leads to the form of liquid vapor menisci in a process called self-desiccation (i.e., Internal drying) (**Fig. 2.1**). Consequently, capillary tension is generated, which leads to pulling the adjacent pore walls closer, which results in the bulk shrinkage of the AAS matrix (Ye and Radlińska, 2016a). Additionally, autogenous shrinkage is linked to chemical shrinkage which results from the reduction in the absolute volume of the paste, where the reaction products occupy less volume than the initial reacting materials, and it is directly proportional to the degree of reaction of slag. The chemical shrinkage of the AAS pastes is attained between 0.103–0.127 mL=$g_{slag}$, which agrees with the estimated values that have been obtained by Thomas *et al*. (2012) and Chen and Brouwers (2007). This value is remarkably higher than the value of OPC at complete hydration, which is about 0.064 mL=$g_{cem}$ (Jensen and Hansen 2001).

Capillary tension can be calculated according to (Eq 2.1), which is directly proportional to the surface tension of the pore solution and the kelvin radius.

$$P_{cap} = \frac{2\gamma\cos\theta}{r} \qquad 2.1$$

$P_{cap}$ = capillary tension on the liquid phase (Pa) which is caused by the formation of vapor-fluid menisci inside the matrix pores and can be related to the size of the menisci and the pore solution properties (c and θ), c is the surface

tension of the pore solution (N/m) and for pure water $\gamma$ = 0.0730 N/m; $\theta$ is the solid-solution contact angle, and r is the Kelvin radius (m) (Radlińska et al. 2008)

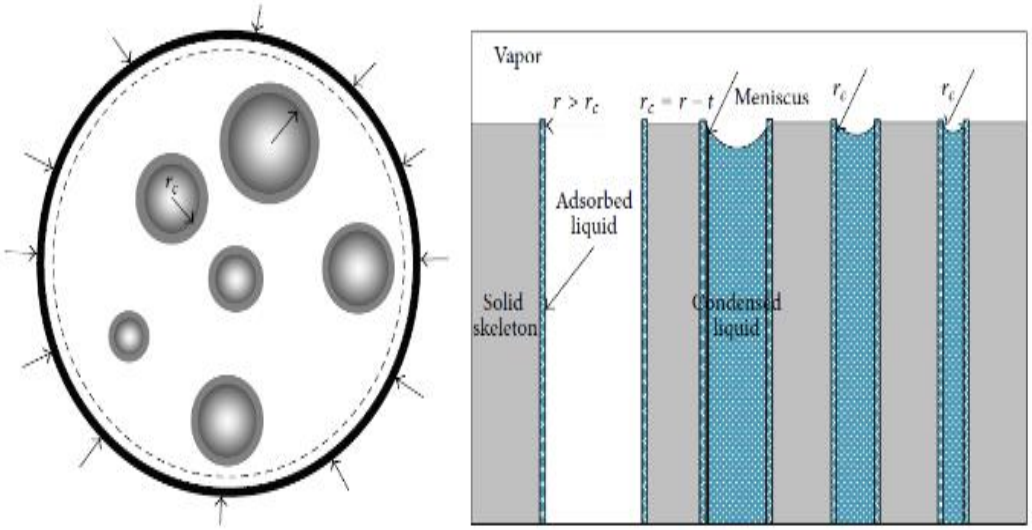


Fig. 2.1. Schematic illustration of the drying process with different pore sizes, the formation of the meniscus, and generation of capillary pressure (Ye and Radlińska, 2016b)

The surface tension of the AAS pore solution is higher than in OPC, especially when the dosage of the activator increases (**Fig. 2.2a**) (Kumarappa *et al.,* 2018). Moreover, AAS exhibits finer pore size distribution when compared to that of OPC and a higher volume of mesopores (**Fig. 2. 2a**) (Neto *et al.,* 2008). Both directly impact the tensile stress and generated this high autogenous shrinkage (Eq 2.1).

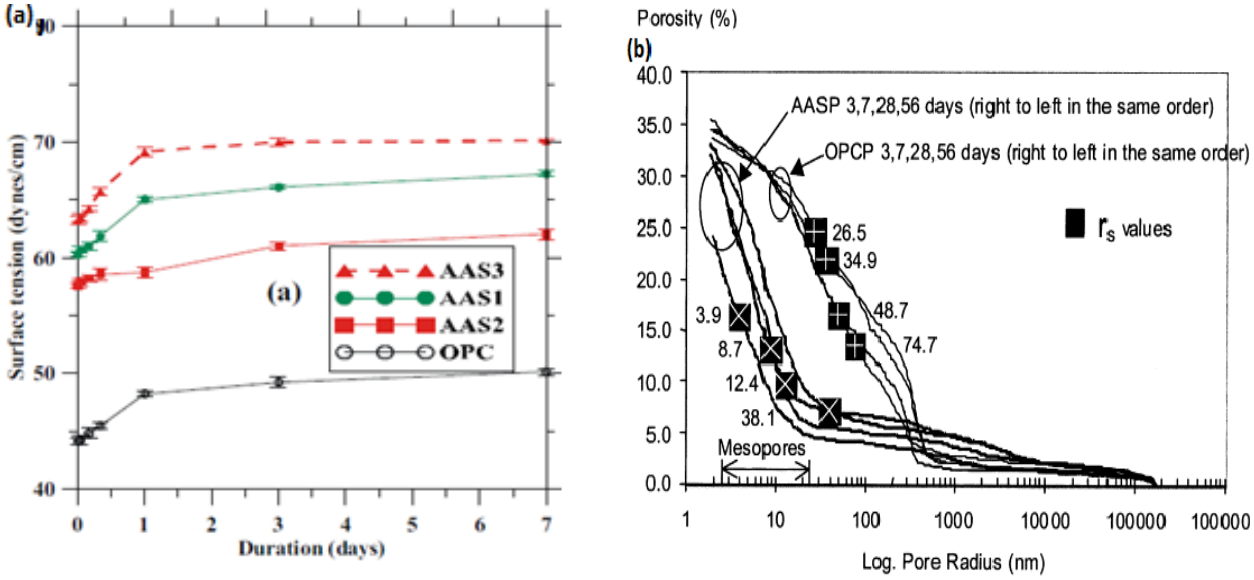


Fig. 2.2. (a) Surface tension of pore solution of AAS pastes with different $Na_2O$%, AAS1 5%, AAS2 4%, AAS3 6% (Kumarappa et al., 2018), (b) Cumulative pore size distribution of OPCP and AASP at 3, 7, 28, and 56 days (Collin and Sanjayan, 2000).

According to Bakharev *et al*. (2000) and Cartwright *et al*. (2014) the autogenous shrinkage strains of AAS concrete are up to seven times larger than those found in OPC due to the lower stiffness level, higher degree of saturation, more chemical shrinkage, and a finer pore structure than AAS concrete.

In unsealed conditions, both internal and external drying occurs, and shrinkage is referred to as drying shrinkage. Researchers attribute high drying shrinkage to high capillary pressures (RH>40), the absence of expansive phases formation (ettringite or portlandite), and the calcium silicate hydrate gel characteristics (Ye and Randilska, 2017). The formation of nano-sized portlandite significantly increases the stiffness of OPC (Chen *et al*., 2010). Consequently, due to the limited amount of formed portlandite in AAS, this can partially explain the decreased stiffness and increased shrinkage. Nonetheless, it is agreed that the capillary pore tension mechanism is limited to a moderate to a high level of relative humidity where the menisci are still present (Ye and Radlińska, 2016a).

### 2.1.2 Gibbs-Bangham Shrinkage

Surface free energy (Gibbs-Bangham shrinkage) is the spreading of physically adsorbed water within the pore volume, which reduces the surface energy and causes shrinkage at low RH conditions (e.g., 30 % RH) (**Fig. 2.3**) (Mehta and Monteiro, 1993). According to Ye and Radlińska (2016b), Gibbs-Bangham shrinkage is effective, and it can partly explain its shrinkage performance. At low RH (e.g., 30 % RH), the surface energy increases and the viscous characteristic of AAS shrinkage almost disappears. According to Jennings, (2008), at RH < 50%, the capillary meniscus becomes unstable at equilibrium conditions, and the air-water interface enters small gel pores. In this case, the surface free energy is the controlling shrinkage mechanism, which results in stress in dissimilar directions, magnitudes, and locations, and triggers the densification of the particle itself. This process is not similar to capillary pressure, in which the former drives the adjacent solid particles closer by the confining pressure (Kovler, 2006; Ye et al., 2016).

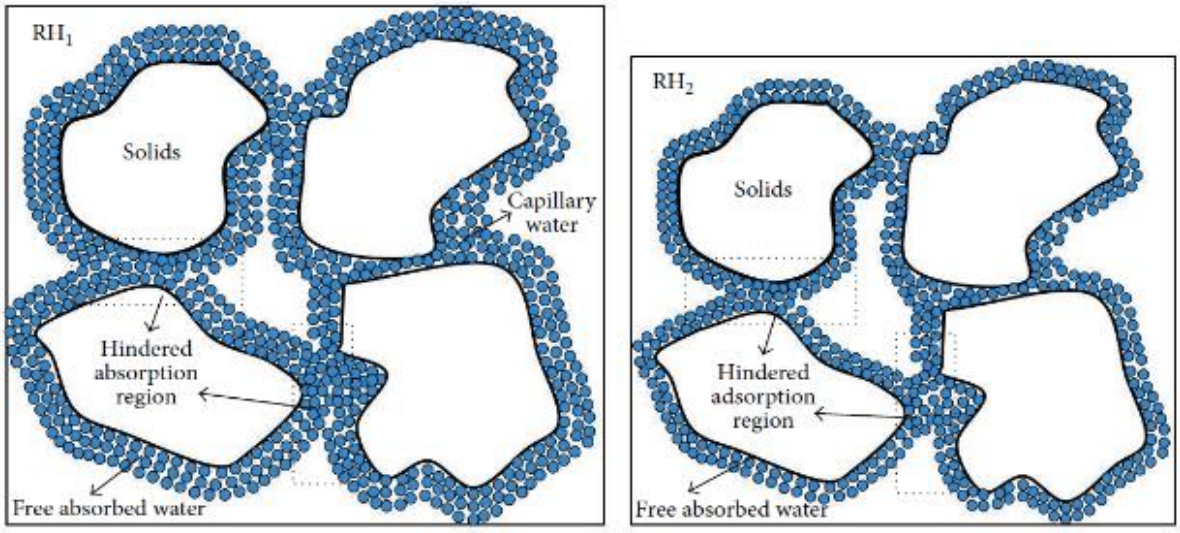


Fig.2.3. Schematic illustration of volumetric reduction due to change in surface free energy when desorption takes place ($RH_2 < RH_1$) (Ye and Radlińska, 2016b).

### **2.1.3** Disjoining Pressure

Disjoining pressure is created due to confined water in fine spaces, which often occurs in pores with a diameter <2.6 nm (Bazant *et al*. 201). This confined water hinders the adsorption layer, and a cohesive interaction is created between the pore water and the surface within the pore

volume (van der Waals forces) (**Fig. 2.4**) (Thomas *et al*. 2016). Ye and Radlińska (2016b) also attribute the high shrinkage of AAS compared to that in OPC, by this mechanism. The disjoining pressure is active in fine pores and the released pressure is related to the pore diameter. Since the pore structure of AAS is finer than OPC, the proportion of pores in the active range of disjoining pressure is larger in AAS.

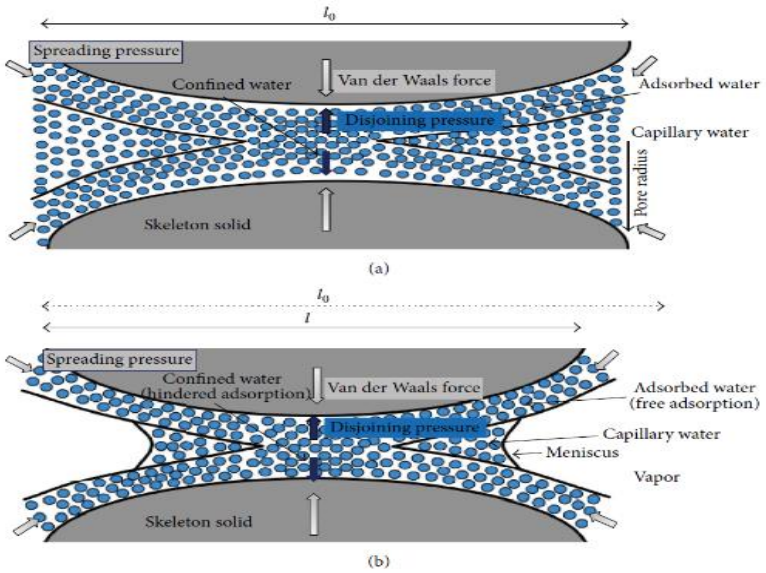


Fig. 2.4. Schematic illustration of the drying process in hindered adsorption region and withdrawal of disjoining pressure: (a) initial status, (b) after RH decreases. This figure shows the simultaneous occurrence of surface free energy-induced shrinkage and withdrawal of disjoining pressure-induced shrinkage (Ye and Radlińska, 2016b).

### 2.1.4 Shrinkage caused by syneresis of C-A-S-H gels

Syneresis of C-A-S-H is defined as the contraction of silica gels that forms in AAS during the polymerization process (Chen et al., 2021). Alkali-enriched calcium-alumina-silicate-hydrate (C-A-S-H) are the main hydration products in the AAS systems. Due to alkali enrichment, these nanoparticles are thermodynamically unstable upon drying, and the particles sliding between adjacent C-A-S-H sheets contribute significantly to the large shrinkage. Hence, syneresis of C-A-S-H gels is adopted to be an additive mechanism that contributes to the high shrinkage of AAS.

## 2.2 Factors Affecting AAS Shrinkage

Different factors affect the shrinkage behavior of AAS, mainly the type and dosage of activator, slag content, the fineness of the slag, and the curing conditions employed.

### 2.2.1 Activator nature and content

Many researchers study the shrinkage characteristics of AAS as a function of activator type/ dosage. For instance, it was reported that as the dosage of the NaOH activator increases, the degree of reaction increases, which can potentially increase the shrinkage of AAS (Ye *et al.* 2017).

NaOH activators cause a quick dissolution of slag, which acts as a catalyst to accelerate the hydration of slag particles. The reaction products form quickly and act as a diffusion barrier around the unreacted slag particles, which hinders the further dissolution of slag particles. Therefore, a course structure and higher porosity are generated, as compared with AAS activated by waterglass (Ben Haha *et al.* 2011). These results agree with the finding of Cartwright *et al.* (2014).

Many studies investigated the role of waterglass in activating the AAS systems. [Douglas et al., 1992; Bakharev et al., 1999; Collins and Sanjayan, 1999a; Collins and Sanjayan, 1999b; Atis et al., 2009]. For instance, an Aydın and Baradan (2013) study showed that AAS mortars activated by waterglass have a higher compressive strength, lower water absorption characteristics, and lower porosity when compared to AAS mortars activated by NaOH. This is attributed to a slower dissolution of slag and uniform precipitation of C-S-H and C-A-S-H within the open pore space when using waterglass. Moreover, it was found that shrinkage values of AAS activated by waterglass reached up to six times when compared to OPC. However, the waterglass activator is mainly controlled by sodium oxide content ($Na_2O$%) and activator modulus (Ms). Sodium oxide content ($Na_2O$%) reflects the ratio of sodium oxide in the activator to that in the binder by weight, while Ms is the ratio of silicon oxide to sodium oxide ($SiO_2/Na_2O$) in the activator. Common ranges of both parameters were between 0.4-2 and 2%-8% for Ma and $Na_2O$%, respectively. Increasing both impacted the autogenous and drying shrinkage of AAS, which was attributed to the intensive reaction, increased volume fraction of capillary pores, and the subsequently higher capillary pressure (Aydın and Baradan, 2013; Atis et al. 2007). A recent

study highlighted that increasing Ms to 2 at constant $Na_2O$% led to a reduction in the autogenous shrinkage of AAS paste. Authors attributed that to the existence of an excessive amount of silica in the activator that resists the internal drying and humidity reduction, and consequently, reduces the autogenous shrinkage (Chen et al., 2021).

Based on the literature, the activator type and chemistry have a great influence on the performance of AAS (Shi, 1996). For example, AAS mortars exhibited similar shrinkage values, suitable strength, and similar setting times when compared to PC mortars when using sodium carbonate to activate slag (Atis et al. 2007). However, several advantageous properties of activation with waterglass were reported. Hence, to design the AAS system, it is important to understand the significance of each activator factor and which factors contribute to specific properties of AAS systems. It is important to optimize controllable cementitious contents to achieve peak performances in terms of compressive strength and shrinkage for AAS mixtures.

### 2.2.2 Curing conditions

The shrinkage of AAS concrete shows high sensitivity to curing conditions. Thomas *et al.* (2017) investigated the effects of age and curing methods on the manifestation of drying shrinkage in AASC. The results showed that the drying shrinkage is reduced by two-thirds or more for samples that dried at a later age (i.e., dried after 90 days of limewater curing) when compared to samples dried at an early age (i.e., dried after 48h limewater curing). Moreover, AAS mortars samples exposed to moist curing exhibited lower shrinkage values when compared with samples that were dry-cured. This is due to the ambient condition, where the evaporation of free water is reduced within high relative humidity (Bilim *et al.* 2013).

**Figure 2.5** shows the drying shrinkage values of concrete upon different curing regimes, the samples that were exposed from day 1 have the highest values of shrinkage; it is due to the greater moisture loss during the first 7 days. Furthermore, samples that rested in the water and that were cured showed minor expansion and a higher shrinkage rate when exposed (Collins and Sanjayan 1999a).

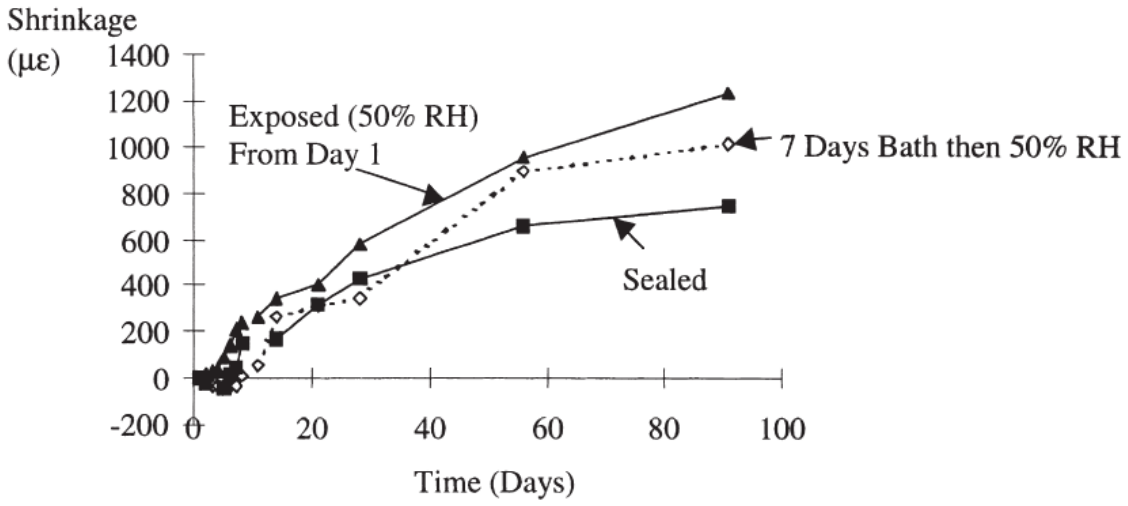


Fig. 2.5. Shrinkage strain of standard prisms following exposure to various curing regimes (Collins and Sanjayan, 1999a)

### 2.2.3 The binder composition, content slag, and fineness

It was proven that increasing the binder content led to an increase in the paste volume, which directly increases drying shrinkage. The paste is more affected by shrinkage when compared to the aggregates as they are highly dimensionally stable (Thomas *et al.* 2017). Furthermore, the composition of the raw materials heavily influences drying shrinkage. For example, high calcium alkali-activated systems usually experience a higher drying shrinkage rate than cement-based systems (Neto *et al*. 2008). On another hand, the low calcium alkali systems exhibit a lower shrinkage value compared with that of OPC (Ma and Ye, 2015). Ground-granulated blast-furnace slag is considered a calcium-rich aluminosilicate precursor in AAM. Therefore, the drying shrinkage of blended slag-fly ash increased when a higher slag content was used in that system (Gao *et al*. 2016).

Moreover, slag fineness significantly influences the reaction kinetics and the reactivity of the slag (Yuan *et al*. 2017). Generally, the slag used in AAS should be finer than those used in OPC. The recommended slag fineness ranges are 4000-5500 $cm^2/g$, while those in OPC blends are ~3500-4500 $cm^2/g$ (Wang *et al*. 1994). Zhang et al. investigated the influence of three types of slag with a fineness of 3000, 4000, and 8000 $cm^2/g$, and results showed that the specimens that incorporated slag with 8000 $cm^2/g$ fineness exhibited the greatest drying shrinkage. However, the complete influence of the chemistry of slag is not fully understood yet.

## 2.3 Shrinkage mitigation strategies in AAS

Several mitigations strategies were developed due to the high shrinkage rates in AAS systems. These strategies can be divided into three major groups, which are (1) mitigating the shrinkage driving forces, (2) expansive reaction, and (3) curing at elevated temperature.

### 2.3.1 Mitigating the shrinkage driving forces

The main driving shrinkage force that controls the shrinkage of AAS with RH>40% is capillary pressure (Kumarappa et al. 2018). According to the Laplace equation (Eq. 2.1), the magnitude of capillary stresses ($P_{cap}$), which is the main factor dominating shrinkage, depends on both the radius of the largest pore (r) and the surface tension of the pore solution (γ) (Neto *et al*. 2008). Hence, shrinkage reduction strategies can be implemented to reduce the surface tension of the pore solution or by applying an internal curing approach.

*a. Applying shrinkage reducing admixture (SRA)*

Shrinkage reducing admixtures is a viable technique in mitigating both drying and autogenous shrinkage. Their role in reducing the shrinkage originates from reducing the surface tension of the pore solution (Nmai et al. 1998; Bentz et al. 2001), which consequently decreases the capillary tension in the pore system. However, there are limited studies on the effect of SRA on the alkali-activated slag systems activated by waterglass. The influence of 2% shrinkage-reducing admixture based on polypropylene glycol on AAS mortars, activated by water glass, was efficient in decreasing the autogenous and drying shrinkage by 85% (cured at 99% RH) and 50% (cured at 50% RH). This is attributed to the reduction in the surface tension of the pore water, which contributes less internal stress upon the evaporation process. Moreover, the addition of SRA caused an increase in the proportion of pores with a diameter ranging from 1.0 to 0.1 μm, which promotes less capillary stress than that in mortars without the added admixture (Palacios and Puertas, 2005; Palacios and Puertas, 2007). According to Bilim *et al*., (2012), 1% SRA reduced the drying shrinkage of AAS mortars activated by waterglass, but still, this SRA dose demonstrated more shrinkage than OPC. Kumarappa et al. (2018) studied the addition of various dosages of SRA and found that 7.5% SRA was effective in compensating against the autogenous shrinkage by around 75%.

Moreover, the effect of SRA based on 2-methyl-2, 4-pentanediol was investigated on waterglass-activated slag mortars. The influence of this type of SRA could be considerably different from SRA based on polypropylene glycol. The results showed that 1.0% of this type of SRA reduced the drying shrinkage by more than 80%, but it had a negative impact on early compressive and flexural strengths.

However, by reviewing the literature, the working mechanism of SRA and its interactions with AAS's pore solution are not investigated yet.

*b. Internal curing*

Internal curing is to simply provide extra water to reduce self-desiccation and to lead to lower tensile stress inside the pores of AAS paste. This can mitigate autogenous shrinkage. The internal curing agent is added during mixing and could be lightweight, absorbent aggregates (LWA) (e.g., pumice or expanded clay), or a superabsorbent polymer that acts as a water reservoir (Trtik *et al.,* 2011). The mechanism behind this process is internal curing. Initially, the liquid is desorbed by the internal curing agent, and as the internal humidity of the system drops, water enters the binder paste pores, which inhibits the self-desiccation process. Thus, the extensive tensile stresses are avoided which causes a drop in autogenous shrinkage (Sakulich and Bentz, 2012). Furthermore, LWA is distributed uniformly so that the system can be cured consistently. Autogenous shrinkage is firmly associated with chemical shrinkage, and internal curing has a considerable influence on the chemical shrinkage which can lower its intensity up to 50 % (Bentz *et al.* 2004).

According to Sakulich and Bentz (2012), internal curing can effectively mitigate autogenous shrinkage in AAS, which contains high levels of reactive silica and high pH activating solution (e.g., water glass /NaOH). Particularly during the first 7 days, the high pH level encourages the reaction of the slag, which causes the moisture to rapidly expand during the reaction process, causing more moisture released from the agents.

Superabsorbent polymers (SAPs) can reduce self-desiccation and autogenous shrinkage of alkali-activated slag materials. Song *et al*. (2016) stated that increasing the dosage of SAP would increase the internal relative humidity, which provokes more effective internal curing took place. The shrinkage compensating factor for AAS mortars, activated by waterglass and $Na_2CO_3$, with 0.6% SAP was 86% and 78% respectively. Hence, an increased dosage is needed to mitigate the

shrinkage completely. Furthermore, it is concluded that the content of SAP that is needed in AAS mortars is greater than that in OPC mortars. For example, around 0.3% SAP was found effective in OPC to mitigate 100% of autogenous shrinkage. A superabsorbent polymer's effect on the autogenous shrinkage of one-part AAS systems was investigated, which showed a result of a reduction of 60–75% in the autogenous shrinkage (Oh and Choi, 2018). On another hand, a compressive strength loss was observed of mixtures with SAPs inclusion. This is attributed to the fact that SAP acts as voids within the specimens. However, the influence of SAPs on the drying shrinkage of AAS is not fully investigated.

### 2.3.2 Elevated temperature curing

Heat curing and aging are considered effective mitigation techniques for drying shrinkage and promoting high early strength. Bakharev et al. (1999) explained that the curing at raised temperatures for 6 h considerably reduced drying in the waterglass AASC. Heat treatment caused changes in pore structure and the condensation of C-A-S-H, which lead to coarser porosity, and thus, a reduction in effective capillary stress. As shown by Thomas et al. (2017), heat curing reduced the drying shrinkage of AAS concrete by around 75%. Bilim et al. (2012) achieved a significant reduction, particularly in early age shrinkage of AAS mortars, when cured at 65°C in water for 5 h. This is due to the fact that the elevated temperature curing made the concrete dimensionally stable. However, at elevated temperatures, the AAS reactions are accelerated, consequently refining the microstructures. Several microstructure studies have been performed on AAS mortars to understand the reasons for the reduced shrinkage from heat treatment, showing that through heat curing, the resulted C–S–H contains a lower water content (Bakharev *et al.*, 1999b; Aydin and Baradan, 2012). However, other researchers mentioned that the mechanisms behind the shrinkage reduction by heat treatment remain unknown. Authors Ye, and. Radlińska (2017) found that heat curing improved the crystallinity of hydrated phases in AAS, whereas C-A-S-H nanoparticles become more crystalline (loss less water upon drying) and the inter-particle bonds are strengthened. Furthermore, the heat-cured C-A-S-H is thermodynamically more stable, meaning the instability is caused by alkali enrichment.

Moreover, the heat treatment history influences drying shrinkage. For example, the pre-treatment at room temperature for 2 h before curing at a high temperature significantly decreased shrinkage in AASC by around 30% (Bakharev et al. 1999).

On another hand, heat curing means additional energy consumption, meaning these curing systems are impractical in-situ. Nevertheless, heat curing is considered an appropriate mitigation method for precast applications in which these curing regimes are more practical and feasible (Thomas et al. 2016).

### 2.3.3 Expansive Reaction

Using expansive agents (e.g., gypsum, CaO-type, and MgO-type), one can reduce the drying shrinkage through the formation of voluminous AFt, portlandite, and hydrotalcite in AAS.

#### 2.3.3.1 Reactive MgO

Magnesium oxide (MgO) has been used as a shrinkage reducing mineral additive since it has high efficiency in controlling the shrinkage of Portland cement. The dead burned MgO is naturally present in slags. Two types of MgO are usually used, namely the reactive MgO (calcined under 1000 C) or hard burned MgO (calcined at 1000–1400 C). The characteristics of reactive MgOs may vary considerably, depending on their calcination history (Shand, 2006). However, the performed investigations on the effect of reactive MgO on the shrinkage of AAS binder are limited. Fang *et al*., (2011) studied the effect of the inclusion of burnt magnesia on drying shrinkage and other properties of waterglass activated AAS with various dosages (0%, 2%, 4%, 6%, and 8 wt%), and at different temperatures of MgO (800, 850, 900, 950 C) for 2 h, which showed results of the burnt MgO harming drying shrinkage. For MgO calcinated at high temperatures (850–950 C), this product reduced the AAS shrinkage as the MgO content increased. Furthermore, the authors recommended using up to 8% of MgO, otherwise, it may affect the other properties of AAS (e.g., setting time, compressive and flexural strengths) negatively. The shrinkage reduction happened because of the expansion of the hydration and carbonation of MgO.

#### 2.3.3.2 Quicklime (CaO)

Calcium oxide (CaO) enrichment was found insufficient in reducing drying shrinkage in AAS, shown through observations where the incorporation of CaO with different dosages in AAS mortars (i.e., Exposure to 50 and 70% RH) lead to the absence of the early-age expansion in AAS. Moreover, it resulted in the refinement of the pore structure. The chemical shrinkage of AAS was unchanged as the portlandite was formed. Thus, the drying shrinkage increased, despite the decrease of moisture loss. This supports the conclusion that the dominant mechanism of shrinkage at high RH (> ~50% RH) is capillary stress. Moreover, Yuan *et al* (2014) mitigated the drying shrinkage of AAS paste by using composite expansion agents, namely anhydrite and quicklime. Increasing the amount of EA results in a decreased drying shrinkage of the concrete. Ettringite was not detected in the hardened paste while portlandite was observed. Therefore, the formation of portlandite was responsible to compensate for the shrinkage in AAS concrete. Jia *et al* (2018) compensated for the drying shrinkage of AAS by adding two types of composite expansion agents in CSAE (calcium sulphoaluminate type expansion agent) and CE (CaO type expansion agent) Results showed that at 56 d, adding CSAE and CE decreased the drying shrinkage by around 45% and 55%, respectively, in AAS mortars.

Through the addition of CSAE, the hydration products in AAS will be changed where $Na_2SO_4$ crystals and Aft are produced. The formation of these voluminous crystals compensated for part of the drying shrinkage. In the CE group, which is different from the CSAE group, a lot of CH was produced by the reaction between CaO and water. However, these generated crystals restrict the deformation of C-A-S-H gels during the drying process, which thereby lowered the shrinkage. As noticed under the same drying condition, the CE group has a better effect in resisting the deformation than the CSAE group under the same conditions. This attributed to the higher elastic modulus of CH than Aft, which contributes less deformation of C-A-S-H gels

#### 2.3.3.3 Gypsum

Optimized gypsum dosing is proven to be effective in reducing the autogenous and drying shrinkage considerably. Researchers found the formation of expansive phases, such as ettringite (AFt) and AFm, causes volume expansion to be reduced, thus decreasing the shrinkage (Ye and Radlińska, 2017b). Bakharev *et al*. (2000) reported that a 6% dose of gypsum could significantly lower drying shrinkage for the AAS concretes (i.e., At 50% RH). At age 56 days, the drying

shrinkage was beneath 150 microstrains, while the autogenous one was around 500 microstrain. The 6% gypsum was indicated as the optimized value, due to the increased formation of AFt and AFm phases (**Fig. 2.6**).

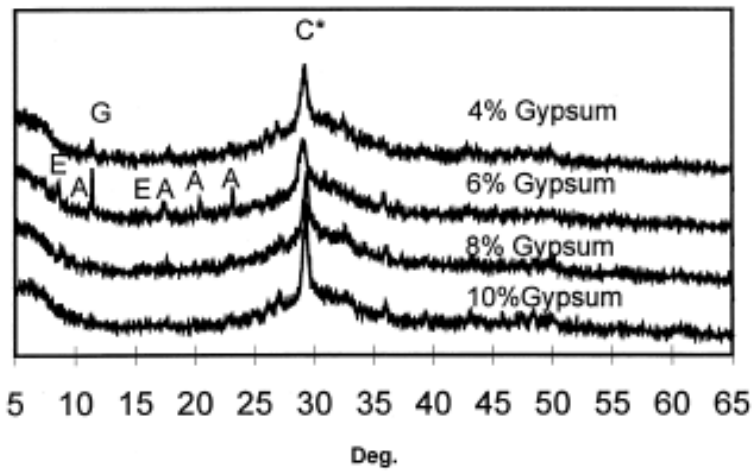


Fig. 2.6. XRD of AAS paste with different content of G, 3 days after start of hydration; C * = overlapping C-S-H and calcite, G = gypsum, Ca-$SO_4$_$2H_2O$; E = AFt phase, $C_3A$_$_3CaSO_4$_$32H_2O$; A= AFm phase, type $C_3A$_$CaSO_4$_H11±13 (Bakhrev et al., 2000).

### 2.3.4 Mitigating the shrinkage by chemical, minerals admixtures, and Fibers

Shrinkage can be reduced by using the appropriate additives type and dosages. Recently, the inclusion of various types of admixtures and fibers was investigated in alkali-activated slag. **Table 2.1** below shows the effects of different types of admixtures and fibers on the shrinkage of AAS.

Table 2.1. Effect of Admixtures and Fibers on AAS shrinkage

| | Type | Influence on shrinkage | Condition | Reference |
|---|---|---|---|---|
| **Chemical Admixture** | **Shrinkage reducing admixture (SRA)** | 2% reduced autogenous and drying by 85% and 50%, respectively. ` | (21 ± 2 °C), 50% RH | (Bakharev et al., 2000) |
| | | 2.5%, 5%, 7% reduced the autogenous shrinkage by 43%, 57% and 77% respectively. | (21 ± 2 °C) 99% | (Kumarappa et al., 2018) |
| | **Water-reducing and retarding admixtures (WRRe) based on lignosulphonates** | Dosage1% WRRe slightly decreased the autogenous and drying shrinkage by 20% and 28%, respectively. (still higher than that in OPC) | (21 ± 2 °C), 50% RH | (Bakharev et al., 2000) |
| | **Air entraining agent (AEA)** | 6 mL/Kg slag, the drying shrinkage reduced by 73% | (21 ± 2 °C), 50% RH | (Bakharev et al., 2000). |
| | **Superplasticizer admixture based on modified naphthalene polymers** | Increased the shrinkage by about 1.5 times the values without using it. | (21 ± 2 °C), 50% RH | (Bakharev et al., 2000). |
| | **Set-retarding admixtures (SSR) based on modified polymer liquid** | 1% SSR decreased the shrinkage slightly by 11% (still higher than that in OPC) | (23± 2°C) and 90% RH<br>65 °C for 5 h | (Bilim et al., 2013) |
| **Mineral Admixtures** | **Fly Ash (FA)** | Decreasing the drying shrinkage with increasing FA content<br>20 %, 40% reduced the drying shrinkage by 15 and 18, respectively. | Steam curing (105 ± 5 °C), | [Chi and Huang, 2013<br>; Aydın, 2013] |
| | **Silica Fume (SF)** | 10% Reduced the drying shrinkage by 45%,<br>20% of SF is recommended to reduce the drying shrinkage by 75%, | Steam curing (105 ± 5 °C) for 16h. | (Aydın, 2013) |
| | **Portland cement (PC)** | 10% was the optimal dosage in reducing the drying shrinkage (shrinkage value similar to PC value) | 20°C with 95% RH | (Fu-Sheng et al., 2005) |
| | **Lime Powder (LP)** | LP >30% reduced the autogenous shrinkage.<br>LP percentage increases, the drying shrinkage also increases. | 21 ± 2 °C), 90% RH<br>21 ± 2 °C), 50% RH | (Yuan et al., 2017) |

| | Type | Influence on shrinkage | Condition | Reference |
|---|---|---|---|---|
| Other additives | **Phosphoric acid** | 0.82 M Increased the drying shrinkage | (21 ± 2 °C, 50% RH) | (Chang et al., 2005). |
| | **Nano $TiO_2$** | 0.5% decreased the drying shrinkage of AAS paste by 30% | 20 ± 3 °C), 50% RH) | Yang et al. (2014) |
| | | 0.5% decreased the autogenous shrinkage of AAS paste by 10% | (20 ± 3 °C, 90±5 % RH) | |
| Fibers | **Steel fibers** | 6- and 13-mm length and dosage of 1.5 %, the drying shrinkage values of AASS decreased by 24% | Steam curing (105 ± 5 °C) for 11h | (Aydın and Baradan, 2013) |
| | **Polypropylene fibers** | 1% fiber reduced the drying shrinkage by 20% | Room temperature, (50% RH) | (Puertas et al., 2003) |
| | **Glass fibers** | 1.1% reduced the drying shrinkage by 23% | Room temperature, (50% RH) | (Puertas et al., 2006) |
| | **Carbon fibers** | 0.2% CF with 3- mm and 6-mm length decreased the autogenous shrinkage by 38% and 45%, respectively. | 20 °C, 99% RH | Vilaplana et al., 2016 |
| | | 1% CF with 12mm length reduced the drying shrinkage significantly. | 20 °C, 50% RH | |

## 2.4 Current Practices Limitations

Using these admixtures is relatively effective in decreasing both autogenous and drying shrinkage of AAS. Shrinkage reducing admixtures are commercially available, economic, and showed a significant role in reducing the shrinkage. Furthermore, SRA has been investigated intensively in OPC systems (Bentz et al., 2001; Bentz and Jensen 2004; Weiss et al., 1999; Ribeiro et al., 2006). On the other hand, there are limited studies on the effect of SRA on the alkali-activated slag systems activated by waterglass. According to Bakharev et al., (2000), SRA is insoluble in alkaline solution, thus, it can reduce the shrinkage with different dosages. The current findings in the literature do not provide sufficient information about the surfactant (i.e., SRA) behavior and its interactions within the AAS system. Additionally, there are no impact assessments for the effect of SRA on AAS hydration, and the causes for the lower early strength development in AAS systems are unknown. Furthermore, there are no studies concerning the threshold of SRA concentration which beyond this concentration, the surface tension value becomes stagnant.

The application of SAP in the AAS system is provided by some minor available studies (Song and Choi 2016; Oh and Choi 2018), however, the limited current published research only deals with the inclusion of SAP to mitigate the autogenous shrinkage of AAS. The efficient dosage for optimized SAP usage as an IC agent in an AAS system, activated by waterglass, has not been identified yet. Additionally, the study of the effects of the addition of SAP on the drying shrinkage of AAS, nor physical properties, have not being investigated.

Both SRA and SAP are efficient in mitigating autogenous shrinkage. Sakulich and Bentz, 2012 recommended the inclusion of SRA in addition to the internally cured AAS in order to enhance the drying shrinkage behavior as it is speculated that combing them would enhance the obtained benefit in reducing both autogenous and drying shrinkage. Nevertheless, the combined effect of both is unknown and has not been researched to this day.

# Chapter 3 - Materials and Experimental Approaches

This chapter presents the experimental plans (**Fig. 3.1**) that have been performed to achieve the main objectives of the current research.

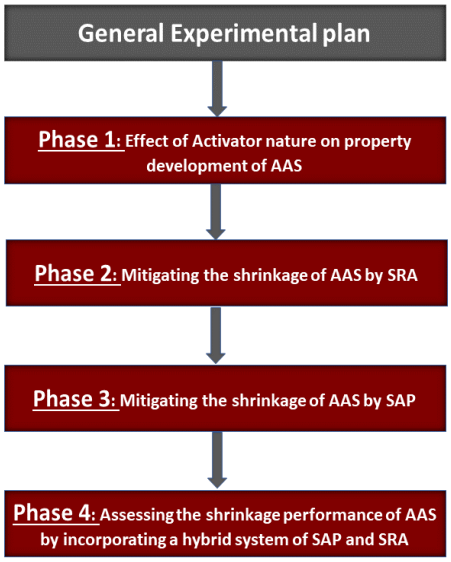


Fig. 3.1. Experimental work plan

## 3.1 Experimental program

The purposes of phase 1 are to investigate the role of activator chemistry on different properties of AAS mortars, understand the significance of each activator factor, and which factor has more contribution to a specific property of AAS mortars. Effects of $Na_2O$ %, in the range of (4% - 8%), and Ms ranges from 0.5 to -1.5.

The output of that phase helped in selecting the proportion of $Na_2O$% and Ms depending on the compressive strength and shrinkage performance. By considering the detrimental effect of increasing both activator parameters, 6% of $Na_2O$ and Ms of 1 were selected as the best adequate waterglass parameters that exhibit high strength and medium shrinkage values. As revealed from the statistical analysis, Ms has a more significant effect on the shrinkage, so increasing Ms to 1.5 contributes to higher shrinkage without significant enhancement in the compressive strength, as

discussed in detail in the following chapter (i.e., Chapter 4). Hence, $Na_2O$ of 6% and Ms of 1 were selected as the optimal activator proportion for the next phases.

The investigation on shrinkage involves the autogenous and total drying shrinkage on:

(a) AAS mortars containing various dosages of alkaline activator and silicate modulus.
(b) AAS mortars containing various dosages of SRA.
(c) AAS mortars containing different content of SAPs.
(d) A combination of both types of SRA and SAPs is investigated on AAS mortars.

*Mixtures preparation*: Alkali activated slag specimens were mixed by using an electrically driven mechanical mixer conforming to the requirements of ASTM C305 (Standard Practice for Mechanical Mixing of Hydraulic Cement Pastes and Mortars). Initially, dry ingredients were mixed for a minute. After premixing of the dry ingredients (i.e., GGBS and sand) for 1 min, the activator was added and continued mixing at low speed for 1 min, then for another 2 min at high speed. All mixtures were prepared with a liquid/ binder ratio of 0.4 at room temperature.

*Curing conditions*: Specimens that are tested under drying conditions were kept inside an environmental chamber under a controlled condition (T = 23±2C° and 45±5% relative humidity).

## 3.2 Materials

### 3.2.1 Ground granulated blast furnace slag

Grade 100 ground granulated blast furnace slag (GGBS) was used, and the chemical compositions are listed in Table 3.1. The basicity coefficient [$K_b = (CaO + MgO)/ (SiO_2 + Al_2O_3)$] and the hydration modulus [$CaO + MgO + Al_2O_3)/SiO_2$], for the used GGBS were 1.06 and 1.63, respectively.

The specific gravity of the slag and the Blaine fineness were 2.92 and 515 $m^2$/kg, respectively.

Table 3.1 The chemical composition of the slag

| Items | $SiO_2$ | $Al_2O_3$ | CaO | $Fe_2O_3$ | $SO_3$ | MgO | $K_2O$ | $Na_2O$ | $TiO_2$ | $M_nO_2$ |
|---|---|---|---|---|---|---|---|---|---|---|
| (Wt. %) | 36.5 | 10.2 | 37.6 | 0.5 | 3.1 | 11.8 | 0.4 | 0.3 | 1.0 | 0.4 |

3.2.2 Cement

Ordinary Portland cement was used with a specific gravity of 3.15 and Blaine fineness of 371 $m^2$/kg. The chemical composition is shown in **Table 3.2.**

Table 3.2. Chemical composition of cement

| Items | $SiO_2$ | $Al_2O_3$ | CaO | $Fe_2O_3$ | $SO_3$ | MgO | $K_2O$ | $Na_2O$ | Others |
|---|---|---|---|---|---|---|---|---|---|
| (Wt. %) | 19.4 | 4.6 | 61.1 | 2 | 2.3 | 3.3 | 0.7 | 2 | 4/6 |

3.2.3 Fine aggregate

Riverside sand with a maximum size of 5 mm, water absorption of 3.5%, and saturated surface dry density of 2.72 was used.

3.2.4 Alkaline activator

The used of sodium silicate (SS) had a chemical composition of 29.40 wt.% $SiO_2$, 14.70 wt.% $Na_2O$%, and 55.90 wt.% $H_2O$ mixed with Sodium hydroxide solution with a molarity of 8 to adjust the Ms and $Na_2O$%. The activator solution was prepared and kept at laboratory temperature for 24 h to cool.

3.2.5 Superabsorbent polymers

Angular covalently crosslinked sodium polyacrylate SAP particles (**Fig. 3.2**). The size range of SAPs was from 90 to 850 μm with a density of 0.54 g/mL at 25 °C.

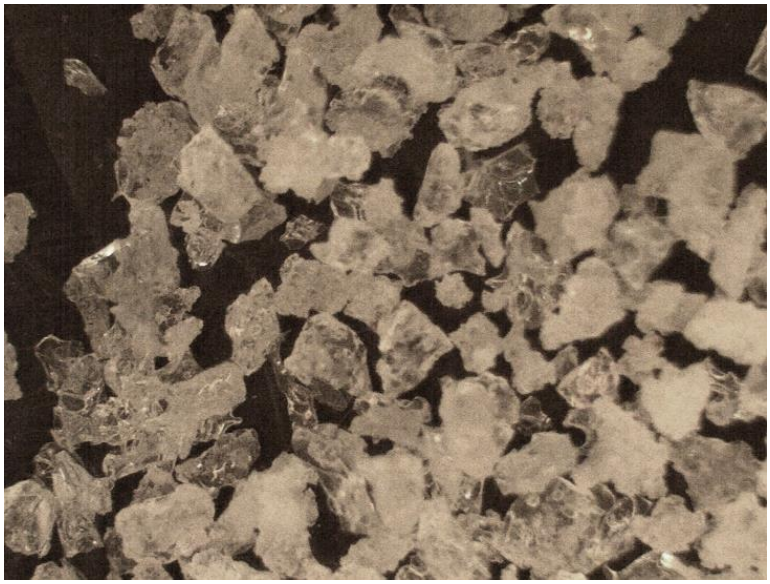

Fig. 3.2. Image of the SAP powders used in the experiments by optical microscope.

### 3.2.6 Shrinkage reducing admixture (SRA)

A commercial glycol ether-based shrinkage reducing admixture was used.

## 3.3 Analytical methods

### 3.3.1 Surface tension and Pore solution chemical analysis

Monitoring the pore solution's surface tension change with hydration time for various SRA dosages was done. The simulated AAS pore solution was prepared and extracted according to Kumarappa et al., (2018). Alkali activated slag pastes were prepared with a solution /slag ratio equal to 2 with various SRA concentrations. The pore solutions were extracted by vacuum filtration method at different ages and stored in sealed containers at a temperature of T=5°C until measurements (**Fig. 3.3**). The surface tension for AAS pore fluids with various dosages of SRA was measured by DCAT 11 instrument.

Fig. 3.3. Extraction of AAS pore solution

Chemical analysis for the extracted AAS pore solution with and without SRA was performed to account for major chemical changes. The ion concentrations (i.e., Ca, K, and Mg) of the extracted AAS pore solution were measured by using Inductively Coupled Plasma Emission Spectroscopy (ICP-AES). The extracted solutions were diluted 10 times with 2% nitric acid solution (i.e., $HNO_3$) and stored until testing at a temperature of 5℃. Moreover, these solutions also were diluted 10 times with distilled water to quantify the concentrations of Si and Na (Ye and Radlińska, 2017).

As SRA is an organic admixture, the total organic content (TOC) of the extracted pore solution was measured to quantify the carbon content following the same procedure reported by Eberhardt, (2011). The pH readings were carried out immediately after extraction of the pore solution using a pH meter.

### 3.3.2 $^{29}$Si solid-state nuclear magnetic resonance (NMR)

A 400 MHz spectrometer instrument was used to conduct $^{29}$Si solid-state nuclear magnetic resonance (NMR) on AAS pastes. At age 7 days, samples were ground to fine powders passing through sieve 150 μm and vacuum desiccated at 40 °C for 1 day. The NMR spectra were executed in a Bruker, Advance III HD spectrometer. The recording conditions for $^{29}$Si were resonance frequency 400 MHz; 4mm wide band with a sample angle rotation of 15 kHz. All

chemical signals were in ppm, and the external chemical shift was referenced to trimethyl silane (TMS) at 0 ppm. Spectral analyses were performed using the commercial software MestReNova (Ye and Radlińska, 2016). The spectra simulations were within 2% of the observed one, and the estimated errors for chemical shifts were less than 0.5 ppm.

### 3.3.3 Thermogravimetric thermal analysis (TGA)

Thermal analysis was performed by Thermogravimetric Analyzer (Q500) to quantitatively estimate the hydration products in the AAS mixtures. At the desired age, samples were crushed and soaked in acetone to stop the hydration. Samples were ground to fine powders passing through a sieve 150 μm and vacuum desiccated at 40 °C for 1 day. Specimens were heated at 10°C/min under a nitrogen atmosphere (Neto et al., 2008).

### 3.3.4 X-ray diffraction

X-ray diffraction (XRD) was conducted on various mixtures to investigate the hydrates assemblage in AAS and identify the crystalline phases. Fine powder samples (i.e., prepared following the same procedure as TGA samples) were placed on glass microscope slides and treated with acetone to stop the hydration (Fernandez-Jimenez and Puertas, 2001). The XRD patterns for various samples were acquired by Bruker, D8 Advance diffractometer with a Cu Ka source operating at 40 kV and 40 mA. The scanning range was from 2Θ of 10° to 60° with a scanning rate of 2°/min.

### 3.3.5 Heat flow evolution

An isothermal conduction calorimeter was used to evaluate the heat evolution for AAS paste samples prepared with a w/b ratio of 0.4 at room temperature. The samples were mixed externally and then loaded into the isothermal calorimeter following ASTM C 1679 (Standard Practice for Measuring Hydration Kinetics of Hydraulic Cementitious Mixtures Using Isothermal Calorimetry). The experiments were run for 7 days and the estimated time between the instant activation of the powder and loading the paste into the calorimeter was about 2 min as shown in **Fig. 3.4**. Hence, the initial 30 min might not be reliable.

Fig. 3.4. Isothermal calorimeter

### 3.3.6 Vacuum water absorption

Cylinder specimens with a diameter of 100 mm and a height of 50 mm were prepared and cured for 28 days. After oven-drying at 60℃ for 48 hours, specimens' side surfaces were sealed by paraffin melted, so the liquid can go through the upper and lower surfaces of samples (**Fig. 3.5**). The specimens were placed in a vacuum chamber and kept under vacuum pressure 0.085–0.095 MPa for 3hr. Then, the water was injected, and all specimens were fully covered with water and kept under vacuum pressure for 1 hour. After that, the specimens were back to normal pressure while submerged in water for 24 hours. After the 24h of water submerging, specimens were immediately wiped and weighted, and an average of three replicates was reported. The vacuum water absorption was calculated according to Eq. (3.1):

$$t = \frac{(M_1 - M_0)}{M_0} \times 100 \qquad 3.1$$

Where t is the % of absorption, $M_0$ is the initial dry mass (g) and $M_1$ is the final mass after absorption (g).

According to Mehta and Monterio, (2013), the open porosity is related to the % of absorption as indicated in Eq. (3.2):

$$P = \frac{(M_1 - M_0)}{V} \times 100 \qquad 3.2$$

Where P is the porosity and V is the volume of the sample in $cm^3$.

Fig. 3.5. Vacuum water absorption setup

### 3.3.7 Characterization of SAPs absorption capacity

In this work, SAP's absorption was determined by the following methods:

(a) Tea bag method

To distinguish the effect of the extracted pore solution of AAS on the absorption of SAP, the absorption of SAP in distilled water and the extracted pore solution of AAS was measured. The absorption of SAP was measured by using the teabag method (Schröfl et al., 2012). According to Eq. (3.3). 0.3 g of dry SAP particles were weighed and assigned as $M_1$, and $M_2$ is the weight of the prewetted tea bag in the corresponding liquid. A tea bag that contains SAP particles hung in a beaker filled with the liquid, the beaker was covered to prevent any carbonation. The teabag was immersed in the corresponding liquid and after a certain time was removed and hung up for 5s to

remove the excess liquid, and then weighted (mass $M_3$) upon time interval of 30 s, 2, 5, 10, 15, 30 min. An average of three teabag measurements was reported. The water absorption rate was calculated by using Eq. (3.3):

$$A = \frac{(M_3 - M_2 - M_1)}{M_1} \quad 3.3$$

(b) SAP Absorption by optical microscope images

To attain a more uniform particles size distribution for SAPs, SAPs particles sieved and the remaining on the sieve #40 (425 μm) were used in this test. The 2-Dimension variations were measured to indicate the SAP volumetric absorption on the base of dry and swollen particles. Images were taken for the dry SAP, then, after immersing the particle in the corresponding liquid for 30 min, the final images were taken to evaluate the changes (Wang et al., 2009). The 2-D dimension changes were measured by a microscope roller and were verified by ImageJ software. The average volume of three particles was measured by assuming a spherical shape.

### 3.3.8 Internal relative humidity (IRH)

The internal relative humidity (IRH) was monitored using a humidity sensor installed inside cylinder specimens 100mm in length and 50 mm in diameter. After casting, a plastic rod with a 20mm diameter was inserted at the cylinder specimen's center to create a hole (50 mm depth) (Chen et al., 2021). At the final set, the rod was removed and replaced by a PVC tube to a depth of 30 mm to support and maintain the sensor at the designated location (**Fig.3.6**). The tube's opening and samples were covered by plastic films and sealed to prevent moisture exchange. Samples that were tested under drying conditions were demolded after the setting time and kept in an environmental chamber with the shrinkage prisms. Sensors with an accuracy tolerance of ±1.5% were inserted inside the hole and connected to a data acquisition system. Data were collected continuously for 28 days. All reported results were the average of three replicate readings.

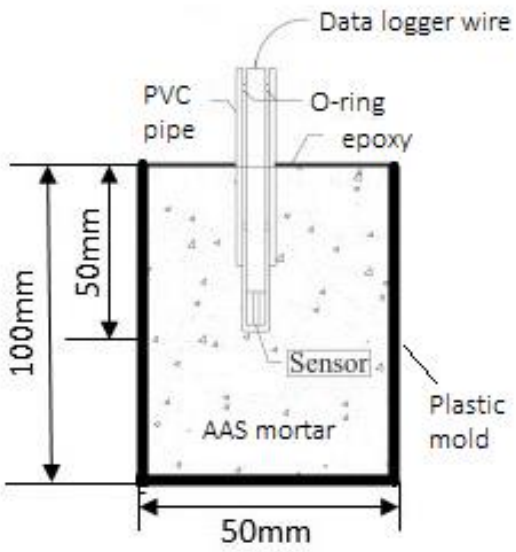


Fig. 3.6. The cross-section for internal relative humidity setup

### 3.3.9 Microstructure investigations

#### 3.3.9.1 Micro-computed tomography (micro-CT)

A micro-CT scanner Bruker, Skyscan1172 was used. The samples were first cast into a small plastic mold with 5mm×10mm and a height of 70mm. After casting, the mold was sealed by paraffin film until testing age. The X-ray source tube worked at 100 keV/60 mA. 1200 images were acquired on a detector (2000 x 1000 pixels) with a resolution of 6 μm. The 3D construction of the dataset was carried out with dragonfly (Chung et al., 2019).

#### 3.3.9.2 Measurement of specific surface ($N_2$-BET)

BET was conducted on tested mixtures with and without SRA to investigate its effect on AAS's pore structure. Specimens were cast in sealed vials for 7 d, crushed into small pieces (4 mm), submerged in acetone to arrest the reaction. The samples subsequently were vacuum dried at 40 °C until a constant mass is achieved. The test was performed using an Automated Surface Area and Porosimetry System (Micromeritics) at a temperature of 77.350 K using nitrogen as sorptive gas. The relative pressure ($P/P_0$) ranges from 0.05 to 0.995. The pore size distribution was determined using the adsorption branch by the Barrett-Joyner-Hallenbda method (BJH) (Barret et al., 1951). The surface area was calculated with Brunauer, Emmett, and Teller (BET) method (Brunauer et al., 1938).

#### 3.3.9.3 Mercury intrusion porosimeter (MIP)

The pore structure characteristic was evaluated by using Autopore IV 9500, Micromeritics to explain the effect of the internal curing on the internal porosity. After 7 days of curing the sample was broken and a central sample was taken for the testing and soaked in acetone to stop the hydration and then was vacuum dried to a constant weight at 40 ℃. The surface tension of the mercury was 485 dynes/cm and with a contact angle of 130° (Webb, 2001).

#### 3.3.9.4 Microscopic examination

AAS cube paste samples with a side length of 20 mm were prepared. At 28 days, a small piece with 10mm thickness was taken from the middle by a saw and soaked in isopropanol until testing. Before testing, the sample was vacuum desiccated at 40°C for 1 day. Then the surface was polished by using sandpaper with a grit size of 600. To increase the conductivity of the surface and avoid charging during imaging, the surface was coated with a thin gold layer. The microstructure was detected under the back-scattering model (BSE). Micrographs were taken from fractured surfaces and Energy-dispersive X-ray spectroscopy microanalysis (EDX) was applied on these surfaces to detect the reaction products (Ben Haha et al., 2010).

### 3.3.10 Shrinkage measurements and mass loss

Autogenous and drying shrinkage was measured using 25 × 25 × 285 mm following ASTM C 157 (Standard Test Method for Length Change of Hardened Hydraulic-Cement Mortar and Concrete). For autogenous shrinkage measurements, sealed specimens were wrapped with four layers of polyethylene sheets and a layer of paraffin wax membrane to prevent moisture loss. Drying shrinkage specimens were exposed to a controlled condition (T = 23±2C° and 45±5% relative humidity) inside an environmental chamber.

The free shrinkage deformations were measured using a comparator provided by a dial gauge with an accuracy of 10 $\mu$m/m. The same prismatic specimens 25 × 25 × 285 mm were used to measure mass loss. Specimens were kept at the same exposure condition after measuring the initial mass using a balance with an accuracy of 0.01 g. Mass measurements were taken for all prisms along with measurements of total strains up to 28 days. All reported results represent the average of at least three specimens.

### 3.3.11 Compressive strength and setting time

Compressive strength was evaluated using cubic specimens 50 ×50 ×50 mm. The samples were cured in humid conditions (22°C and 88±5% RH) after demolding and tested at ages 3-, 7-, and 28-days following ASTM C109 (Standard Test Method for Compressive Strength of Hydraulic Cement Mortars (Using 2-in. or [50 mm] Cube Specimens).

Setting time was evaluated according to ASTM C191 (standard test method for time of setting of hydraulic cement by Vicat needle)

# Chapter 4 - Effect of activator nature on property development of alkali-activated slag binders

## 4.1 Introduction

Waterglass is a combination of sodium silicate and sodium hydroxide solutions. The reactivity of this activator is mainly controlled by sodium oxide content ($Na_2O$%) and activator silicate modulus (Ms). Sodium oxide content ($Na_2O$%) reflects the ratio of sodium oxide in the activator by binder weight, while Ms is the molar ratio of silicon oxide to sodium oxide ($SiO_2$/ $Na_2O$) in the activator. However, the effect of $Na_2O$% and Ms on the autogenous and drying shrinkage of AAS mortars is still under debate. in order to design the AAS system, it is essential to understand the significance of each activator parameter, and which one has more contribution to a specific property of AAS. Therefore, the influence of activator nature on the property development of AAS will be discussed in this chapter.

## 4.2 Specific methods and approaches

In a first step effects of $Na_2O$ %, in the range of (4% - 8%), and Ms ranges from 0.5 to -1.5, on the reaction kinetics, setting time, compressive strength, autogenous and drying shrinkage were evaluated. Then, a design of experiment (DOE) was used to quantify the effects of $Na_2O$ % and Ms value on AAS properties. Three full factorial design was applied, whereas three levels of $Na_2O$ % and Ms were selected to cover a reasonable range of solution chemistries which are (4, 6, 8%) and (0.5,1, 1.5), respectively. Mixtures configurations with different levels of $Na_2O$ % and Ms values are shown in **Table 4.1**. For each mixture, the first number refers to $Na_2O$%, while the second number indicates the Ms values. For instance, M805 and M815 codes refer to mixtures with 8% $Na_2O$% and Ms=0.5 and Ms=1.5, respectively.

Table 4.1. Summary for tested mixtures and variables ranges

| Mixture ID | $Na_2O$% | Ms |
|---|---|---|
| M405 | | 0.5 |
| M410 | 4% | 1.0 |
| M415 | | 1.5 |
| M605 | | 0.5 |
| M610 | 6% | 1.0 |
| M615 | | 1.5 |
| M805 | | 0.5 |
| M810 | 8% | 1.0 |
| M815 | | 1.5 |

## 4.3 Results and Discussion

### 4.3.1 Setting times

**Figure 4.1** presents the initial and final setting times for pastes with various Ms and $Na_2O$% values. Increasing $Na_2O$% and/or Ms shortened the setting time. For example, at Ms=1, increasing $Na_2O$% from 4% to 8% shortened the setting time by about 72%. This can be attributed to the higher pH at a high $Na_2O$% (higher $OH^-$ concentration), which helps the dissolution of calcium ($Ca^{2+}$) from the slag particles leading to a higher reaction rate (Chang, 2003). Increasing $Na_2O$% from 6% to 8% slightly shortened setting time. This found can be ascribed to the rapid formation of a high amount of initial C-A-S-H products and a reduction in calcium solubility (Yip and Van Deventer 2003; Ravikumar and Neithalath, 2012). On the other hand, at low $Na_2O$% (i.e., 4%), increasing Ms from 0.5 to 1.5 shortened the initial and final setting time by 60% and 33%. This result indicates that more soluble silica is available in the solution, which accelerates the reaction leading to a faster setting and hardening process (Atis et al. 2009, Bernal et al., 2011). One interesting point is that the effect of Ms at high $Na_2O$% (e.g., 6% and 8%) was minor. Hence, it could be concluded that $Na_2O$% will dominate the setting property for AAS rather than Ms.

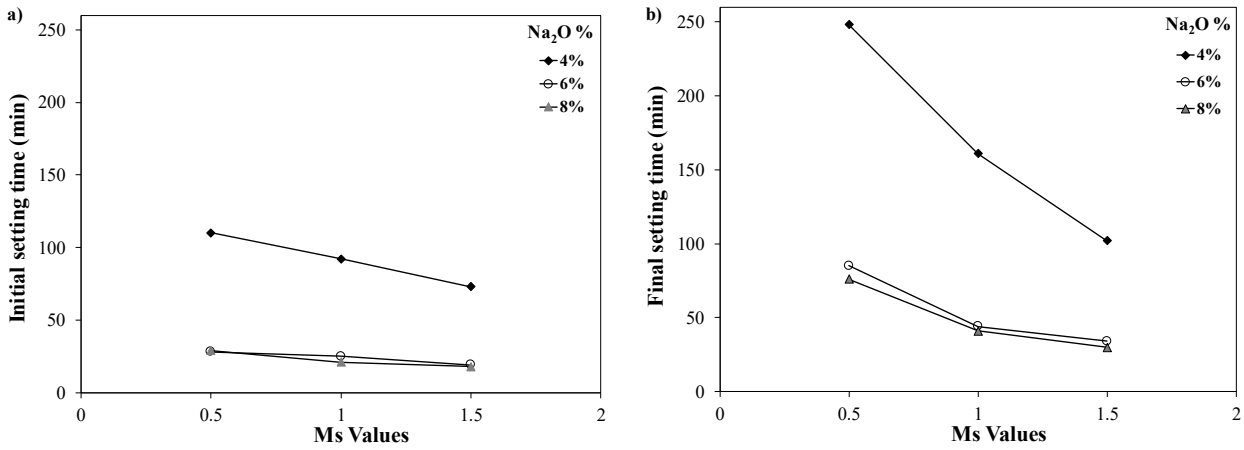

Fig. 4.1. Figure 1. Setting times for pastes (a) Initial times and (b)final setting times

### 4.3.2 Heat of Hydration

#### 4.3.2.1 Effect of $Na_2O$% on the heat evolution rate

**Figure 4.2** (a,b) presents the heat evolution rates of AAS activated by different dosages of $Na_2O$%, and various Ms. These curves exhibited two peaks. The initial peak, which is narrow and intense, occurred within the first few hours of mixing, due to the dissolution of slag. This initial peak was followed by an induction period. The second peak which is called the accelerated peak appeared after the induction period and is attributed to the formation and precipitation of reaction products (e.g., hardened gel) (Ravikumar and Neithalath, 2012). **Figure 4.2b** illustrates the heat evolution rates of AAS activated by different ratios of $Na_2O$% with Ms = 1. The higher the $Na_2O$% was, the higher were the initial and accelerated hydration peaks. Additionally, the higher the $Na_2O$ %, the shorter was the induction period. For instance, the accelerated peak for mixture M810 was about 8.35 kJ/kg/h and appeared after 9.5 hrs while M410 was about 3.96 kJ/kg/h and appeared after 35.6 hrs. This is due to the higher alkalinity for mixture M810 (i.e., $Na_2O$% =8%) since higher sodium oxide definitely will lead to higher pH. For instance, the difference in alkalinity for mixtures with $Na_2O$% of 4% and various Ms is presented in Table 3. The measured pH values for activators with Ms 0.5, 1, and 1.5 were 13.7, 13.3, and 12.9, respectively. The higher percentage of sodium oxide at low Ms resulted in higher alkalinity. This was also confirmed by measuring the electrical conductivity for the used activators, as hydroxide ions have higher conductivity compared with the other ions presented in these activators (Snyder et al., 2003).

Increasing the alkalinity of the activator solubilizes the water-impermeable layer on the surfaces of slag particles, contributing to faster reaction rates and product formation (Song et al., 2000). This trend is also noticed for other mixtures at the same Ms value (e.g., 0.5), as shown in **Fig. 4.2a**.

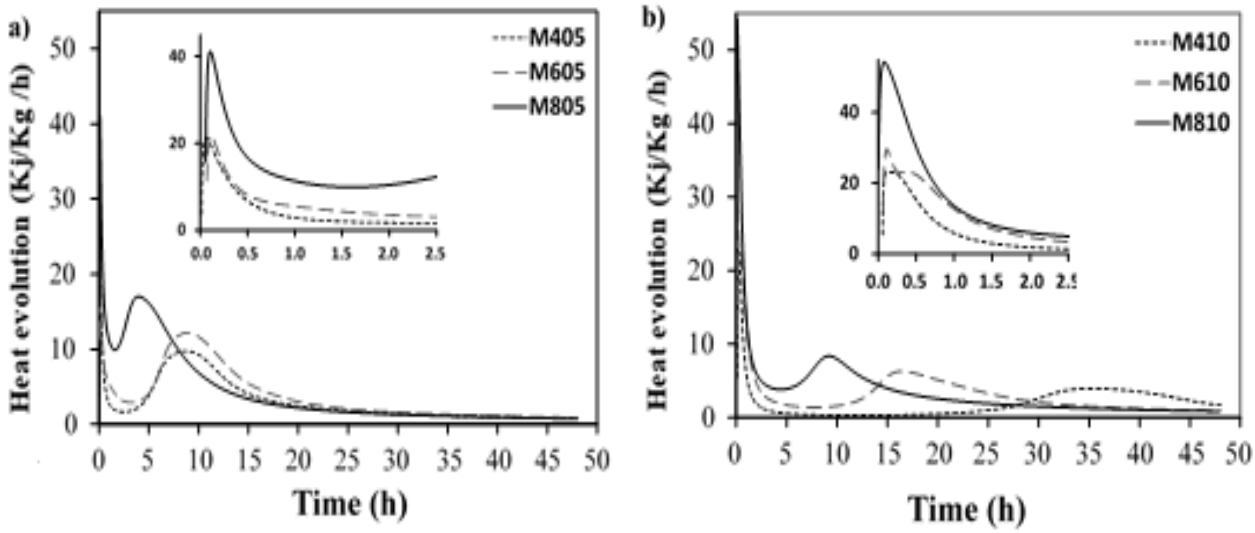


Fig. 4.2. Heat flow of reaction for alkali-activated slag pastes activated with different $Na_2O$% weight and constant Ms. (a) Ms=0.5, (b) Ms=1

4.3.2.2 Effect of Ms values on the heat of hydration rate

**Figure 4.3**(a,b) shows the heat evolution of AAS paste activated by different Ms and the same $Na_2O$ %. At higher Ms values, the accelerated peak value decreased and shifted to a later time, indicating a slower reaction. For instance, at $Na_2O$ % of 6%, the accelerated peak value for mixture M605 (i.e., with Ms= 0.5) was about 12.2 kJ/kg/h and occurred at 8.3 hrs, while mixture M615 (i.e., with Ms= 1.5) showed 3.6 kJ/kg/h after 30.2hrs. This can be attributed to the reduction in alkalinity by increasing the activator Ms values, which led to a delay in the reaction (**Table 4.2**). In conclusion, with increasing silica modulus, the value of accelerated peak decreases, and the induction period lasted longer (Ravikumar and Neithalath, 2012).

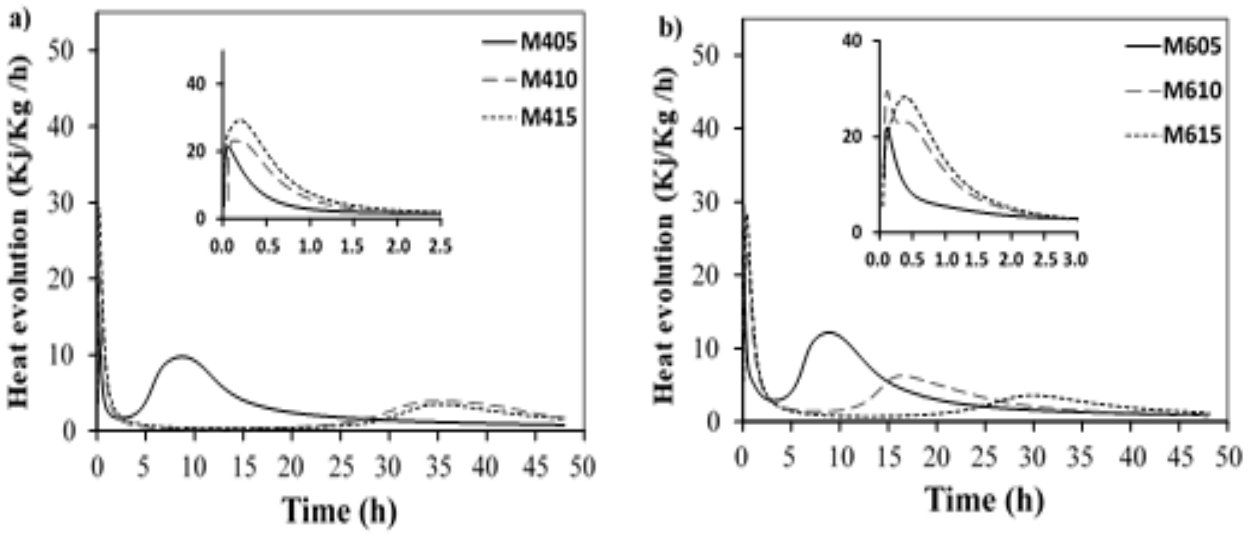


Fig. 4.3. Heat flow of reaction for AAS activated with different Ms (a) 4% $Na_2O$ and (b) 6% $Na_2O$

Table 4.2 Effect of Ms on the pH and conductivity

| Mixture ID | $Na_2O$% | Ms | pH | Conductivity (S/m) |
|---|---|---|---|---|
| M405 | | 0.5 | 13.70 | 9.3 |
| M410 | 4% | 1.0 | 13.30 | 8.4 |
| M415 | | 1.5 | 12.90 | 7.2 |

4.3.2.3 Cumulative heat of hydration. `

**Figure 4.4** shows the corresponding cumulative heat of hydration for all tested AAS mixtures. In agreement with previous results, at the same Ms, increasing $Na_2O$% resulted in a higher cumulative heat of hydration. For instance, at Ms= 0.5, mixture M805 showed the highest cumulative heat, followed by M605, and the lowest was M405. On the other hand, increasing Ms (lower alkalinity) decreased the released cumulative heat at the same $Na_2O$%. For example, mixtures M805 (i.e., with 8% $Na_2O$ and Ms=0.5) showed the maximum cumulative heat value which is 201 KJ/kg slag, while for mixture M810 and M815 with Ms= 1and 1.5, the values were about 142 kJ/kg slag 112 KJ/kg slag, respectively.

Consequently, the heat evolution analysis indicated that increasing both $Na_2O$% and Ms will lead to a higher initial peak, which means higher dissolution and formation of the initial hydration products. Comparing with the setting time results, it seems that for AAS, initial setting times appear towards the early part of the induction period. In contrast with OPC, whereas the final

setting time synchronizes roughly at the end of the induction period or the beginning of the second peak, as shown in **Fig. 4.5**. For instance, mixture M815 (i.e., with 8% $Na_2O$% and Ms=1.5) showed a long induction period, and the accelerated peak appeared after about 28 hrs. However, the initial setting time occurred relatively quickly (i.e., in about 30 min). Hence, for alkali-activated slag, the evaluation of the structure formation by setting time cannot be assuredly related to heat evolution.

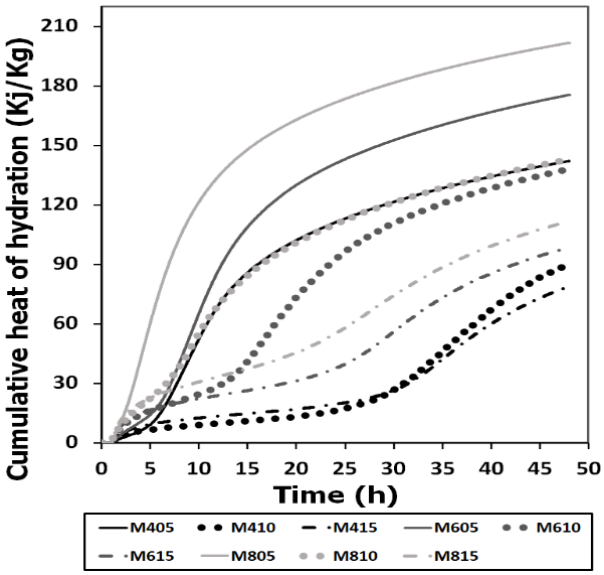


Fig. 4.4. Effect of sodium silicate with different Ms and $Na_2O$% on cumulative heat of hydration of AAS pastes

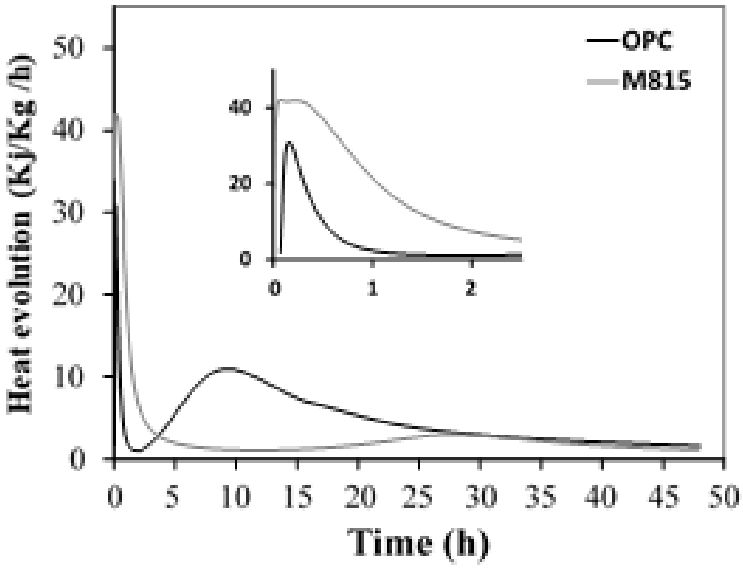


Fig. 4.5. Heat flow of reaction for alkali-activated slag pastes compared to that of OPC paste

### 4.3.3 Compressive strength

**Figure 4.6** (a, b, c) illustrates the compressive strengths for all tested AAS mortar mixtures. Generally, compressive strengths increased as the dosage of $Na_2O$% increased. This can be attributed to the high $OH^-$ ions concentrations, which act as scissors break Si-O bonds to release more $Si^{4+}$ from the slag particle surface. This promoted the formation of a higher amount of hydration products, especially C-S-H gel leading to high compressive strength (Li et al., 2017). This agrees with the heat of hydration results, in which higher $Na_2O$% was found to intensify the reaction. For instance, at age 7 days, mixture M805 (i.e., with 8 % $Na_2O$ and Ms=0.5) achieved compressive strength around 43 MPa, which is about 64% higher than that of mixture M405(i.e., with 4 % $Na_2O$ and Ms=0.5).

Interesting that at very low $Na_2O$% (i.e., 4%), mixtures with Ms (1,1.5) did not gain any strength at an early age (up to 2 days). The low initial strengths of these mixtures can be attributed to the reduction in the pH by increasing Ms. Moreover, as found in the heat evolution section, these mixtures exhibited very long induction periods. Contrarily, at later ages, the compressive strength values increased by increasing Ms ratios. Basically, as the hydration undergoes, more

silicate anions are incorporated, forming more C-S-H with a low C/S ratio, which has a higher binding ability (Aydın and Baradan, 2014; Ben Haha et al., 2010).

Moreover, the poorly packed structure converted into a dense and compact structure by increasing Ms value leading to a lower porosity (Feng et al., 2004; Aydın and Baradan, 2014). Additionally, higher Ms contributed a higher amount of reactive silica that enhances the geo-polymerization process and favors the formation of a larger amount of C-S-H gel. Consequently, much higher mechanical strength. It is clear from Figure 6 that increasing $Na_2O$% from 4% to 6% increased the 28-compressive strength. However, a slight change occurred by increasing $Na_2O$ from 6% to 8%. This may be ascribed to the reduction of the calcium solubility by increasing $Na_2O$% as a result of the formation of calcium hydroxide around the slag particles, which also prevents the slag hydration and production of more C-S-H gels. This thin layer was formed because of a reaction between $Ca^{2+}$ from the slag and the excessive $OH^-$ ions from the activator, which led to a reduction in $Ca^{2+}$ solubility (Yip and Deventer, 2003; Yip et al. 2005).

The 28 days compressive strength values increased as Ms values increased from 0.5 to 1 and 1.5. This result contradicts previous work findings (Atis et al., 2009; Aydin and Baradan, 2014), whereas a reduction in the compressive strength was achieved by increasing Ms from 1 up to 1.5. The contradiction in the 28-compressive strength trend can be ascribed to the difference in the basicity coefficient ($K_b$) of the used slag, whereas it was reported that GGBS has a variable composition reliant on the raw materials (Bakharev et al., 1999; Wang et al., 1994). The used slag in this work is classified as a basic slag ($K_b$=1.06) while the slag that is used in studies (Atis et al., 2009; Aydin and Baradan) is considered an acidic one. According to authors, Wang et al., (1994), the optimum Ms ratios to gain the highest 28-compressive strength for basic slag is between (1-1.5). This agrees with the obtained compressive strength in this work. It can be said that at a given $Na_2O$ dosage, the optimum silica modulus is found to be higher when the slag alkalinity is higher. Furthermore, the 90-compressive strengths increased by an average of 17% and 28% as $Na_2O$% increased from 4% to (6 and 8%) at the same Ms, while varying Ms values showed a lower effect.

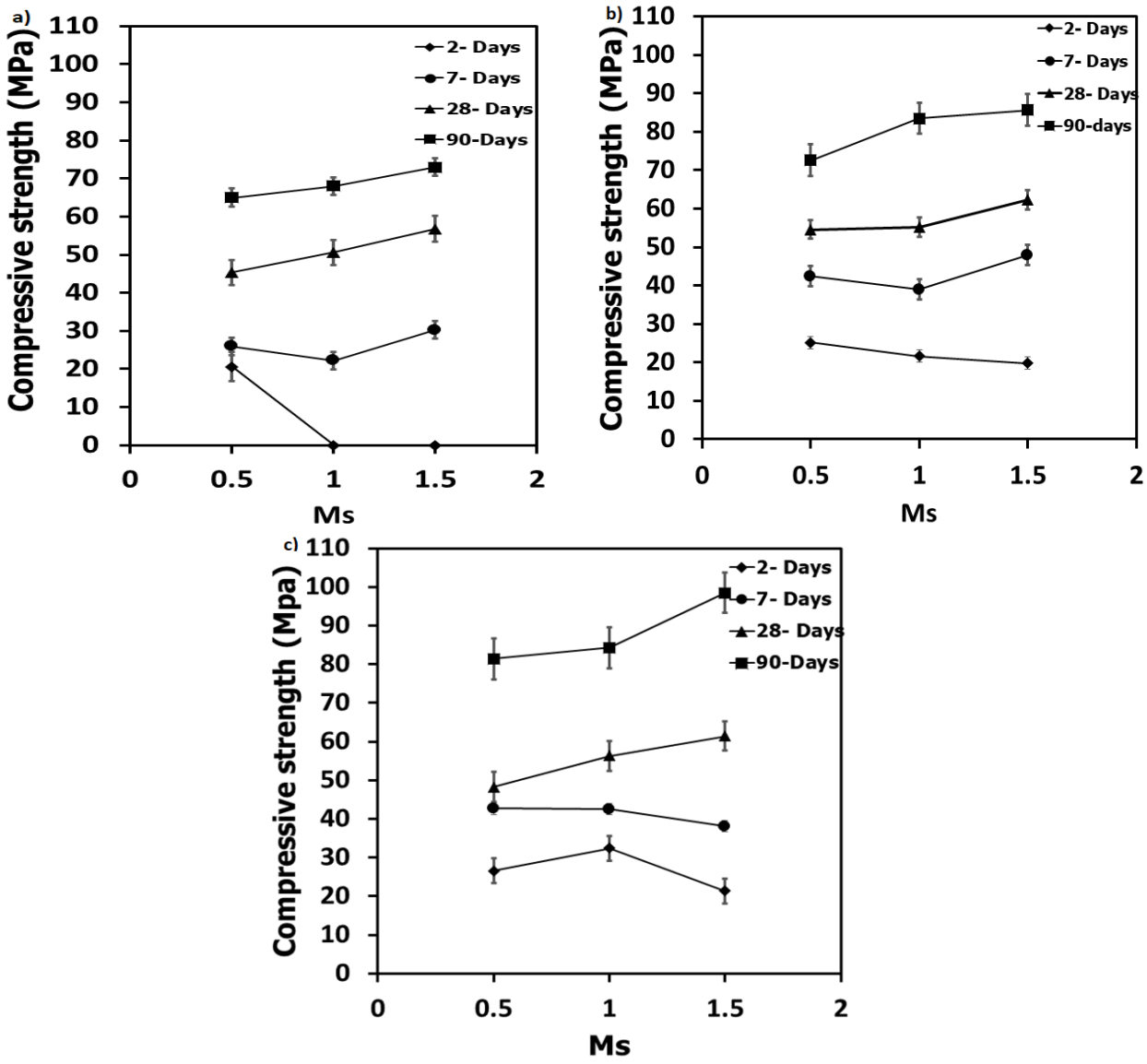


Fig. 4.6. Compressive strength AAS activated by sodium silicate with $Na_2O$% of (a) 4%, (b) 6% and (c) 8%

### 4.3.4 Autogenous shrinkage

Chemical shrinkage and self-desiccation are the main driving forces for autogenous shrinkage (Neto et al. 2008). Measured autogenous shrinkage for tested AAS mixtures with different $Na_2O$ % and Ms values are presented in **Fig.4.7**. Generally, increasing either $Na_2O$% or Ms ratio resulted in a higher autogenous shrinkage. For instance, at the same Ms (i.e., 0.5,1 and 1.5), increasing $Na_2O$% from 4% to 8% led to about an average increment of 88% in the autogenous shrinkage. However, the autogenous shrinkage average increment was in the range of 15% by increasing $Na_2O$% from 6% to 8% at the same Ms value (i.e., 0.5,1 and 1.5). On the other hand, at the same $Na_2O$% (i.e., 4%,6%, and 8%), increasing Ms value from 0.5 to 1.5 resulted in around 78% increase in autogenous shrinkage as shown in **Fig.4.7**. This indicates that both Ms and $Na_2O$% had significantly affected the autogenous shrinkage. For example, for all mixtures, autogenous shrinkage measured up to the first 7 days represented about (50% - 60%) of the final shrinkage. Activator $Na_2O$ % and Ms ratio play a crucial role that significantly affected the degree of reaction and the development of microstructure (i.e., porosity) (Ben Haha et al., 2010; Feng et al., 2004; Aydın and Baradan, 2014). Increasing the activator $Na_2O$ % intensified the polymerization process, leading to a higher chemical shrinkage along with refining pores (i.e., increases the volume of mesopores and reduction in the total porosity) (Neto et al., 2008).

Generally, at the same Ms value, increasing $Na_2O$% led to a higher surface tension value. This is attributed to the high pH environment by increasing $Na_2O$%, which boosts slag dissolutions (Dier et al. 2014). Therefore, the pore solution will be loaded with Al, Si, and Na ions. This is expected to increase its surface tension at the same solution to binder ratio (Shi and Day, 1995). Moreover, increasing Ms values at the same $Na_2O$% led to a higher surface tension too. In the pore solution, $[SiO4]^{4-}$ ions concentration increases as Ms value increased, leading to more soluble silica in the solution. This allows $[SiO4]^{4-}$ ions to polymerize as not enough $Ca^{2+}$ is available to react, leading to higher surface tension in the pore solution (Shi and Day, 1995; Kumarappa et al., 2018). The surface tension of water was calculated to be 77mN/m, which is about half that of the sample with 8% $Na_2O$. According to Laplace equation Eq. (2.1), the magnitude of capillary stresses ($P_{cap}$), which is the main factor dominating shrinkage, depends on both the radius of the largest pore (r) and the surface tension of the pore solution ($\gamma$) (Radlińska et al. 2008).

This could explain the increase in the autogenous shrinkage associated with increasing activator $Na_2O$ % and Ms ratio. This agrees with previous results reported by (Neto et al. 2007; Chen and Brouwers, 2007).

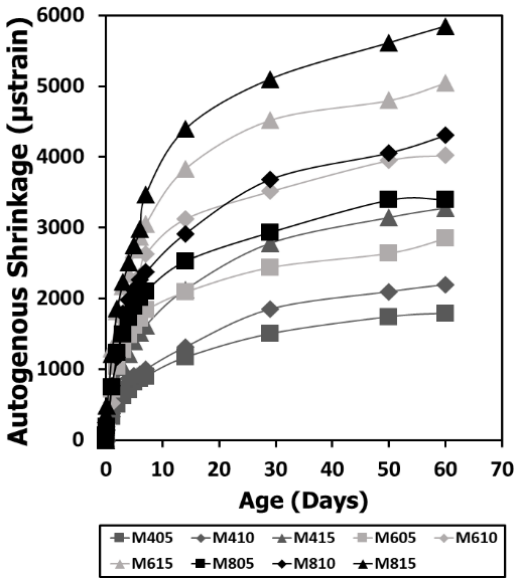


Fig. 4.7. Autogenous shrinkage of ASS mortars

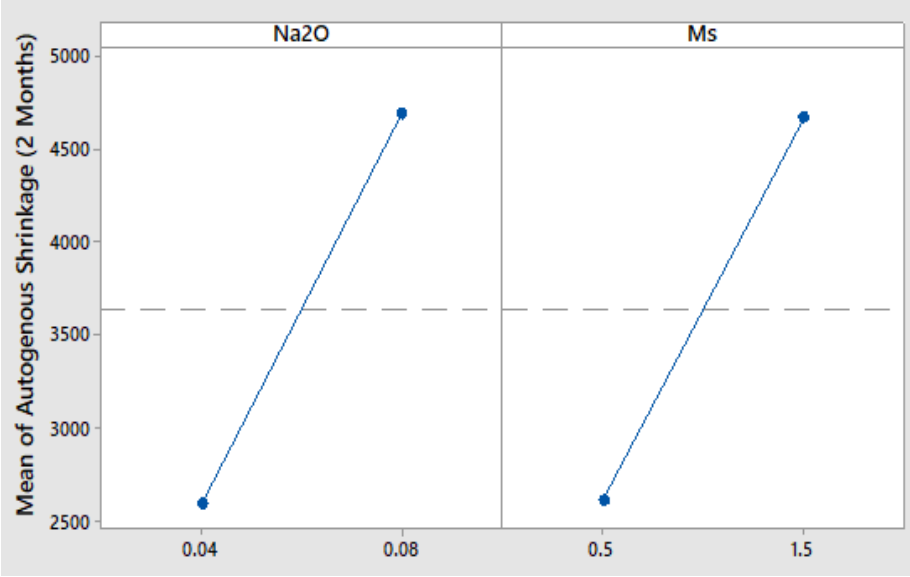


Fig. 4.8. Relationship between autogenous shrinkage and activator parameters

### 4.3.5 Total shrinkage

Total shrinkage followed the same trend for autogenous shrinkage. The higher the $Na_2O$ % and Ms value, the greater the total shrinkage. This is expected as total shrinkage reflects both autogenous and drying shrinkages. For example, at Ms = 0.5, increasing $Na_2O$% from 4% to 8% led to about a 45% increase in the total shrinkage. On the other hand, at the same $Na_2O$% (i.e., 4%,6%, and 8%), the total shrinkage for mixture with Ms =1.5 was about 2.5 times that with Ms= 0.5, as shown in **Fig.4.9**. This indicates that Ms had a more significant influence on the total shrinkage than that of $Na_2O$%.

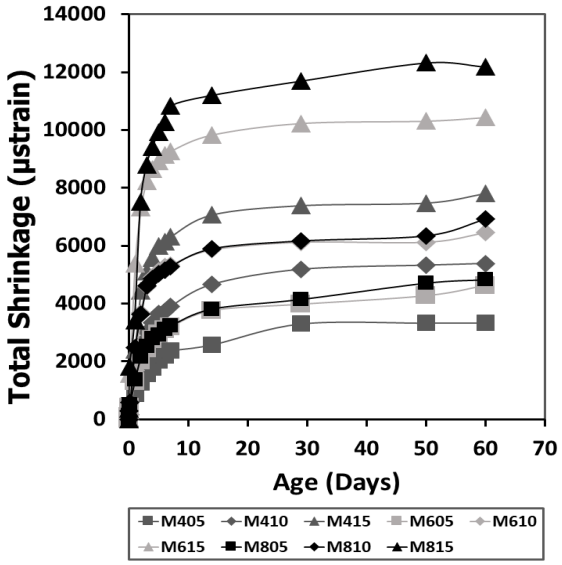


Fig. 4.9. Drying shrinkage of ASS mortars

Autogenous shrinkage occurs under sealed conditions. However, there is an interaction between it and the total measured shrinkage (i.e., exposed to drying conditions). As shown in **Fig. 4.10**, the contribution of autogenous shrinkage in the total shrinkage is more significant for samples with higher Ms, which can be attributed to the higher percentage of mesopores and the capillary pressure. On the other hand, under drying conditions, an additional shrinkage mechanism to that reported at sealed conditions (autogenous) contributes to the total shrinkage (Neto et al., 2008). During the initial hydration phases, silica or silica-rich gel is formed, which are rich in silica hydro silicates and silica acid (Lukowski et al., 1983). At alkaline media and high pH, the silica acid will polymerize into silica gel and condense. The formed silica gel will possess high water content. Consequently, as drying undergoes, the silica gel starts to evict water and shrink (Shi et

al., 1992; Gao et al., 2016; Wang et al., 1995; Kutti, 1992). Simultaneously, several particle-to-particle bonds in the structure gradually break (Ye and Radlinska, 2016; Thomas et al., 2017). Therefore, at higher Ms ratios, higher drying shrinkage is experienced (**Fig.4.10**).

Furthermore, the silica gel that formed in AAS activated by sodium silicate solution contains a low Ca/Si ratio and tend to shrink more, especially for samples with high Ms (Hu et al., 2019; Shi et al., 2006). According to a recent study (Chen et al., 2021), increasing Ms led to higher shrinkage due to the silicate gel structure's spontaneous volumetric contraction during the silicate polymerization process.

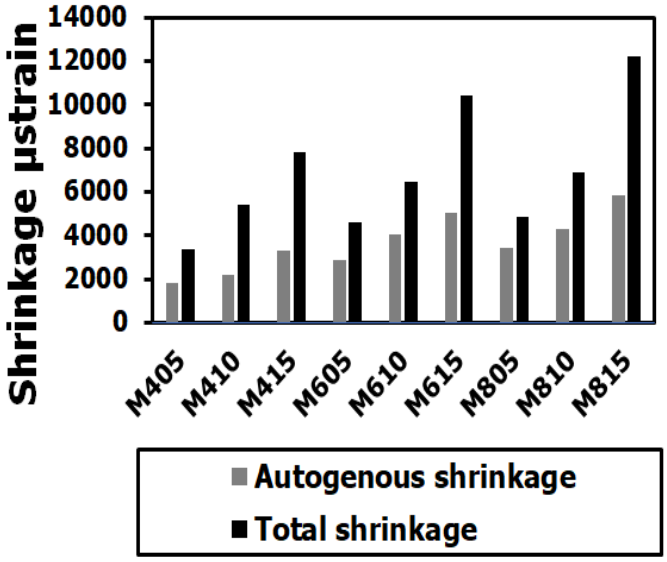


Fig. 4.10. Comparative graph of drying and autogenous shrinkage of AAS mortars

Shrinkage and compressive strength for all tested mixtures were illustrated in **Fig.4.11.** The relationship between the total shrinkage and compressive strength of AAS mixtures showed that mixtures with Ms =0.5 would exhibit low shrinkage while achieving comparable strength for those with higher Ms values regardless of $Na_2O$%.

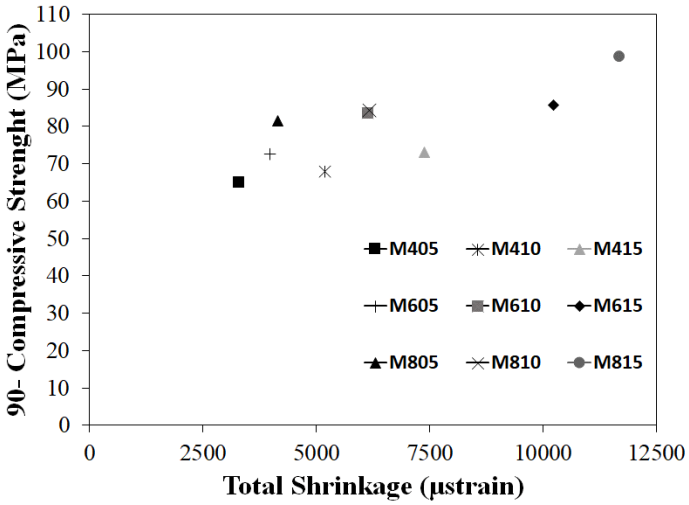


Fig. 4.11. The relation between the total shrinkage and the 90 -compressive strength

### 4.3.6 Mass change characteristics

**Figure 4.12** (a,b) presents the influence of $Na_2O$ % and Ms values on the mass loss for tested AAS mixtures. Generally, mass loss is highly dependent on the $Na_2O$ %. The higher the $Na_2O$ %, the lower the mass loss, which occurred over a shorter period. For instance, at Ms=0.5, increasing $Na_2O$ % from 4% to 8% led to about 72% reduction in the mass loss. This can be attributed to the refinement of pores as a result of increasing $Na_2O$ %, as explained earlier, and more water consumed by hydration reactions. Mass loss and emptying fine pores will be harder than larger pores. Figure 13(b) illustrates the effect of Ms on the moisture loss at 8% $Na_2O$. Samples with higher Ms exhibited higher mass loss and evaporation rates. For instance, mixtures with Ms=1.5 lost weight about 2.5 times higher than that for mixture with Ms=0.5. This, in agreement with the, reported drying shrinkage, as explained in the following section.

**Figure 4.13** illustrates the correlation between measured total shrinkage and mass loss for all AAS mixtures. The slopes for shrinkage-mass loss curves reflect the rate of shrinkage development concerning the mass-loss rate. Increasing the $Na_2O$ % and Ms values led to a steeper slope. Hence, at higher $Na_2O$ % and Ms value, the total shrinkage increasing rate was higher than the mass-loss rate. Moreover, near the end of the investigation period, there was an increase in shrinkage while the mass loss was almost null. This indicates that shrinkage is not

entirely related to mass loss. This agrees with previous findings that shrinkage for sodium silicate solution activated slag cannot be quantified by mass loss (Collin and Sanjayan, 2000). This behavior confirms the visco-elastic/visco-plastic response of AAS to the effective capillary pressure. This pronounced viscous characteristic of AAS (shrinking without losing water), is not due to the gradual loss of moisture but most probably attributed to the microstructural redistribution and rearrangement (Ye and Radlińska, 2016a).

Moreover, researchers referred the high reported shrinkage to the incorporation of alkali cation with C-A-S-H nanostructure, which decreases its stacking regularity. Hence, make the C-A-S-H unstable, easier to collapse, rearrange, and redistribute (Ye and Radlińska, 2016a).

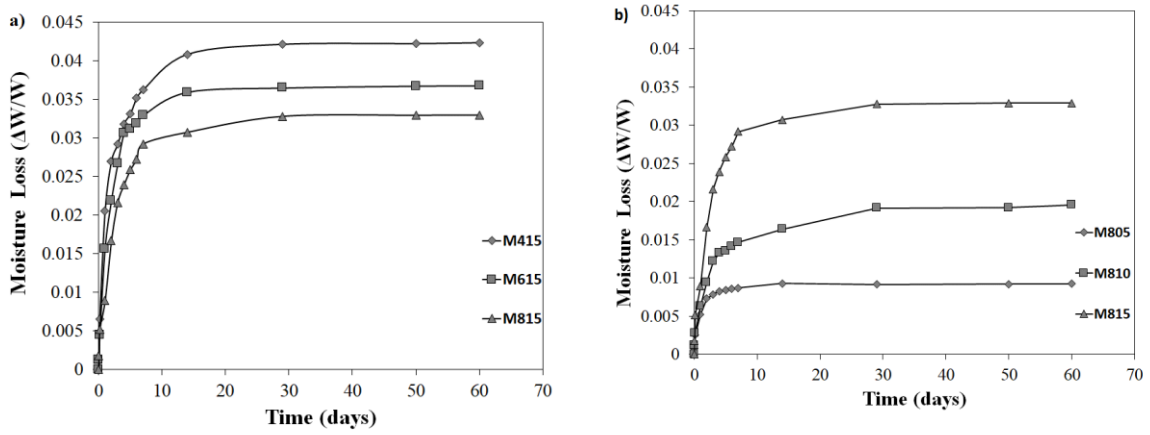


Fig. 4.12. (a) Effect of $Na_2O$% on the Mass loss, **(b)** Effect of Ms on the Mass loss at 8% $Na_2O$

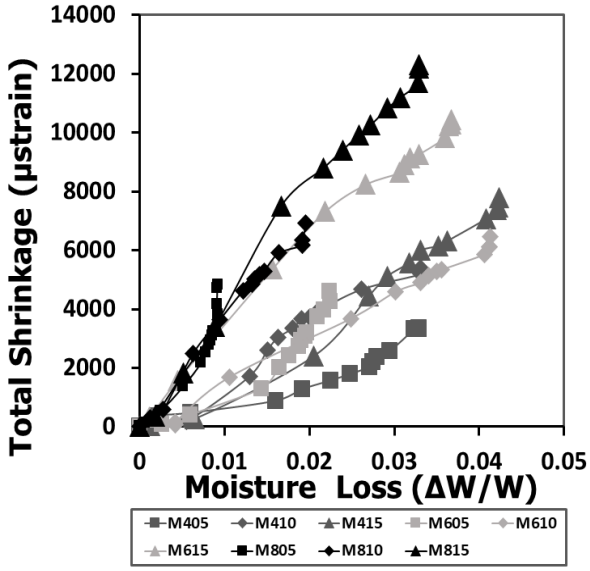


Fig. 4.13. Drying shrinkage versus moisture loss

## 4.4 Statistical evaluation of experimental results

A successful statistical tool that has been applied in several engineering applications is the analysis of variance (ANOVA) (Gorhan, 2015). In ANOVA, F-test is used to evaluate the significance of each parameter on the targeted responses. It compares the variation in each response due to a specific parameter with variation within each selected parameter for the null-hypotheses test. P-value is the Prob > F, which is the probability that the model will not explain the variations in the response. The parameter is considered statistically significant if the p-value is less than α, which is the significance level (usually taken =0.05 for engineering applications). If the p-value is greater than 0.1, the parameter is considered statistically insignificant (Mohammed et al., 2012). After that, selected statistical models have generated to estimate and prediction the responses as a function in the considered parameters. In this study, ANOVA was performed to evaluate which of $Na_2O$ %, and Ms significantly affect AAS responses (i.e., properties) using Minitab.

**Table 4.3** shows the ANOVA results for setting time, cumulative heat, compressive strength, total, and autogenous shrinkage.

Table 4.3 ANOVA test results

| Response | Setting Time | Cumulative Heat | Compressive strength | Autogenous shrinkage | Total shrinkage |
|---|---|---|---|---|---|
| Standard deviation | 37.9 | 11.42 | 3.01 | 366.59 | 755.08 |
| $R^2$ value | 82.8% | 96.33% | 96.4% | 95.12% | 95.67% |
| Adjusted $R^2$ | 72.88% | 94.12% | 94.24% | 92.18 | 93.07% |
| F value | 7.49 | 43.72 | 44.64 | 32.46 | 36.83 |
| p- value (Prob> F) p-value | 0.027 | 0.001 | <0.00001 | 0.001 | 0.001 |
| $Na_2O$% | 0.011 | 0.002 | <0.00001 | 0.001 | 0.01 |
| Ms | 0.047 | <0.00001 | 0.002 | 0.001 | <0.00001 |
| $Na_2O$%× Ms | 0.244 | 0.248 | 0.707 | 0.248 | 0.114 |

Comparing the ANOVA and experimental results, $Na_2O$%, and Ms values statically significance effects on AAS properties were confirmed. For instance, for setting time, $Na_2O$% had a p-value of 0.011 compared to 0.047 for Ms. This indicates that increasing the $Na_2O$% will have a higher effect on setting time than that induced by varying Ms. Similarly, for the 90-days compressive strength, $Na_2O$% had more considerable influence than that of the Ms values. On the other hand, Ms is more significant than $Na_2O$ % for cumulative heat released. As discussed above, the delay in appearance of the accelerated peak and the change in peak height seems to be well associated with the activator Ms values, and increasing Ms caused a reduction in the alkalinity. Furthermore, both Ms values and $Na_2O$% had significant effects on autogenous shrinkage, based on the fact of increasing the surface tension of the pore solution and refinement of the pores, which leads to higher capillary pressure while Ms value had a higher effect on drying shrinkage.

Figure 15, which presents a Pareto chart of the standardized effects for each property. These Pareto charts present the absolute values of the standardized effects from the largest effect to the smallest effect. The plotted line is a reference line to indicate which effects are statistically significant. For instance, the standardized effect of Ms on drying shrinkage is about 9.5 while it is about 4 for $Na_2O$%, which indicates that Ms value contributes more for drying shrinkage property.

The prediction equations for setting time, compressive strength, total, and autogenous shrinkage are shown. Eqs. (4.1 to 4.4) The adjusted $R^2$ of the models ranged from 0.82 to 0.96, which is adequate.

| | | |
|---|---|---|
| Final Setting Time (Min) | =504- 5533 $Na_2O$ - 231 Ms+ 2500 $Na_2O$*Ms | (4.1) |
| Compressive strength (MPa) | =30.4+ 556 $Na_2O$ + 10.67 Ms+ 60 $Na_2O$*Ms | (4.2) |
| Autogenous Shrinkage (μs) | =-111 + 28413 $Na_2O$ + 604 Ms+ 23988 $Na_2O$*Ms | (4.3) |
| Total Shrinkage (μs) | =1649 - 10645 $Na_2O$ + 1537 Ms+ 72306 $Na_2O$*Ms | (4.4) |

It must be remarked that the purpose of work is to introduce a new statistical approach, ANOVA analysis, to quantify the effects of activator factors on the performance and properties of AAS. The predicted equations are simply examples of ANOVA analysis based on limited data. **Figure 4.14** represents the Surface respond model for the properties of AAS mortars.

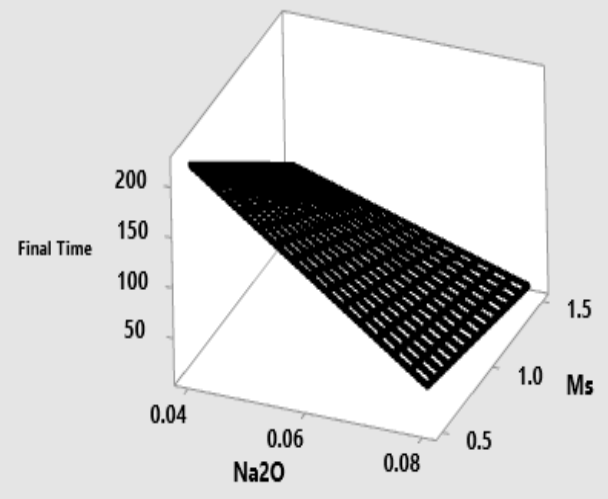


(a). Surface respond model of setting time

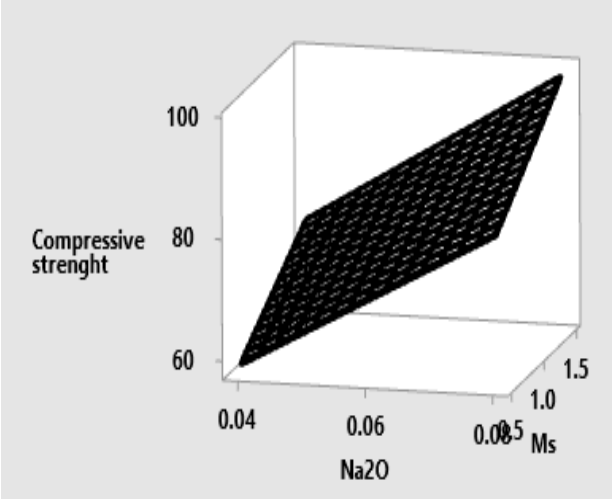


(b). Surface respond model of 90-compressive strength

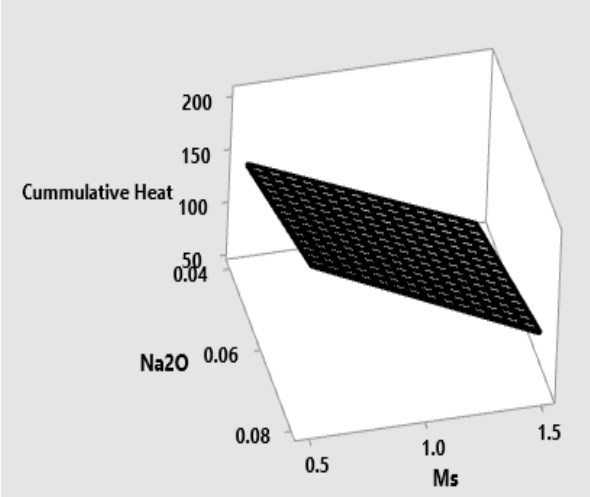


(c). Surface respond model of cumulative heat released

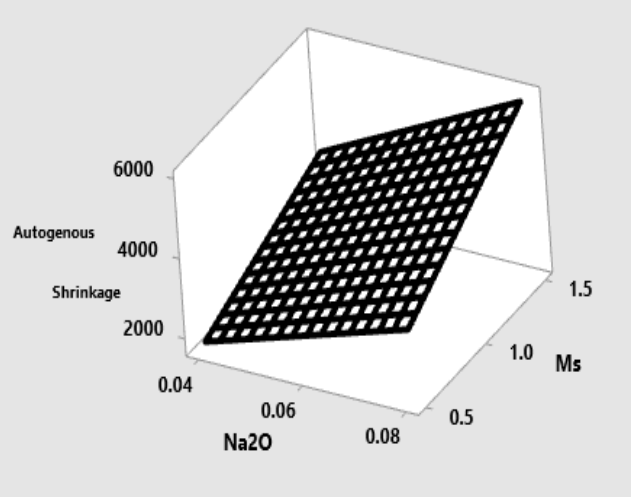


(d). Surface respond model of autogenous shrinkage

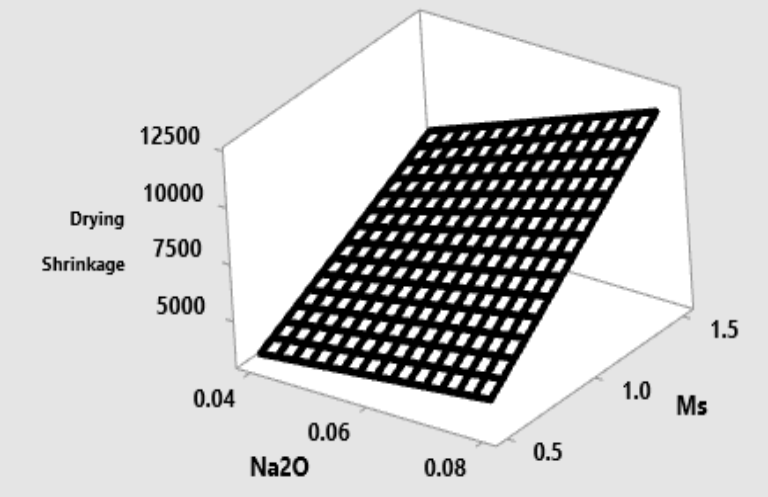


(e). Surface respond model of drying shrinkage

Fig. 4.14. Surface respond model for different properties

## 4.5 Concluding remarks

Based on the experimental results and analysis, it is possible to highlight the following:

- The activator chemistry controlled the setting time of alkali-activated slag paste, with higher significance for $Na_2O$% than that of Ms value.
- Setting time in AAS paste occurred much earlier than the beginning of the acceleration peak. Therefore, the evaluation of the solid microstructure by setting time cannot be assuredly related to heat evolution, contrary to that in OPC.
- Ms value has more effect on the cumulative heat of hydration than $Na_2O$%, whereas the changes in the heat of hydration peak values and the appearance time of the accelerated peak are profoundly more affected by Ms value.
- Generally, high early strength can be achieved with a waterglass of low silica modulus (i.e., Ms = 0.5). However, at later ages, the maximum shifted towards higher Ms.
- The amount of mass change by evaporation is not mainly responsible for the high total shrinkage of ASS. The found behavior confirmed the visco-elastic/visco-plastic response of AAS.
- The autogenous shrinkage is responsible for a significant amount of the total excessive shrinkage experienced by alkali-activated slag mortars. Moreover, increasing Ms has a more significant effect on total shrinkage than that of $Na_2O$%.
- In conclusion, by analyzing the reported results in this present study and considering the detrimental effect of each activator parameter on the shrinkage and compressive strength of AAS, it is recommended to use waterglass of moderate values of $Na_2O$% and Ms in AAS.

# Chapter 5- Interactions between shrinkage reducing admixtures and alkali-activated slag

## 5.1 Introduction

Shrinkage of AAS is significantly reduced due to the role of the shrinkage reducing admixtures. It is expected that SRA's surface activity is the main mechanism for decreasing capillary stress acting on the porous body (Pease et al., 2005).

Shrinkage reducing admixture (SRA) is commonly used to solve shrinkage problems. It belongs to the surfactant chemical family. Adding SRA reduces the pore solution's surface tension and reduces the developed internal capillary stresses due to drying (Kumarappa et al., 2018; Shoya et al., 1990). However, some negative impact for SRA was reported, such as retarding the slag's activation and extended the setting time (Kumarappa et al., 2018; Palacios and Puertas, 2007). This was attributed to the reduction in the surface tension; however, no clear explanation was provided. According to previous studies (Balogh, 1996; Rongbing and Jian, 2005; Pease and Weiss, 2005), the performance of SRA in the cement paste's pore solution was assumed similar to that in water. This had limited the SRA effect to reducing the surface tension while ignoring its effect on the pore solution's ionic compositions. However, the difference in the degree of alkalinity and chemical compositions between water and pore solution supports the idea of having variations in SRA interactions (Shoya et al., 1990). This concept was highlighted by previous findings (Feneuil et al., 2017). Hence, this study focused on providing a fundamental understanding of the SRA effects on AAS basic hydration mechanisms and the reasons behind the retardation effect, impacting the shrinkage behavior. Additionally, limited guidance is given regarding determining the appropriate concentration rate of SRA that should be used in the AAS system to attain a specific performance level.

Hence, this study aims to bridge the knowledge gap concerned with SRA interactions with AAS's pore solution. It provides a fundamental understanding of the SRA's impact on the pore solution's alkalinity and surface tension and their correlations to the low strength development

rate and autogenous shrinkage mitigation efficiency. This is anticipated to help identify the optimum SRA dosage to achieve AAS mixtures with low shrinkage.

## 1.2 Background on surfactant's behavior in aqueous solutions

The surfactant molecule is amphiphilic; consists of a polar functional group (i.e., hydrophilic head) connected to a non-polar hydrocarbon chain (i.e., hydrophobic tail) (Fig. **5.1**) (Adamson, 2001). Hence, it exhibited a high alliance to be adsorbed on the different interfaces (i.e., liquid/liquid, liquid/solid, or liquid/air surfaces). The hydrophilic head is attracted towards the oppositely charged interfaces or hydrogen-bonded solvents (such as water). The hydrophobic tail pointed toward the non-polar solvent and repelled from polar molecules [Adamson, 2001; Garnier, 2005]. SRA is a surfactant that is classified as an organic chemical. The working mechanism of SRA is directly linked to its presence at the water/air interface, thereby, the hydrophilic head is attracted to the water, and the tail is pointed toward the air (Garnier, 2005). The surface activity of SRA, to reduce the surface tension of the water/air interface, is limited by a breaking point (Pease et al., 2005). This breaking point is called critical micellization concentration (CMC), representing the saturation limit of the adsorbed surfactant molecules on a water/air interface, enabling the system to reduce its free energy (Powers, 1965). The water surface tension decreases by increasing the SRA dosage as molecules are adsorbed on interfaces until they reach the CMC. Exceeding the CMC will decrease the efficiency of SRA in reducing the water surface tension. This can be ascribed to the high amount of surfactants that remains in the bulk water. It starts to assemble, forming micelles to avoid the undesirable repulsion between the hydrophobic tail and the water (**Fig. 5.1**) (Zana, 2005). The size and the shape of the formed clusters depend on the surfactant's properties and the solvent. The simplest micelle is the spherical shape with a diameter of about 5 nm formed by the aggregation of 20-100 molecules (Zana, 2005). The formation of these aggregates and micelles is highly affected by the host liquid's nature and composition. Hence, the efficiency of SRA will differ depending on the pore solution characteristic. This emphasizes the high potential for the interaction between AAS pore solution composition and SRA efficiency.

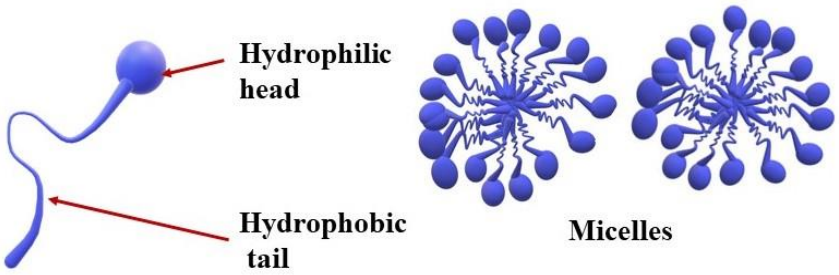


Fig. 5.1. A simple scheme of a surfactant molecule(left); the formation of micelles after the CMC (right)

## 5.1 Specific materials and Methods

Basically, the surface activity of SRA can be affected by the dissolved ions in a solution. Firstly, monitoring changes in the pore solution's surface tension for various SRA dosages, which helps in determining the suitable dosage of SRA rate. Alkali-activated slag pastes were prepared with a solution/slag ratio of 2 with various SRA dosages (i.e., high dosages up to 15 w% were selected to extend the investigated range). Moreover, the surface tension for AAS paste containing SRA was measured over hydration time, whereas, at specific hydration ages (3h, 24h, and 7 days), the pore solutions were extracted by vacuum filtration method and stored in sealed containers at a temperature of T=5°C until measurements. In a second step, to reveal the interaction between SRA and AAS pore solution, chemical analysis for the extracted AAS pore solutions, with and without SRA was performed. An Inductively Coupled Plasma Emission Spectroscopy (ICP-AES) was used to identify changes in ion concentrations (i.e., Ca, K, and Mg). The extracted solutions were diluted ten times, with 2% nitric acid solution (i.e., $HNO_3$), and stored until testing at a temperature of 5℃. Moreover, to quantify the concentrations of Si and Na, the solutions were diluted ten times with distilled water (Ye and Radlińska, 2017). Thirdly, SRA concentration in the AAS pore solution was monitored, therefore, since SRA is an organic admixture, the total organic content (TOC) of the extracted pore solution was measured to quantify the carbon content following the same procedure reported by (Eberhardt, 2011). The pH readings were carried out immediately after extracting the pore solution using a pH meter.

To reveal the impact of SRA on the phase assemblage of AAS, XRD and TGA were performed. formed C-A-S-H amount were quantified by conducting TGA at specific ages (i.e. 6h, 24h, 48h, 3, and 7 days). The nitrogen BET test was conducted on various mixtures to investigate the pore structure. In addition, the impact of SRA on the C-A-S-H nanostructure, $^{29}Si$ solid-state nuclear

magnetic resonance (NMR) on AAS pastes. Finally, characterization for AAS incorporating SRA (3%, 6%, and 9%) as shown in **Table 5.1,** was performed on AAS mortars to evaluate the autogenous shrinkage, IRH development, and the compressive strength

Table 5.1. Vicat setting times for the four AAS paste mixtures

| **Mixture number** | Control | SRA3 | SRA6 | SRA9 |
|---|---|---|---|---|
| SRA% | 0% | 3% | 6% | 9% |
| Initial set (min) | 19 | 30 | 38 | 40 |
| Final set (min) | 50 | 55 | 101 | 108 |

## 5.2 Results and Discussions:

### 5.2.1 SRA and surface tension reduction

Surface tension is defined as the required energy/unit area to expand the liquid's surface (Ferrari and Wittmann, 1987). According to the Kelvin-Laplace equation, the capillary pressure is highly dependent on the surface tension of the liquid (Y and Radlińska, 2016). Nevertheless, AAS pore solutions consist of different valence ions and are classified as strong electrolytes (Puertas, 2004). For this aqueous electrolyte solution, it was reported that the surface tension increases with increasing cations concentration; hence, some ions will have higher effects (Bostrom et al., 2001). **Figure 5.2** shows the changes in the surface tensions for AAS pore solutions extracted from specimens cured under a sealed condition for various SRA contents. The initial surface tension value for the AAS pore solution without SRA addition was 53 mN/m. The surface tension decreased steeply as the SRA dosage increased until reaching a plateau at about 33 mN/m. The CMC can be deduced from **Fig. 5.2** as the intersection of two straight lines. The two lines represent the surfactant effect before and after the CMC. Hence, the CMC for the tested AAS pore fluid is slightly above 9% of SRA. As mentioned earlier, CMC is conceptually related to the self-aggregation phenomenon. Reaching the CMC corresponds to the maximum possible surfactant enrichment at the liquid/vapour interface. In other words, the adsorption isotherms flatten out, and the bulk activity of the non-ionic surfactant depleted significantly (Garnier, 2005; Wattebled, 2006; Schulz, 2004). It can be concluded that adding SRA at a dosage less than 9 wt% will have a higher impact on reducing the surface tension of ASS pore solution leading to

lower shrinkage. However, exceeding the 9% SRA will have a minimal effect. Hence, 9% SRA was selected in this study as the upper limit for the following experimental phases.

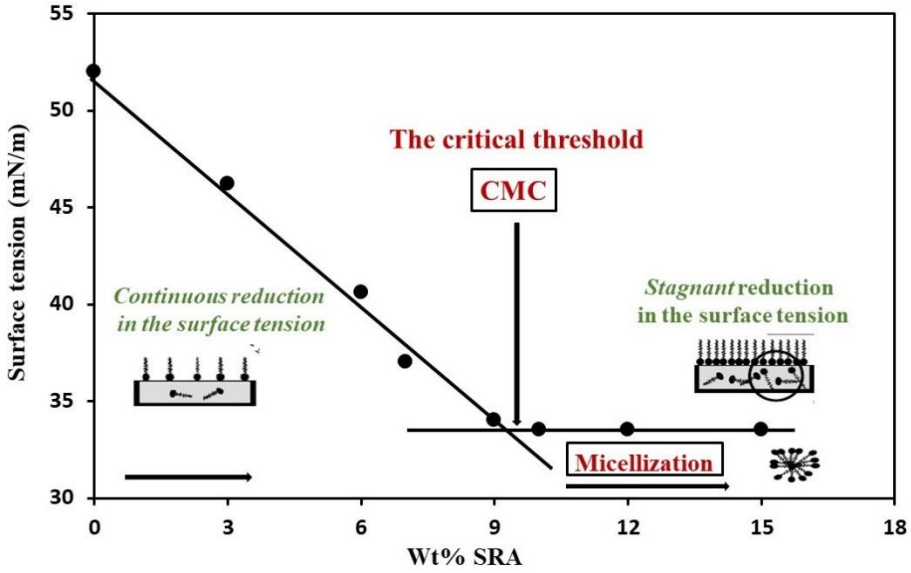


Fig. 5.2.The surface tension of emulsions of SRA in the extracted pore solution of AAS paste.

On the other hand, control AAS paste (without SRA) showed an increase in the extracted pore solution surface tension with hydration time which agrees with a previous study (Kumarappa et al., 2018). Conversely, the AAS pore solution's surface tension slightly decreased throughout the reaction process for mixtures incorporating SRA (**Fig. 5.3**). The progress of hydration will consume water; hence, SRA concentration increases in pore solution (Eberhardt, 2011). This was confirmed by evaluating the time-dependent concentration of SRA in the AAS pore solution using the TOC test. An increasing trend in SRA concentration in the pore fluid over the investigation period was reported **(Table 5.2)**.

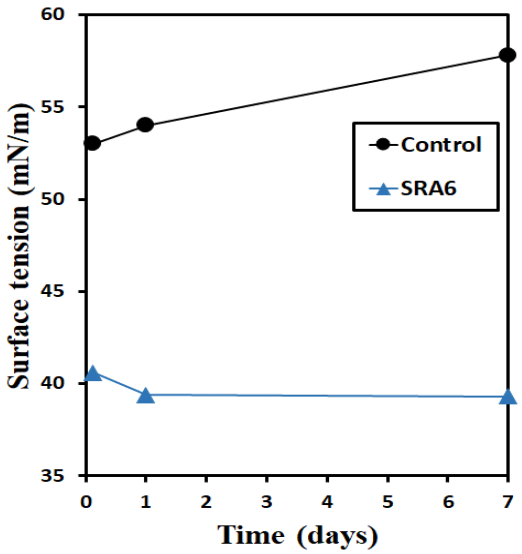


Fig. 5.3. The time-dependent surface tension of extracted pore solution of AAS pastes for control and SRA6 mixtures

Table 5.2. The total organic content of extracted AAS pore solutions

| AAS hydration time | Carbon content (mg/l) |
|---|---|
| 1h | 13295 |
| 3h | 12853 |
| 24h | 16500 |
| 3 days | 21683 |

### 5.2.2 Influence of SRA on the hydration kinetics of AAS paste

**Figure 5.4** shows the heat released by AAS mixtures, which followed a similar trend to OPC hydration (i.e., having five hydration stages) (Ravikumar, N. Neithalath, 2012; Ben Haha et al., 2012). The incorporation of SRA had changed the reaction kinetics for AAS. The time to reach the peak (TRRP) for the control mixture without SRA was 11.3h while increasing SRA dosage extended the TRRP to 30h, 36.5h, and 39h for SRA3, SRA6, and SRA9 mixtures, respectively.

The relative degree of hydration (rel. $\alpha_{hyd}$ (t)) for each mixture is shown in **Table 5.3.** AAS pastes incorporating SRA exhibited a relative degree of hydration less than 1 at age 3 days, indicating retardation for the hydration reaction. Hence, this reduction in the hydration degree can be attributed to the interaction effect between SRA with the pore solution. Finally, as shown in **Fig. 5.4,** the control paste's calorimetric signals indicated an intense alkali activation of slag

during the first 24h, leading to massive precipitation of reaction products (Ravikumar, N. Neithalath, 2012). In the presence of SRA, mass precipitation of reaction products continued over a longer period. Nonetheless, after 7 days, all the mixtures incorporated with SRA showed approximately the same rel.$\alpha_{hyd}$ compared to the control mixture. In conclusion, this retardation is due to the SRA interactions with the pore solution of AAS paste and the changes in ionic species, as will be discussed in the following section.

Table 5.3 Relative degrees of hydration of pastes containing SRA

| Mixtures | rel.$\alpha_{hyd}$ | |
|---|---|---|
| | 3 days | 7 days |
| Control | 1.0 | 1.00 |
| SRA3 | 0.973 | 1.03 |
| SRA6 | 0.92 | 1.03 |
| SRA9 | 0.824 | 0.99 |

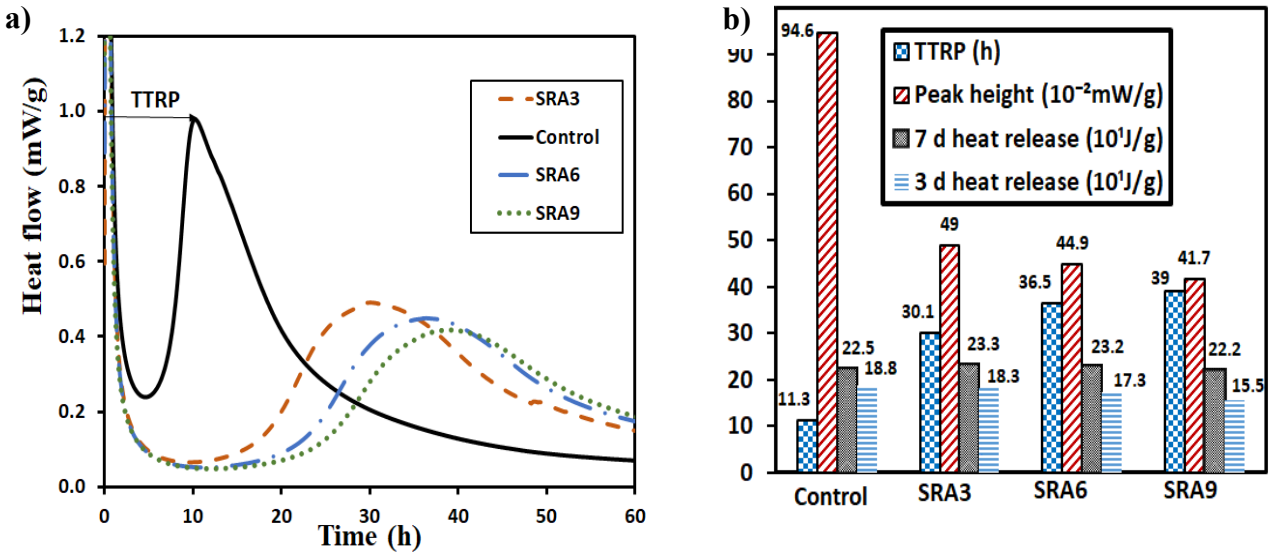


Fig. 5.4. (a) Heat evolution for AAS pastes with different SRA dosages using isothermal conduction calorimetry; (b) summarized results

### 5.2.3 SRA impact on Ionic content of AAS pore solutions

Pore solutions were extracted from mixtures with and without SRA to compare the changes in the chemical composition. During the initial stage of the activation process, the high pH activator breaks the Ca-O, Al-O, and Si-O bonds on the slag surface (Puertas et al., 2004; Shi and Day, 1995). The dissolved species in the solution from the slag particles will be in the form of calcium

($Ca^{2+}$), $[H_2SiO_4]^{2-}$, $[H_3SiO_4]^-$ and $[H_4AlO_4]^-$ (Shi and Day, 1995). Moreover, the waterglass activator ($SiO_2$_$nNa_2O$_$mH_2O$+ NaOH) will contribute significantly to the Si and Na ions concentrations in AAS pore solutions. These compounds' precipitation will generate the AAS's microstructure as their concentrations reach the solubility limit for different phases and solid compounds (Puertas et al., 2004; Shi, 1997). Hence, the evolution of such dissolved ions in the pore fluid with time could reveal information about the reaction process and product formation (Fernandez-Jimenez and Puertas, 2001). **Figure 5.5** shows the concentrations of five major ions (Na, K, Ca, Si, and Mg), as a function of the specimen's age. Initially, after 3h of the hydration, the Si concentration was very high then at 24h of hydration, it was depleted significantly by around 60% (**Fig. 5.5a**). This initial reduction in the Si concentration revealed massive precipitation of reaction products associated with the slag activation in the control mixture. On the other hand, the Si concentration in the pore solution for the SRA mixture exhibited a different trend, decreasing gradually with time, indicating that the activation process is slower **(Fig. 5.5b)**. These results agreed with the previous conduction calorimetric results, showing that SRA mixtures had less intense acceleration peaks over a longer time. Further, as the reaction progress, the Na concentration decreased gradually, which could be ascribed to the precipitation of initial hydration products (i.e., C-A-S-H) (Shi and Day, 1997; Fernandez-Jimenez, F. Puertas).

One interesting point, the addition of SRA had significantly reduced the Ca, Mg, and K ions. Lowering the alkali ions in the pore solution significantly slowed the slag hydration and dissolution, yielding a lower formation of reaction products (Mobasher et al., 2016).

The activated solution's pH plays the primary role in the slag's initial dissolution, favoring Ca ions' dissolution from the slag particle surface to the solution (Puertas et al., 2004; Shi, 1997). The pH values of pore solutions reveal that the presence of SRA reduced the pore solution's alkalinity by lowering Ca concentration (**Table 5.4**). Calcium ions were depleted by about 60% for SRA mixtures (F**ig. 5.5a, b**). After 24 h, pore solutions for mixtures incorporating SRA showed a significant depletion in the amount of Mg and K compared to that of control AAS. One hypothesis is that the addition of SRA affected the solubility limit of alkalis to ionize in the pore solution (Rajabipour et al., 2008). In other words, a delay in the slag grain dissolution in mixtures containing SRA is partially responsible for the ion's depletion. Hence, there is a strong

interaction between SRA and pore solution, which dominates the hydration retardation experienced by AAS incorporating SRA.

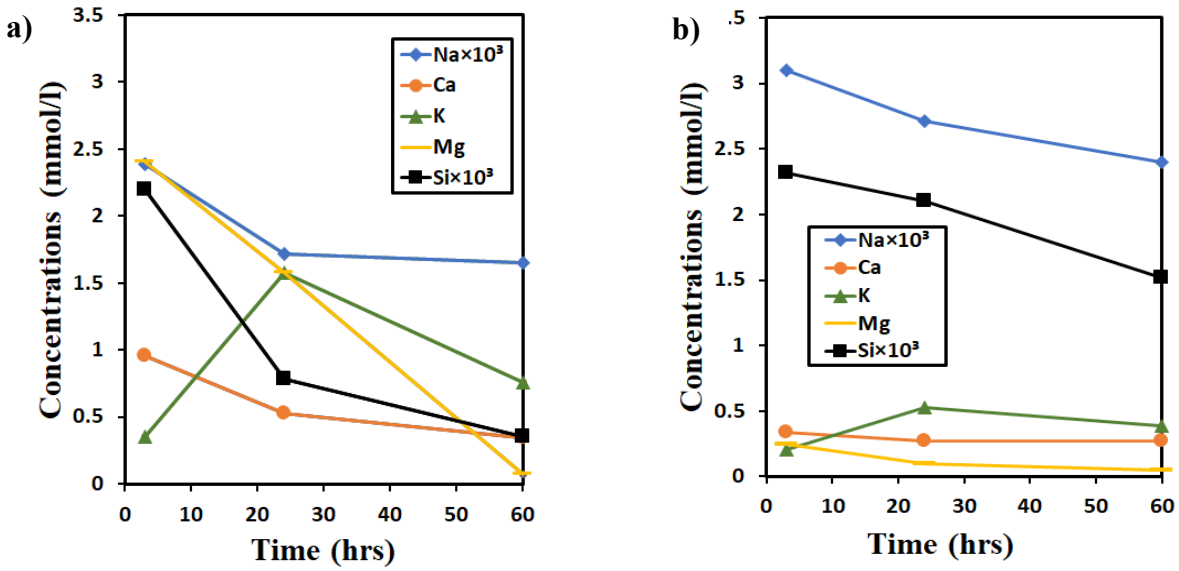


Fig. 5.5. Chemical analyses of AAS pore solutions extracted (a) Control; (b) contain 6% SRA

Table 5.4. pH transformation of the extracted AAS pore solution in the presence of 6% SRA

| Hydration time | pH value | |
|---|---|---|
| | Control | SRA6 |
| 3 hrs | 13.89 | 13.78 |
| 24 hrs | 13.97 | 13.82 |
| 7 days | 13.91 | 13.73 |

### 5.2.4 Autogenous shrinkage

**Figure 5.6** shows the effect of SRA addition on autogenous shrinkage for AAS mortars. Autogenous shrinkage values were -3801με, -2397με, and -1837με for SRA3, SRA6 and SRA9, respectively, compared to -4290 με for the control mixture without SRA. Hence, increasing SRA concentration resulted in a lower autogenous shrinkage. The majority of the developed autogenous shrinkage for AAS takes place during the first 7 days. The 7 days autogenous shrinkage for control, SRA3, SRA6, and SRA9, represented around 60% to 70% of the total measured shrinkage at the end of the investigating period (i.e., 70 days). Mixtures with 9% SRA

showed the highest decrement in autogenous shrinkage rate, which agreed with the main reaction process discussed in **Fig. 5.4**. After the initial reaction period, the rate of autogenous shrinkage reduced significantly. Moreover, as shown in **Fig. 5.6b,** the maximum autogenous shrinkage rate coincided with the beginning of the acceleration period of the hydration (i.e., chemical shrinkage and self-desiccation). This indicated the significant influence of AAS hydration kinetics on autogenous shrinkage during the early stages.

Consequently, the autogenous shrinkage is significantly decreased by around 16%, 48%, and 62% for SRA3, SRA6 and SRA9, respectively. The lower intensity of autogenous shrinkage for mixtures SRA3, SRA6, and SRA9, can be attributed to the low capillary tension resulting from self-desiccation.

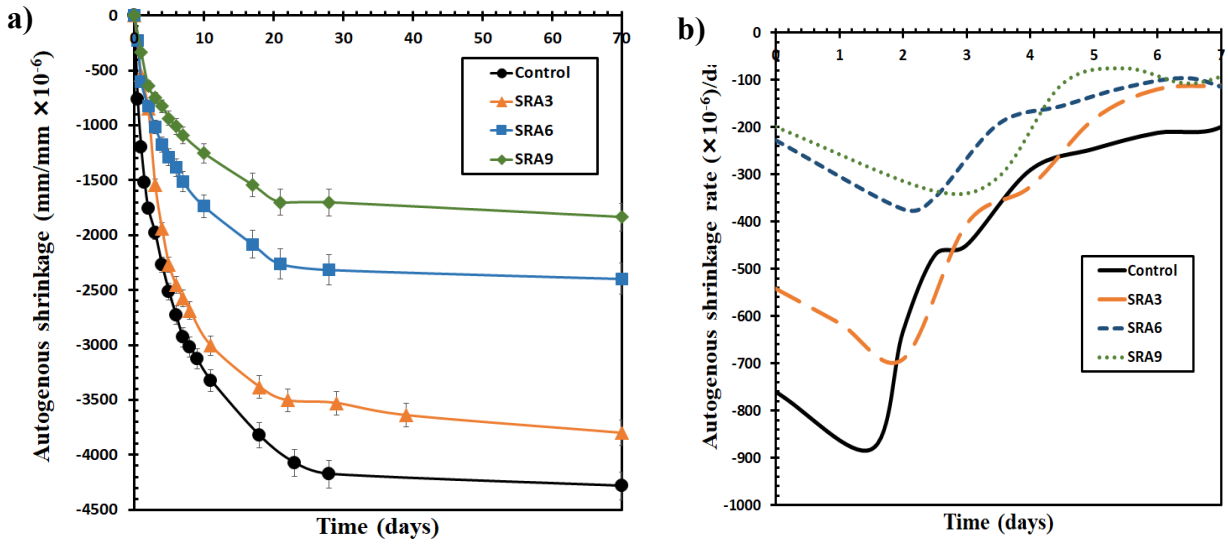


Fig. 5.6. (a) Autogenous shrinkage of AAS mortars of different dosages of SRA; (b) Corresponding autogenous shrinkage rates.

### 5.2.5 Reaction products characterization

#### 5.2.5.1 Thermogravimetric (TGA) analysis

**Figure 5.7a** represents the thermogravimetric analysis of AAS at the age of 7 days. The main peak taking place between 30℃ to 220℃ is correlated to the amount of formed C-S-H and aluminates in waterglass AAS ($\Delta m_1$) (Neto et al., 2008). Another endothermic peak occurred at a temperature range of (275℃-425℃) which is correlated to hydrotalcite (Ht) phases. Hydrotalcite

is a crystal phase ($Mg_6Al_2$. $CO_3(OH)_{16}\times 4H_2O$) that has a layered structure with interlayer water molecules and ($CO_3^{-2}$) ion (Wang and scrivener, 1995). This peak corresponding to the release of structural water and $CO_2$ constituent the Ht-phases (Abdalqader et al., 2016) is assigned as ($\Delta m_2$). **Figure 5.7b** shows the estimated C-A-S-H amount as a function of hydration time and the SRA dosages. The amount of formed C-A-S-H in AAS mixtures had reduced significantly as SRA dosage increased, especially during the first 24 h. For instance, the weight loss associated with C-A-S-H at the age of 6 hrs increased from 4.6% to 6% as the SRA dosage increased from 3% to 6%, which agrees with the heat of hydration results (**Fig. 5.4**). This also confirms the role of high SRA dosage on depressing alkalis dissolution and reduces the cations/anions concentrations in the pore solution yielding a lower amount of C-A-S-H formation (**Fig. 5.5b**). Consequently, it can be stated that a high dosage of SRA reduced the C-A-S-H formation. However, the development rate of the amount of formed C-A-S-H in SRA mixtures (**Fig. 5.7b**) is consistent with the autogenous shrinkage rate development **(Fig. 5.6b),** indicating that the reaction kinetics is the dominant parameter affecting the autogenous shrinkage.

**Table 5.5** depicts the calculated mass loss of reaction products based on **Fig. 5.7a**. $\Delta m_1(\%)$ decreases as the SRA dosage increase, while Δm2 increases as the SRA dosage increases. For instance, the addition of 9% SRA decreased the $\Delta m_1(\%)$by approximately 8%, while it increased by around 22% compared to the control mixture without SRA. This indicates that AAS paste with a higher SRA dosage contains a large volume of hydrotalcite-like phases compared with the control one. This also is confirmed by XRD results, as will be shown later.

Besides, the mass of reaction products for AAS mixtures is approximately the same at the age of 7 days, but the difference is in the products' amount. This is in good agreement with the measured relative degree of hydration (see **Table 5.3**)

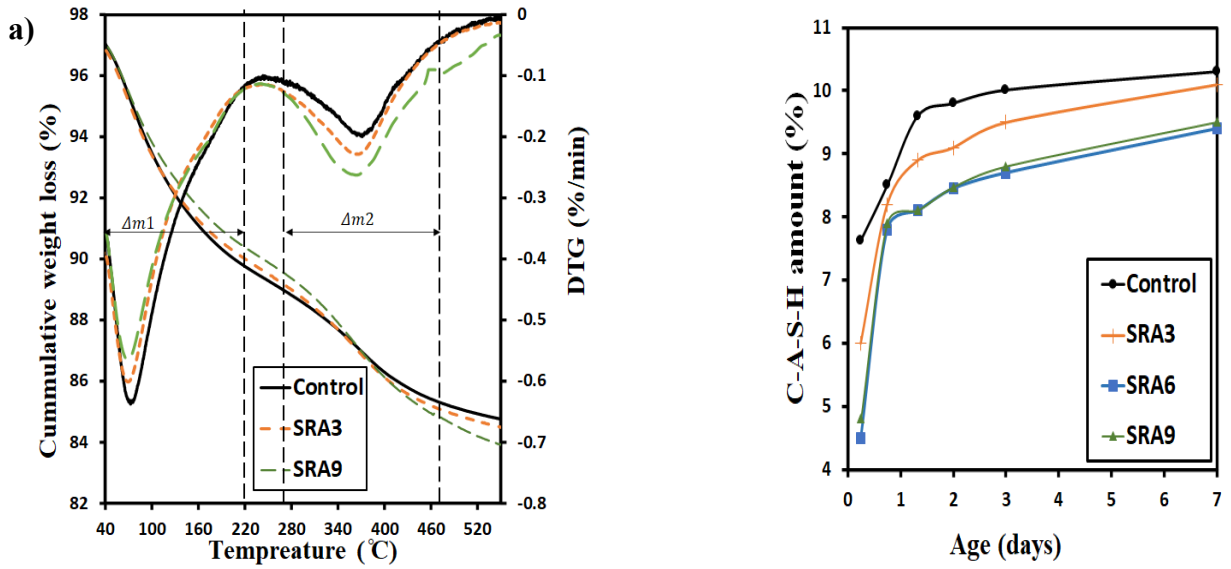


Fig. 5.7. (a) TGA curves of AAS pastes hydrated for 7 days; (b). Influence of SRA dosage on C-A-S-H amount.

Table 5.5. Mass loss of C-A-S-H gel and hydrotalcite-like phases

| Mixture | $\Delta m_1(\%)$ | $\Delta m_2(\%)$ | $\Delta m_1 + \Delta m_2(\%)$ |
|---|---|---|---|
| Control | 10.3% | 3.04 | 13.34 |
| SRA3 | 10% | 3.4 | 13.4 |
| SRA9 | 9.56% | 3.85 | 13.41 |

5.2.5.2 Nuclear magnetic resonance spectroscopy ($^{29}$Si NMR spectra)

**Figure 5.8** illustrates the deconvoluted $^{29}$Si NMR spectra of control, SRA3, and SRA9 AAS paste mixtures. Chemical shifts are usually explained in terms of various silicon $Q^n$ for each tetrahedral unit (i.e., Q is $SiO_4$), n indicates the number of connected bridging oxygen to other atoms of Si. In the AAS slag, the C-A-S-H mainly contains $Q^1$, $Q^2$, and $Q^2(1Al)$, which indicates that Al is incorporated into the C-A-S-H silicate chain (Renaudin et al., 2009; Richardson et al.,1993). According to the literature, the $Q^1$ unit refers to a peak appearing between -73 and -78 ppm, while $Q^2$ refers to the peak appearing between -83 and -85 ppm. The substitution of Si by Al is assigned to $Q^2(1Al)$, resulting in a chemical shift of 3 or 5 ppm towards more positive values, so the peak appears around -81 ppm (Ismail et al., 2013). All these values reflect the formation of the main reaction product of the AAS, which is a C-S-H with Al tetrahedrally incorporated in the structure. Based on published work [ Richardson and Groves, 1997; Skibsted

and Andersen, 1997] the mean chain length (MCL), which indicates the polymerization of the calcium silicate hydrate, and Al/Si ratio in the C-A-S-H, which reflects the substitution of Si by Al in tetrahedral positions, can be determined according to the following equations Eqs: (5.1-5.2):

$$\mathrm{MCL} = \frac{2(\mathrm{Q^1} + \mathrm{Q^2} + 1.5\mathrm{Q^2(1Al)})}{\mathrm{Q^1}} \quad 5.1$$

$$\mathrm{Al/Si} = \frac{0.5\mathrm{Q^2(1Al)}}{\mathrm{Q^1} + \mathrm{Q^2} + \mathrm{Q^2(1Al)}} \quad 5.2$$

As shown in **Fig. 5.8**, the presence of SRA did not significantly change the nature of the layered structure in C-A-S-H. Nonetheless, SRA considerably modified the percentage of bridging tetrahedral Si units. **Table 5.6** summarized some important values revealed from the $^{29}$Si MAS NMR test. The $\sum Q^2/Q^1$ ratio, roughly reflecting the degree of polymerization of the silicate (Thomas and Jennings, 2006), had changed with the addition of SRA. Increasing SRA dosage slightly decreased the $Q^2$ units while increased $Q^1$ leading to a lower $\sum Q^2/Q^1$ ratio. Hence, the presence of SRA had decreased C-A-S-H gel polymerization.

The addition of SRA had reduced the $Q^2(1Al)$ units revealing that the Si substitution by Al in the tetrahedral silicate chain is slightly lower than that of the control AAS paste (**Fig. 5.9**). However, this may be detected from the decrement in the Al/Si ratio. Si substitution by Al at tetrahedral positions in the silicate chains had already been demonstrated by several authors (Richardson et al., 1994; Richardson and Cabrera, 2000).

The $\sum Q^2/Q^1$ ratio for the control paste was higher than those of calcium silicate hydrate formed in AAS paste containing SRA (**Table 5.6**). This indicated that the formation of solid species with shorter length tetrahedral silicate chains (MCL).

Consequently, the C-A-S-H composition for the SRA mixtures is less protonated than the control one and had a shorter chain length. This result confirmed the reduction of silicate polymerization degree in the presence of SRA. The lower polymerization degree of C-A-S-H gels of SRA mixtures, indicating that the Si chains in SRA mixtures experience less intense C-A-S-H syneresis (i.e., contraction of silicate gel's structure) during the polymerization process, which

subsequently decreases the autogenous shrinkage (Chen et al., 2021, Ye and Radlińska, 2017, Abdalqader et al., 2016).

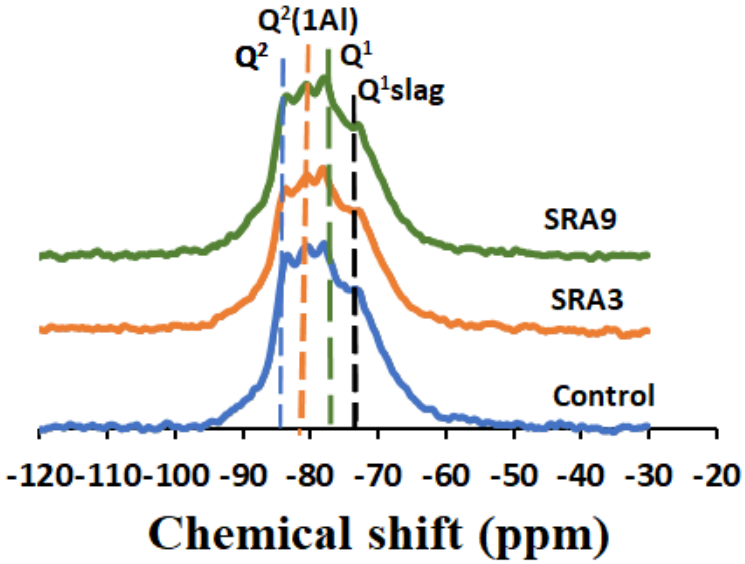


Fig. 5.8. $^{29}$Si solid-state NMR patterns of AAS paste with 3% and 9% SRA

Table 5.6. Parameters obtained with $^{29}$Si MAS NMR (Figs. 5.8, 5.9)

| Mixture | Admixture | $\alpha = (1-(Q^0+Q_{slag}) \times 100\%$ | $\sum Q^2/Q^1$ | MCL | Al/Si |
|---|---|---|---|---|---|
| Control | 0% | 68.94 | 1.99 | 6.87 | 0.151 |
| SRA3 | 3% | 69.23 | 1.80 | 6.44 | 0.1487 |
| SRA9 | 9% | 67.9 | 1.79 | 6.41 | 0.1477 |

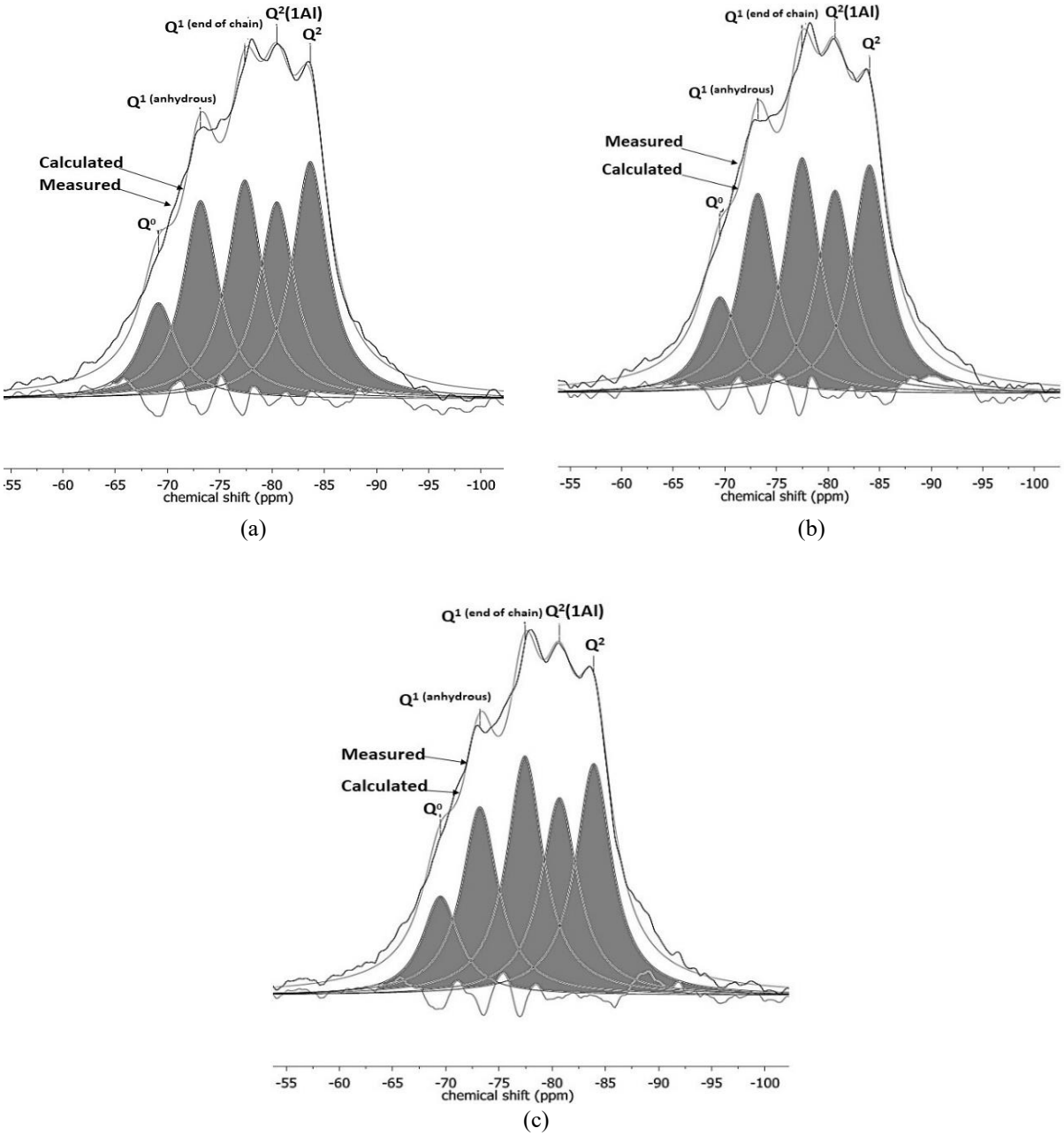


Fig. 5.9. Deconvolution of $^{29}$Si solid-state NMR patterns of AAS containing(a) 0% SRA (b) 3% SRA; (c) 9% SRA.

### 5.2.5.3 XRD analysis

Mineralogical characterizations of AAS reaction products were investigated using XRD. As shown in **Fig. 5.10**, the main detected hydration products were C- S-H (l), hydrotalcite-type phases, and portlandite for mixtures with and without SRA (Ye and Radlinska, 2016). The detected calcite can be attributed to the interaction between $CO_2$ and dissolved $Ca^{2+}$ from the slag during sample preparation or testing (Ye and Radlinska, 2016). It can be concluded that there are two main hydration products. The first is a poorly crystalline C-A-S-H with a riversideite structure associated with a peak near 2θ = 29.5°. Additionally, other phases of C-A-S-H were detected around 32.1° and 50.1° (Ye and Radlińska, 2017). The second product is hydrotalcite ($Mg_6Al_2(CO_3)(OH)_{16}.4(H_2O)$), which is a very stable product, detected at 2θ around 11.6°, 23.4° and 34.8° (Abdalqader et al., 2016).

Generally, the mixtures with and without SRA showed approximately similar diffractograms (i.e., same hydration products). Adding SRA led to higher precipitation of hydrotalcite (Ht)-phases (i.e., which is crystalline). The greater the SRA dosage, the higher the detected Ht-phase peaks (**Fig. 5.10**). The high formation for Ht-phases consumed Al and Mg ions. This explains the source of the significant decline of Al and Mg ions in the pore fluid extracted from the SRA mixtures (**Fig. 5.5b**). Furthermore, the NMR spectra showed a drop in the proportion of $Q^2$ (1Al) for SRA mixtures, revealing that a higher portion of Al precipitated in the form of Ht- phases in the presence of SRA. This suggested that the majority of reaction products in AAS mixtures with higher SRA dosage are crystalline. These crystalline products led to a more stable and orderly rearranged microstructure, which resists deformation and consequently lowering the autogenous shrinkage (Ye and Radlińska, 2017).

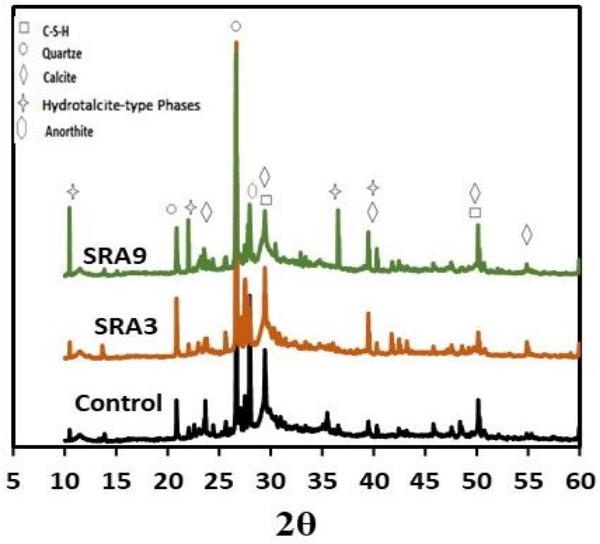


Fig. 5.10. XRD patterns of AAS containing control; 3% SRA and 9% SRA

### 5.2.6 Pore structure characterization

According to Mindes et al. 1981, pores that existed in cementitious materials can be classified into gel pores with diameter d < 10 nm, directly proportional to the hydration degree, and capillary pores with diameter d > 10nm. **Figure 5.11a** represents the adsorption/desorption and the pore volume for the control mixture and mixtures with 3% and 9% SRA at various relative pressures ($p/p_o$). All the tested samples exhibited type V classification according to the International Union of Pure and Applied Chemistry system (IUPAC). This indicated that AAS has a hysteresis loop with an inflection point at relatively high pressure and contains micropores (<2 nm), mesopores (2.5–50 nm), and macrospores (>50 nm) (Ye and Radlińska, 2017, Joyner et al., 1951).

The addition of SRA had modified the pore structure for AAS as indicated by the measured isotherms curves (**Fig. 5.11a**). The control mixture (without SRA) adsorbed a significantly higher amount of the adsorbents at relative pressure above 0.38 compared to mixtures incorporating SRA (i.e., SRA3 and SRA9). This implied a higher amount of fine pores in the control mixture.

Further analysis of the adsorption branch isotherms was performed by Barrett-Joyner-Halends (BJH) method to achieve the pore size distribution (Barrett et al., 1951). The adsorption branch was used to avoid the pore blocking effects (i.e., inkbottle effects) that may lead to uncertain results (Ranaivomanana et al., 2011; Joyner et al., 1951). The cumulative pore volumes of AAS mixtures are illustrated in **Fig. 5.11b.** The results reveal that mesopores volume accounts for 90-95% of the total pore volume for all tested AAS mixtures, which agreed with previous studies (Neto et al., 2008; Brough and Atkinson, 2002; Shi, 1996). The incorporation of SRA leads to a reduction in the volume of gel pores, which are the pores existing in C-A-S-H gel (Ismail et al., 2013). Compared with the control AAS paste, the C-A-S-H gel porosity (0.5-10 nm) of SRA3 and SRA9 are noticeably lower. Moreover, SRA9 exhibited the lowest volume of gel pores, while in the control mixture was the highest **(Fig. 5.11c)**. This can be attributed to the reduction in the amount of C-A-S-H formation, as evidenced by the TGA analysis. Consequently, adding SRA resulted in lower gel porosity within the range of <10nm, and the reduction is more pronounced by increasing SRA dosage, as shown in **Fig. 5.11c.**

Moreover, the volume fraction of mesopores within a range of 2.5–50 nm is considered an important factor influencing the autogenous shrinkage of AAS. It affects the capillary stresses (i.e., the driving force for autogenous shrinkage) during the self-desiccation process (Neto et al., 2008). Based on the cumulative pore volume, the volume fraction of mesopores can be estimated in this study (Chen et al., 2021). As indicated in **Fig. 5.11b**, all AAS mixtures exhibited approximately the same volume fraction of mesopores, around 95%. Therefore, the results indicate that SRA influences the pore structure of AAS pastes mainly by reducing the gel porosity which is directly linked to the C-A-S-H formation rather than modifying the capillary pore structure.

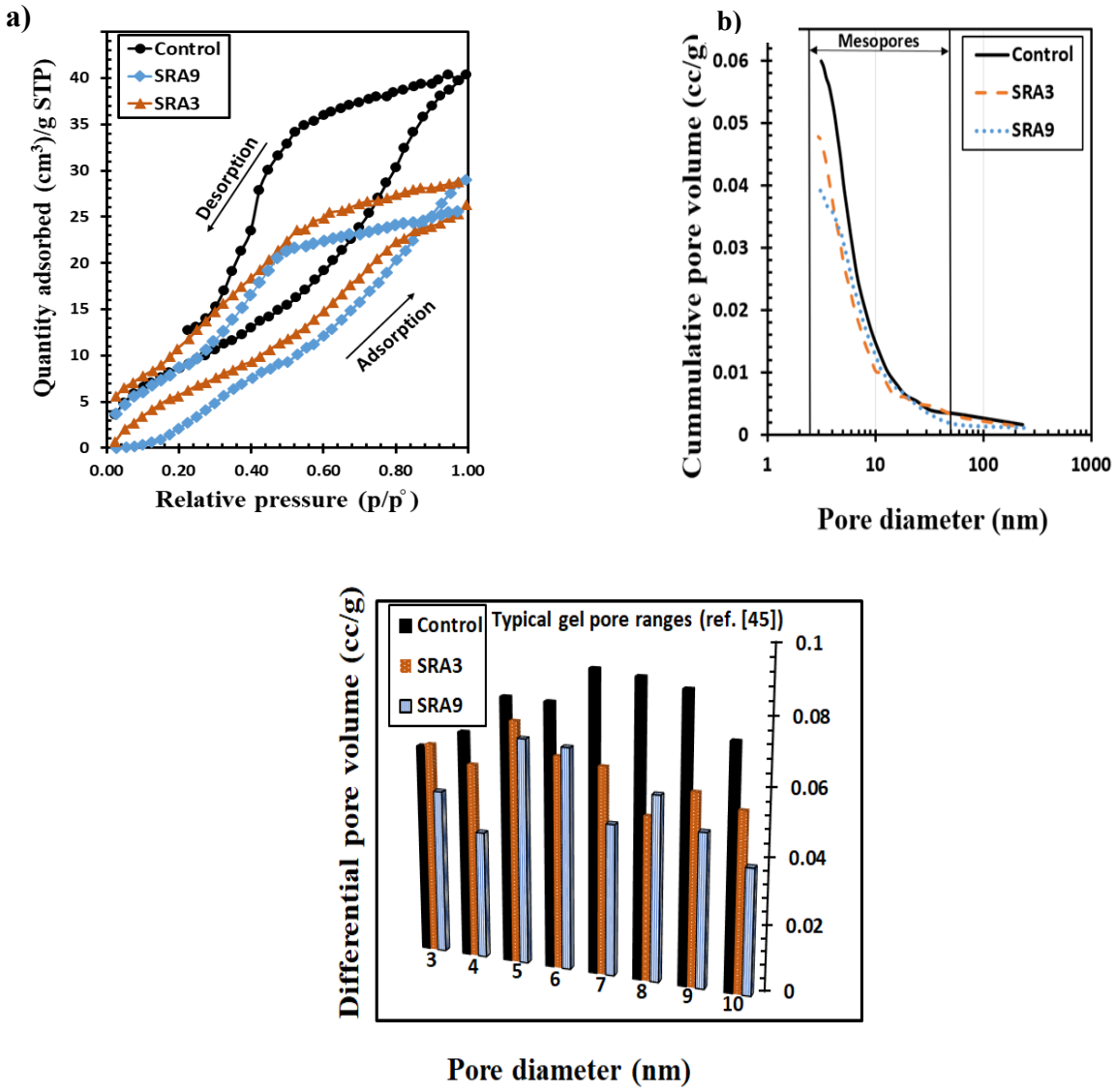


Fig. 5.11. (a) Nitrogen sorption isotherms curves for mixtures with the various dosage of SRA; (b) Cumulative pore volume; (c) Gel pore distributions

### 5.2.7 Internal relative humidity

**Figure 5.12** illustrates the changes in the internal relative humidity (IRH) for mixtures with and without SRA over the investigated period. Two-stage of IRH development can be recognized. Stage 1 reflects the moisture saturated stage (i.e., IRH remains around 100%). The chemical shrinkage is the main driving force behind the measured macroscopic deformation (Chen et al., 2021). At the end of this stage, the IRH started to decrease due to increased hydration rate (i.e., more chemical shrinkage and self- desiccation) (Chen et al., 2021; Han et al., 2014, Wyrzykowski and Lura, 2016). This critical time represents the end of the first stage and the start

of the second stage, during which the IRH sharply dropped and then decreased at a lower rate afterward. The drop in IRH for the control mixture was steeper than mixtures incorporating SRA. This can be attributed to the high chemical shrinkage for the control mixture compared to SRA mixtures, as confirmed by TGA results. The addition of SRA was found to delay the critical time due to the slower water consumption in the hydration process than control mixtures without SRA.

This agreed with the detected higher initial formation of C-A-S-H in mixtures without SRA (**Fig. 5.7b**). Generally, during the first 7 days, there is a dramatic reduction in IRH for AAS mixtures, which agrees very well with their autogenous shrinkage development. This further confirms that IRH is an essential factor driving affecting autogenous shrinkage.

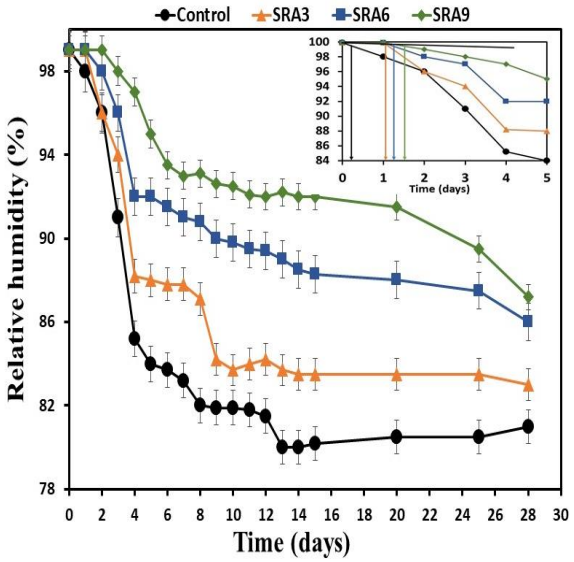


Fig. 5.12. Development of internal relative humidity in AAS mixtures with different SRA

### 5.2.8 Influence of SRA on strength development

**Figure 5.13** presents the compressive strength for mixtures with and without SRA. Regardless of the added dosage, SRA had significantly impacted the early age strength (i.e., 3 days strength). This can be ascribed to the lower relative degree of hydration for mixtures incorporating SRA (**Table 5.3).** At later ages (i.e., > 3days), all mixtures incorporating SRA exhibited lower strength development, except SRA3, which showed a slight improvement. For instance, mixtures with 9% SRA showed around 40% reduction in the compressive strength at the age of 3 days compared to the control mixture without SRA. Nonetheless, this reduction decreased to around 16% at the age

of 7 days. Moreover, these findings agreed with the reported pore solutions analysis (**Fig. 5.5**). Higher soluble concentrations of cations/anions in the pore solution can significantly accelerate slag hydration and strength development (Kumarappa et al., 2018). Consequently, the high incorporation dosage of SRA (> 3%) considerably depresses the formation of C-A-S-H, as evidenced in (**Fig. 5.7b**).

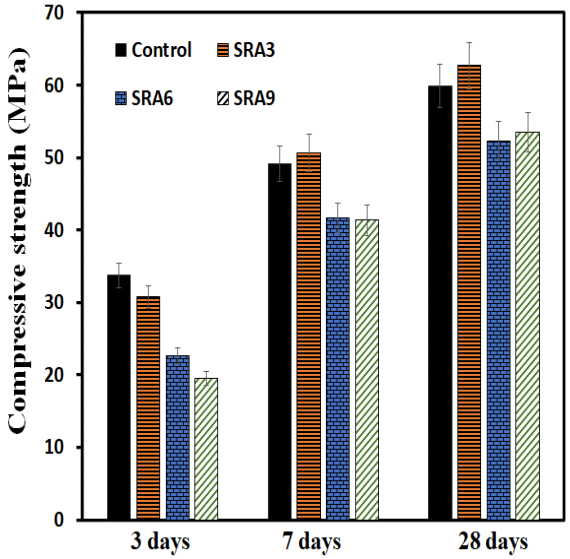


Fig. 5.13. Compressive strength of the mixtures at different ages

### 5.2.9 SEM (EDX) analysis

The microscopical analysis was carried out on AAS pastes with and without SRA. **Figure 5.14** shows the BSE-SEM of the hydration products at age of 7 days for Control and SRA9 mixtures.

As can be seen, discrete crystals of hydrotalcite-type phases can't be distinguished on a sub-micrometer scale by SEM images. Whereas these tiny crystals are finely intermixed with the C-A-S-H (Wang and Scrivener, 2003).

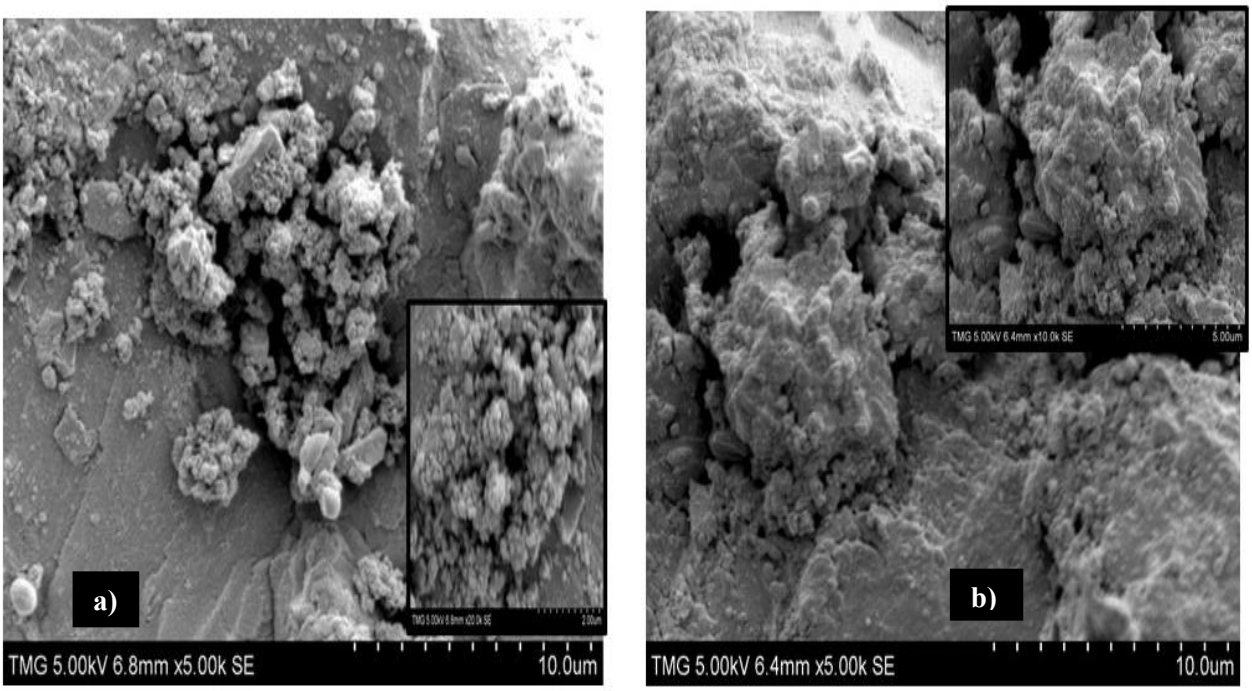


Fig. 5.14. Microstructure after 7 days for AAS (a) Control; (b) With SRA

EDS X-ray microanalysis was performed to identify the influence of SRA addition on the major hydration product of AAS. **Table 5.7**. Shows the main elemental ratio of these reaction products as derived from the analysis of different EDX points.

Table 5.7 Average atomic ratios of 6 points observed in the hydration products by EDX-analyses

| Sample | Ca/Si | Al/Si | Mg/Ca | Mg/Si |
|---|---|---|---|---|
| Control | 1.1 | 0.257 | 0.177 | 0.197 |
| SRA9 | 1.14 | 0.23 | 0.26 | 0.297 |

The Ca/Si ratio for the Control and SRA9 AAS mixtures is 1.1 and 1.14 respectively. This confirms the formation of C-A-S-H with low C/S ratio in waterglass AAS system (Brough & Atkinson, 2002; Puertas, Fernández-Jiménez, et al., 2004; Wang & Scrivener, 2003). However, the mixture with SRA exhibited a higher ratio in Ca/Si, which indicates that the SRA mixture is less protonated compared to the control one. This microanalysis result confirms the NMR

observations, whereas the addition of shrinkage reducing admixture reduced the amount of $Q^2$ units and thus, lower silicates MCL.

Furthermore, the SRA9 mixture is richer in magnesium as the Mg/Si and Mg/Ca (0.297,0.26) ratios are higher compared to the control mixture (0.197, 0.177). This suggests the higher formation of hydrotalcite-type is in AAS with SRA. These findings are consistent with the data from XRD and TGA.

The Al/Si ratio by EDX for the AAS with SRA was found to be lower (i.e.,0.23) compared to that in AAS without SRA (i.e., 0.257). These ratios are consistent with that found in Wang and Scrivener's study (Wang and scrivener, 2003). However, the NMR results confirmed the substitution of Al for Si in the bridging sites, leading to a charge imbalance which is compensated by alkali incorporation in the C-A-S-H (Brough & Atkinson, 2002; Puertas, Fernández-Jiménez, et al., 2004; Wang & Scrivener, 2003). The calculated Al/Si ration from NMR for the Control and SRA9 AAS mixtures were 0.151 and 0.147 respectively. Indicating SRA9 mixtures contain less aluminum in the C-A-S-H than those corresponding to the Control.

### 5.2.10 Mechanisms of SRA in mitigating autogenous shrinkage of AAS

The previous results show that SRA dosage significantly affected the microstructure development, porosity, and hydration kinetics, which are highly linked to shrinkage behavior. Autogenous shrinkage takes place under sealed conditions, whereas the water exchange is prevented (Neto et al., 2008). Generally, chemical shrinkage occurs, during the early hydration period, leading to a volume reduction in the reacting system (Chen and Brouwers, 2007). After the setting, water/air menisci will form in capillary pores generating capillary stresses, which is the driving force for autogenous shrinkage (Neto et al., 2008). Moreover, the finer pore size for the AAS system, compared to the OPC system, increased capillary stresses and consequently autogenous shrinkage (Neto et al., 2008). According to Laplace Eq. (2.1), the capillary stresses ($\sigma_{cap}$) will directly be proportional to the surface tension ($\gamma$) and inversely with the pore size (r).

Hence, mixtures incorporating SRA exhibited lower autogenous shrinkage than control mixtures without SRA due to reducing the pore solution's surface tension. This had led to around 62% reduction in the autogenous shrinkage compared to the control mixture at the CMC SRA (i.e. 9%). Moreover, increasing SRA was found to increase the crystallinity of AAS reaction products, which enhanced the AAS matrix's stability that can compensate for the shrinkage.

On the other hand, studies have proved that the viscous performance of AAS can contribute to autogenous shrinkage (Chen et al., 2021; Li et al., 2019, Li et al., 2020). Therefore, in addition to the self-desiccation, the syneresis of C-A-S-H gels (i.e., volumetric contraction of silicate gel during the polymerization) is also adopted to explain the high autogenous shrinkage of AAS. The NMR results showed a lower polymerization degree for C-A-S-H for mixtures incorporating SRA than the control (**Table 5.6**). This indicates that SRA addition had reduced the syneresis effect of the C-A-S-H gels.

## 5.3 Concluding remarks

1. Adding shrinkage reducing admixture reduced AAS paste's pore solution's surface tension efficiently up to a critical concentration (i.e., 9%).
2. SRA affected the soluble amount of ionic species reducing the AAS pore solution's alkalinity, retarding alkaline activation rate, and extending the setting time.
3. Adding SRA reduced shrinkage associated with the syneresis of C-A-S-H gels as a result of the lower polymerization degree.
4. Increasing SRA enhances the formation of hydrotalcite crystals, which contribute to enhancing the stability of the microstructure and compensating for the shrinkage.
5. The influences of SRA on surface tension, hydration rate, formation of C-A-S-H, and IRH dominate the resultant AAS's shrinkage.

# Chapter 6 - Understanding the shrinkage behavior of alkali-activated slag binders modified by the superabsorbent polymer

## 6.1 Introduction

Shrinkage is an important property in alkali-activated slag systems (AAS) due to the high potential for cracking and consequently the compromise for durability performance. Several types of shrinkage contribute to the total deformation including chemical, autogenous, and drying (Sakulich & Bentz, 2013). However, the cracking of AAS concrete is highly related to autogenous and drying shrinkage. Autogenous shrinkage is driven by the internal self-desiccation process induced by the hydration progress as pore solution is consumed leading to a drop in the internal relative humidity (IRH). This will also be accompanied by an increase in mesopores volume (Neto et al., 2008). The drying shrinkage induced by water loss due to evaporation has also a significant contribution to total shrinkage (Thomas et al., 2017). Studies on the early age shrinkage of AAS indicated that the most critical period is the first 7 days during which around 50% of the total shrinkage occurs (Al Makhadmeh & Soliman, 2020; Chen et al., 2021; Thomas et al., 2017). Hence, mitigation of early age shrinkage is an important measure to ensure the durability of AAS systems.

Among several available mitigation techniques, internal curing (IC) with the aid of a curing agent is a very effective technique to maintain the IRH level of the concrete. According to previous studies, internal curing limits the autogenous shrinkage (Henkensiefken et al., 2008; Stefan et al., 2018), reduce the cracking tendency of concrete (Lura & Bisschop, 2004; Stefan et al., 2018), and enhance its durability (RILEM TC-196, 2007). Two main curing agents are commonly used, pre-wetted lightweight aggregate (LWA) and superabsorbent polymer (SAP) (Babcock & Taylor, 2015). LWA has been widely applied in high-strength concrete (Bentur et al., 2001). (Sakulich & Bentz, 2013)confirmed the efficiency of pre-wetted LWA to mitigate autogenous shrinkage in slag activated by waterglass. Moreover, the inclusion of fully saturated blast-furnace slag coarse aggregate in AAS decreased the drying shrinkage by about 40% (Collins & Sanjayan, 1999). However, SAP exhibited higher absorption capacity and a lower

water release rate and can be used as a dry admixture during mixing concrete (Beushausen et al., 2014; Jensen & Lura, 2006; Liu et al., 2017).

SAPs are a special kind of polymeric gel that has a cross-linked structure, with water absorption of up to 500 times of its mass (Snoeck et al., 2015). The osmotic pressure difference inside the gel structure is responsible for its super absorbency (Liu & Rempel, 1997). During the mixing process, SAPs absorb water and swollen hydrogels are formed. The absorbed water in SAPs will release during hydration to compensate for the self desiccation. However, after releasing the water, SAP induces macro voids in the dense matrix, subsequently, the mechanical properties of concrete will be affected (Wehbe & Ghahremaninezhad, 2017).

On the other hand, limited data in the literature about the SAPs performance in alkali-activated systems. (Oh & Choi, 2018) found that 0.3% SAP reduced the autogenous shrinkage of AAS by around 60%. 0.3-0.6 wt.% SAP was effective in reducing the autogenous shrinkage of AAS as it maintained a high IRH (Oh & Choi, 2018). Also, it highlighted the effect of activator types on the optimum SAP dosages (i.e., > 0.6% for AAS mortars activated by waterglass). Despite this potential and the concluded results, research in this field is still limited. For instance, SAPs absorption mechanisms in AAS extracted pore solutions are not fully understood. Moreover, the effect of SAPs on the reaction kinetics and the microstructure evolution still needs further investigation. Additionally, a potential effort should be given to identify a suitable benchmark for SAPs addition in the AAS system, considering their efficiency in mitigating the shrinkage and balancing the impact of their induced macro voids on AAS properties.

Therefore, this study focuses on the interactions between SAPs and pore solutions for the AAS system. More specifically, this dissertation highlights the absorption/desorption mechanisms of SAPs in AAS pastes and links this knowledge to the efficiency in mitigating shrinkage. Additionally, this dissertation shall determine the suitable content rate of SAP that should be used in the AAS system to attain a specific performance level. The shrinkage behavior for drying shrinkage measurements in SAP-modified AAS and the ability of SAP in mitigating the shrinkage under a dry environment was also tested. To the best of the knowledge of the authors at the time of submission, this shrinkage behavior has not been investigated previously. This

work aims to contribute towards supporting the practical applications of SAPs in AAS systems, especially in some conditions when increasing the curing time can not be implemented.

## 6.2 Specific materials and working approaches

It is well known that the SAPs absorption capacity may significantly be affected by the presence of divalent ions, especially $Ca^{2+}$. In a first step, SAPs absorption in extracted AAS pore solution was measured. In a second step, the interaction of SAPs particles and $Ca^{2+}$ ions was estimated by investigating the extracted pore solution after 3h of mixing by ICP-AES. Moreover, the desorption kinetics of SAPs (i.e., amount and period of releasing) is crucial as it influences the efficiency to counteract the shrinkage. Therefore, the desorption kinetics of SAP in AAS pastes were monitored with hydration time by using computed X-ray computed tomography.

Angular covalently crosslinked sodium polyacrylate SAPs particles were used (**Fig 6.1**). The SAPs percentages were added at rates 0.3%, 0.6%, and then 0.9% (wt) of the GGBS and designed as SAP3, SAP6, and SAP9, respectively. Extra water was added to the SAP mixtures following the previous recommendation (assuming SAP absorbs the same amount) (Oh & Choi, 2018). For each total w/b ratio, an AAS mixture was prepared and tested as a control mixture. **Table 6.1** shows the composition for tested mixtures. Hydration kinetics were studied by isothermal heat flow calorimetry and thermogravimetric analysis (TGA) was applied to estimate the hydration degree. Moreover, in this study, autogenous, total drying shrinkage tests, and continuous monitoring of internal relative humidity change were performed.

The microstructure of AAS pastes incorporated with SAPs was qualitatively described by SEM. Energy-dispersive X-ray spectroscopy microanalysis (EDX) was also used to detect the reaction products around the SAP voids. Additionally, mercury intrusion porosimetry (MIP) was used to investigate the influence of SAPs on the internal pore structure and obtain the pore size distributions.

Table 6.1 Mixtures of paste and mortar samples

| Mixtures | Effective w/b | Extra w/b | SAP% |
|---|---|---|---|
| C3 | 0.42 | 0 | 0 |
| C6 | 0.44 | 0 | 0 |
| C9 | 0.46 | 0 | 0 |
| SAP3 | 0.4 | 0.02 | 0.3 |
| SAP6 | 0.4 | 0.04 | 0.6 |
| SAP9 | 0.4 | 0.06 | 0.9 |

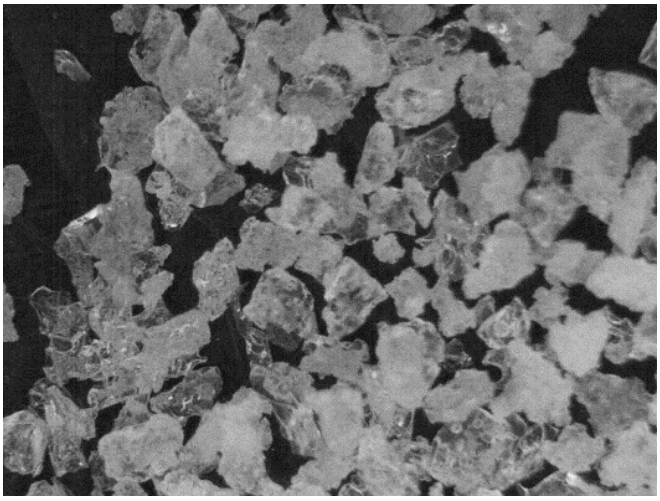

Fig. 6.1. Image of the SAP powders used in the experiments by optical microscope

## 6.3 Results and discussion

### 6.3.1 SAP absorption in AAS pore solution

The mechanism of SAP absorption primarily relies on the osmotic pressure difference concept as described in Eq. (6.1). Moreover, the absorption amount, kinetics, and stability of the swollen hydrogel depend on various thermodynamic and kinetic factors (Richter et al., 2008).

$$\Delta_{\pi} = \Delta_{\pi(\mathrm{mix})} + \Delta_{\pi(\mathrm{elastic})} + \Delta_{\pi(\mathrm{ion})} + \Delta_{\pi(\mathrm{bath})} \quad 6.1$$

Once SAP particles get in contact with the water, the polymer-water-interactions raise the osmotic pressure ($\Delta_{\pi(mix)}$). After that, the hydrated polymer chains start to expand, and consequently, an elastic force is generated to counteract this expansion and to balance the pressure due to their cross-linking interactions $\Delta_{\pi(elastic)}$. The SAPs used in this experiment are Acrylic-based polymers, which are negatively charged (Richter et al., 2008). Hence, a strong electrostatic repulsion is generated as a result of the interaction of polyelectrolyte hydrogels with neighboring chains which are already charged likewise. This expansive pressure ($\Delta_{\pi(ion)}$) can contribute to the balance of the osmotic pressure (RILEM TC 260-RSC).

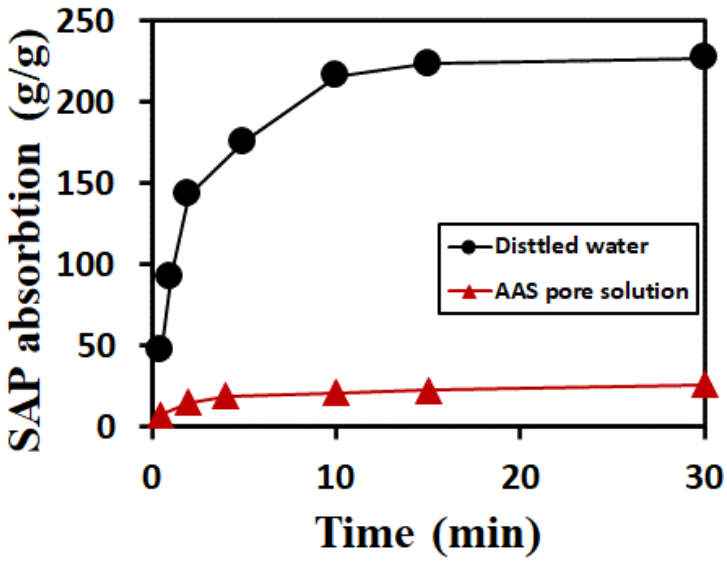


Fig. 6.2. Absorption of SAP in distilled water and extracted AAS pore solution.

As shown in **Fig. 6.2**, the SAP absorbs deionized water quickly (i.e. 15-30 min) and reaches complete saturation at ~227 g/g water, which is comparable with the reported data for this SAP (Snoeck et al., 2014). For the AAS pore solution, the absorption capacity was only ~25 g/g, which is reported similarly for synthetic pore-fluid of AAS by waterglass (29.9g/g) (Song et al., 2016). This reduction can be attributed to the increase in the ion's concentration, which leads to a reduction in the osmotic pressure, and consequently, water absorption (Richter et al., 2008; Schröfl et al., 2017). It was reported that the existence of mobile ions of $Ca^{2+}$ in the pore solution can form complexes interactions with the anionic hydrogels of the polymer network. Thus, a polyelectrolyte shielding ($\Delta_{\pi(bath)}$) decreases the osmotic pressure, which aligns with a hydrogel

shrinkage (Kang et al., 2017; Richter et al., 2008). However, the AAS pore solution contained a considerable concentration of cations and $Ca^{2+,}$ which originated from the partial dissolution of the slag (Puertas, Fernández-Jiménez, et al., 2004). The control pastes without SAP exhibited a higher concentration of $Ca^{2+}$ ions than that of the SAPs modified paste. For instance, the $Ca^{2+}$ ions in control mixtures were 0.9 mmol/l compared to 0.66 mmol/l in mixtures incorporating 6% SAPs. This indicated the development of polymer chain crosslinking due to the binding of $Ca^{2+}$ ions. This mechanism is illustrated in **Fig. 6.3b** which shows additional crosslinking of polymer chains. In conclusion, the reduction of water absorption in the AAS's pore solution is attributed to the interaction of $Ca^{2+}$ ions with anionic groups of the polymer networks and the charge screening effect (Puertas, Fernández-Jiménez, et al., 2004). Based on Eq. (6.1), this interaction results in electronic shielding that contribute to reducing the osmotic pressure inside the gel, leading to a reduction in absorption tendency and SAP swelling (Richter et al., 2008; Schröfl et al., 2012). However, the reported SAP absorption in OPC pore solution was around 16g/g, which is less than that in the AAS system (25g/g). This can be attributed to the higher concentration of $Ca^{2+}$ in the pore solution of OPC leading to higher electronic shielding, resulting in lower absorption capacity (Justs et al., 2015)

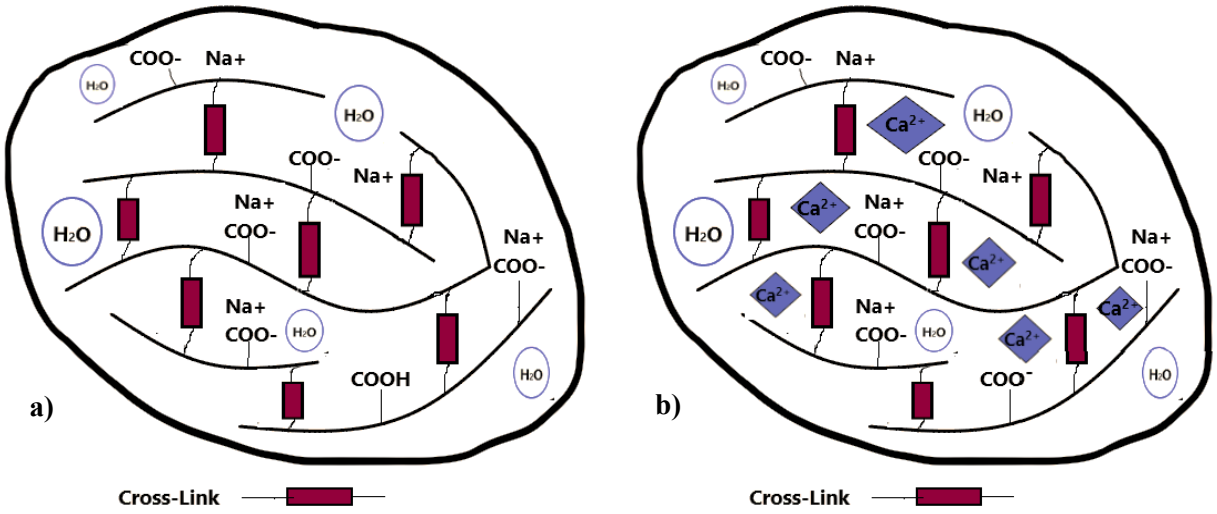


Fig. 6.3. Schematic representation of a crosslinked SAP network (a) interaction with water (b) interaction in the extracted pore solution of AAS paste

### 6.3.2 Compressive Strength

There has been a limited amount of research investigating the effect of the addition of SAPs on the mechanical properties of AAS. **Figure 6.4** shows the compressive strength results at ages 3, 7, and 28 days. For SAP mixes, a significant decrease in 7-day compressive strength was observed, where the strength reductions were 13%, 24%, and 24% for SAP3, SAP6, and SAP9 mixes, respectively. At 28 days, the trend changed, as shown in **Fig. 6.4.** This compares SAP3 and C3, which both have the same total w/b ratio of 0.42. It is interesting to observe that the 28-compressive strength of SAP3 is noticeably higher than that of C3 by about 7%. This proposes that at the low addition of SAP, the 28-day (and later) compressive strength loss effect of IC water entrained by SAP is lower than that of the free mixing water for mixes SAP3. Moreover, a the 28-day strength was slightly reduced by around 5% with the addition of 6% SAP to C6. However, the strength difference at 28 days is reduced for SAP3 and SAP6 compared to C3 and C6, respectively, compared at the age of 7 days. This enhancement in the compressive strength could be attributed to the counterbalance effect, where after the swollen SAP dries out, large voids of >100 μm are expected to form which contributes to a strength loss. On the other hand, SAP can entrain liquid slowly, which leads to enhancement in the hydration degree at a later age. Hence, hydration proceeds further in SAP3 and SAP6 which helps in compensating for the additional porosity at a later age (Dudziak & Mechtcherine, 2008; Mechtcherine et al., 2008).

Contrary to mixes SAP9 and C9 which exhibited opposite trend, whereas a significant strength loss of 22% occurred by inclusion 9%. However, a high dosage of SAP (i.e., 0.9%) contributes to impact the matrix by inducing large voids. Hence, it can be stated that the effect of the addition of 0.9% SAP in AAS can't compensate for the strength loss due to the induced high void volume.

As shown in **Fig. 6.4**, it seems that at a high dosage of SAP (i.e., >0.3%) the reduction in the strength due to voids formation will be dominating.

Furthermore, a higher w/b ratio for AAS mixtures leads to a decrease in compressive strength. According to (Yuan et al., 2015), the w/b ratio is a critical factor determining the strength of AAS (Behfarnia & Rostami, 2018). These trends are generally in line with those observed in OPC (Hasholt et al., 2012; Justs et al., 2014).

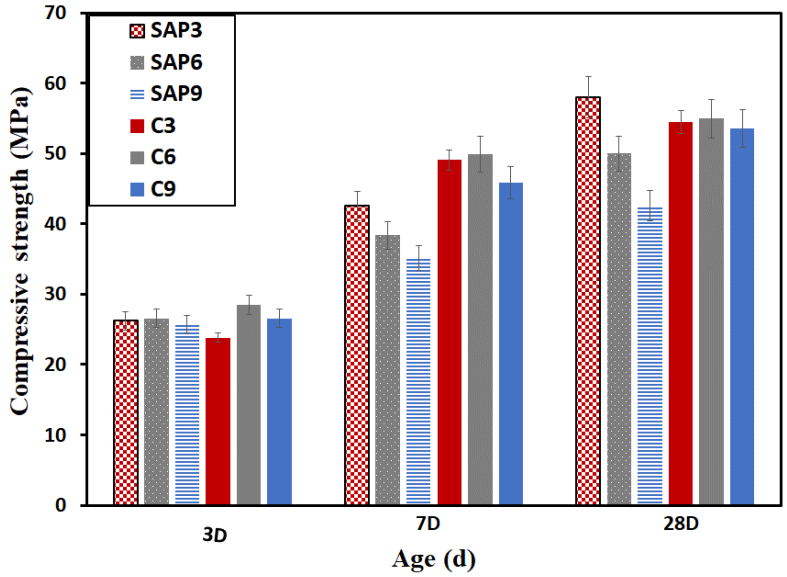


Fig. 6.4. Compressive strength for AAS mortars with and without SAPs

### 6.3.3 Effects of SAP on the kinetics of AAS hydration

The hydration kinetics of AAS was investigated by using isothermal calorimetry. **Figure 6.5** shows the heat flow profile for various AAS mixtures that exhibited a similar trend to that of OPC systems (Ravikumar & Neithalath, 2012). Generally, the incorporation of SAP prolonged the induction period and delayed the acceleration peaks while reducing their height intensity. This observation suggests that SAP has a retardation effect on AAS hydration (**Fig. 6.5a**). **Figure 6.5b** illustrates the cumulative heat released at 7 days. All mixtures incorporating SAPs exhibited lower hydration degrees compared to the control mixtures. This reduction in the relative hydration degree can be possibly ascribed to the slow-releasing rate for the solution retained inside SAPs (Justs et al., 2015).

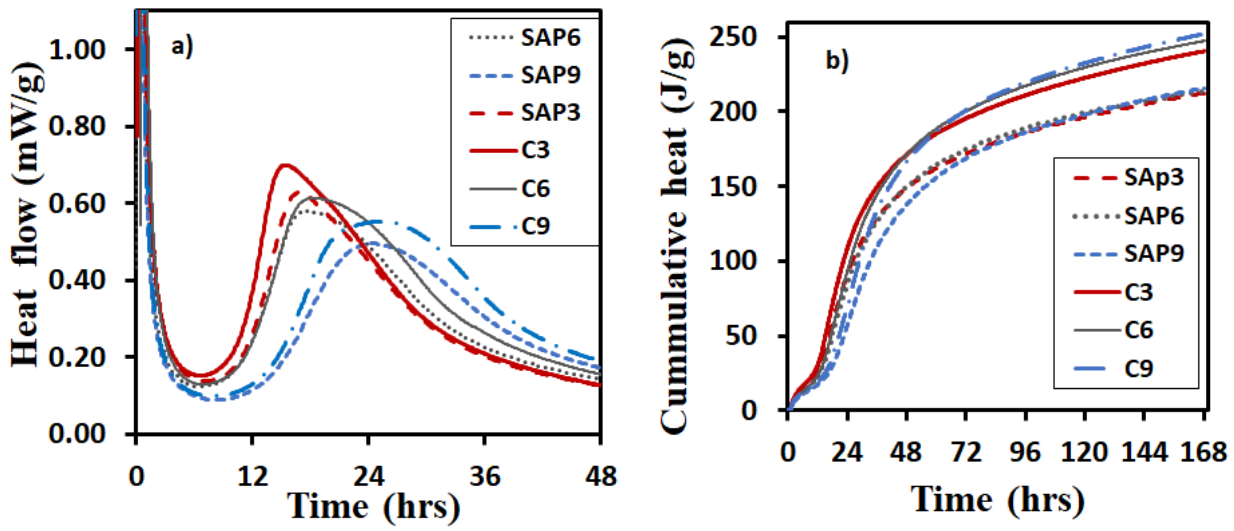


Fig. 6.5. (a) Heat flow (b) Cumulative heat flow up to 7 days of AAS pastes

Another interesting point is to compare the effect of the w/b ratio without SAPs to the w/b ratio with the presence of SAPs on the hydration kinetics of AAS. Increasing the w/b ratio in control mixtures (i.e., C3, C6, and C9) enhanced the slag hydration while promoting a higher exothermic peak (**Fig. 6.5a**) and degree of hydration at 7 days (**Fig. 6.5b**). Mixtures incorporating SAPs showed reduced hydration peaks and a slightly longer dormant period compared to mixtures without SAPs when having the same total w/b ratio. Hence, enhancement for slag hydration by free mixing water is higher than that induced by water entrained in the SAPs. This can be ascribed to the uniform distribution for the free water in the matrix and high contact with slag grain. On the other hand, the entrained liquid by SAP is not instantaneously available or not enough during the corresponding hydration period (Justs et al., 2014). Furthermore, $Ca^{2+}$ alkali ions, dissolved from slag, are likely taken up by SAPs, leading to a lower concentration in the pore solution (**Table 6.2**). This will affect the Ca/Si ratio and consequently the formation of C-A-S-H gels as confirmed by the low hydration peaks.

Mixtures without SAPs exhibited a longer acceleration period while the w/b ratio increased when compared to mixtures with SAPs (**Fig. 6.5a**). In principle, increasing the w/b ratio increases the initial interstitial porosity of the paste and the connectivity (Justs et al., 2015; Ye, 2003). Furthermore, at the same w/b ratio, SAP absorbed the liquid and swelled, inducing macro voids

inside the matrix, which reduces the interstitial pore space between slag particles (**Fig. 6.6**). Hence, a smaller space is available for the formed hydration products around the slag particles, which increases the solid-phase percolation in SAP mixtures (Justs et al., 2015). After the formation of a large amount of reaction products in the limited interstitial space, this will depress the further dissolution of slag and ions mobility (Ye, 2003). Thus, there is a slower reaction rate of SAP mixtures when compared to the paste without SAP at the same w/b ratio, especially after the acceleration period (i.e., 36h) (**Fig. 6.5b)**. Moreover, the increased total degree of hydration for AAS mixtures while the w/b ratio increased is similar to reported findings for OPC paste (Justs et al., 2015; Justs et al., 2014; Ye, 2003; Zhang et al., 2012). This also suggested that the stored liquid in the SAP had not been released completely during the first 7 days, increasing the potential for further hydration progress at later ages.

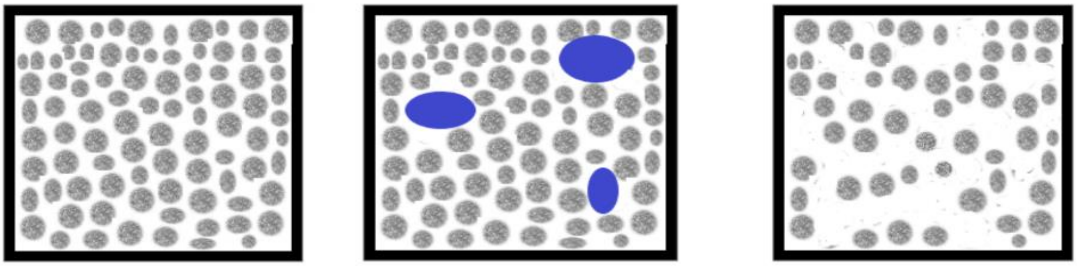

Fig. 6.6. Schematic representation of the phase distribution of (a) AAS without SAP with w/b of 0.42; (b) SAPs internally cured paste with extra water (w/b 0.42); (c) and paste with extra water but without SAPs (w/b 0.46) (Justs et al., 2015)

It is clearly seen that increasing the w/b ratio affects the slag hydration, as evidenced from the long-dormant period for mixtures C9 compared to C3 and C6. This initial retardation in the reaction process is attributed to the dilution effect of the additional water which affects the alkalinity of the alkali activator and reduces the ion concentrations in pore solution by increasing the w/b ratio (Yuan et al., 2015). The electrical conductivity was used as an indirect indicator for the alkalinity since the hydroxide ions have higher conductivity than the other ions present in these solutions (Snyder et al., 2003). The conductivity for activator solutions was measured as a function of the w/b ratio (C3, C6, and C9). As shown in **Fig. 6.7,** C3 exhibits the highest alkalinity level, which promotes the formation of larger initial amounts of C-A-S-H, leading to high $Ca^{2+}$ and $Al^{3+}$ ions dissolved from the slag. This is evident from the increased intensity of

peak and a short dormant period for C3, as compared to C6 and C9. As commonly shown in research, during the initial stage of the activation process, the high pH activator breaks the Ca-O, Al-O, and Si-O bonds on the slag surface (Puertas, Fernández-Jiménez, et al., 2004). The dissolved species in the solution from the slag particles are in the form of $Ca^{2+}$, $[H_2SiO_4]^{2-}$, $[H_3SiO_4]^-$ and $[H_4AlO_4]^-$. The microstructure of the AAS is generated by precipitating these compounds as their concentration reaches solubility of different phases and solid compounds (FernandezJimenez & Puertas, 1997; Puertas, Fernandez-Jimenez, et al., 2004). Hence, the long-dormant period for C6 and C9 is attributed to the increased time required for the ionic species in the pore solution to reach the critical concentration and to form the hydration products (Fernandez-Jimenez & Puertas, 2001; Provis & van Deventer, 2007). This retardation vanished after the acceleration period. However, although there is initial retardation, the C9 mixture exhibited the highest hydration degree at the age of 7 days, as shown in **Fig. 6.5b**. This can be explained by the fact that slag particles in the C3 mix exhibit a finer interstitial porosity (**Fig. 6.6a**) which means a shorter distance for the dissolved ions ($Ca^{2+}$ and $Al^{3+}$) from the slag surface to diffuse through, meaning they form further reaction products quicker. Meanwhile, as illustrated in **Fig. 6.6c**, a higher w/b ratio contributes to having a higher amount of water in the interstitial spaces, as well as the increased absolute amount of silicate species and alkali ions in the interstitial space. Thus, after reaching the critical concentrations of the reaction products, the larger available amount of reactants leads to higher total heat. This is in line with the results as indicated in **Fig.6.5b.**

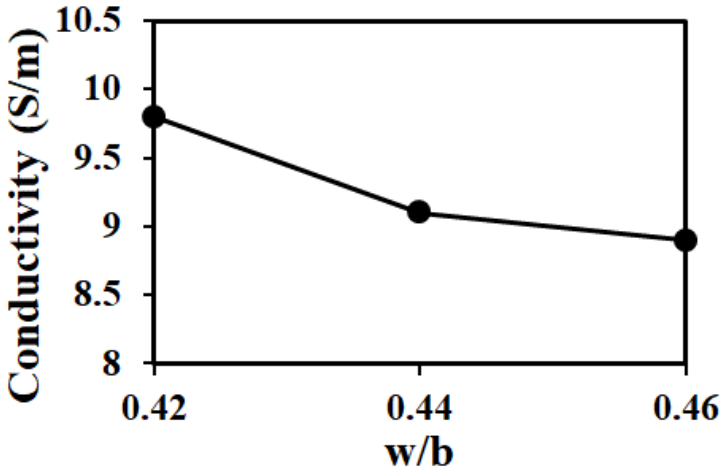


Fig. 6.7. Electrical conductivity of the activator solution based on various w/b ratios.

### 6.3.4 Computed tomography (Micro CT)

SAPs ‘s releasing process was evaluated in AAS paste under the sealed and unsealed condition

#### 6.3.4.1 SAP desorption kinetics under sealed condition

The X-ray microtomography results for the sealed sample at the age of 5h, 2 days, and 7 days are shown in **Fig.6.8**. Three phases were distinguished from the tested cross-section. The light grey represents the AAS paste, including the unreacted slag particles in the white color, and the SAP with liquid and entrapped air is represented by dark grey and black, respectively.

The SAP particles start to absorb the liquid and swell once they are in contact with the solution during the mixing process (Justs et al., 2015). As illustrated in **Fig. 6.8a**, the SAP particles are distributed randomly within the paste, reaching a size of 0.9 mm after solution absorption. After 5h of hydration, voids started to form inside swollen SAP, indicating the initiation for liquid desorption from SAP particles (**Fig. 6.8b**). This confirms the inside-out drying process of SAP, where the particles are emptied from the inside, as reported in the OPC system (Lee et al., 2010). At 2 days, the area of voids increases, which confirms that SAPs have released more entrained liquid. This quick moisture expending during the reaction process coincides with the time of the acceleration peak, and subsequently, more moisture is released from the agents to meet the reaction demands. At the age of 7 days, the dark grey color indicates that a significant portion of the liquid inside SAP particles in the shown cross-section has been consumed (**Fig. 6.8c**).

Part of the liquid is still stored inside the SAP, which can be used for further hydration after 7 days. Furthermore, the results showed that the internal curing sources were not emptied at 7 days, hence, it can be concluded that no self-desiccation took place during this period, which results in the low capillary stress and the subsequently low autogenous shrinkage (Sakulich & Bentz, 2013). Moreover, the volume of unreacted slag particles in the white color reduced with time, confirming the hydration progress.

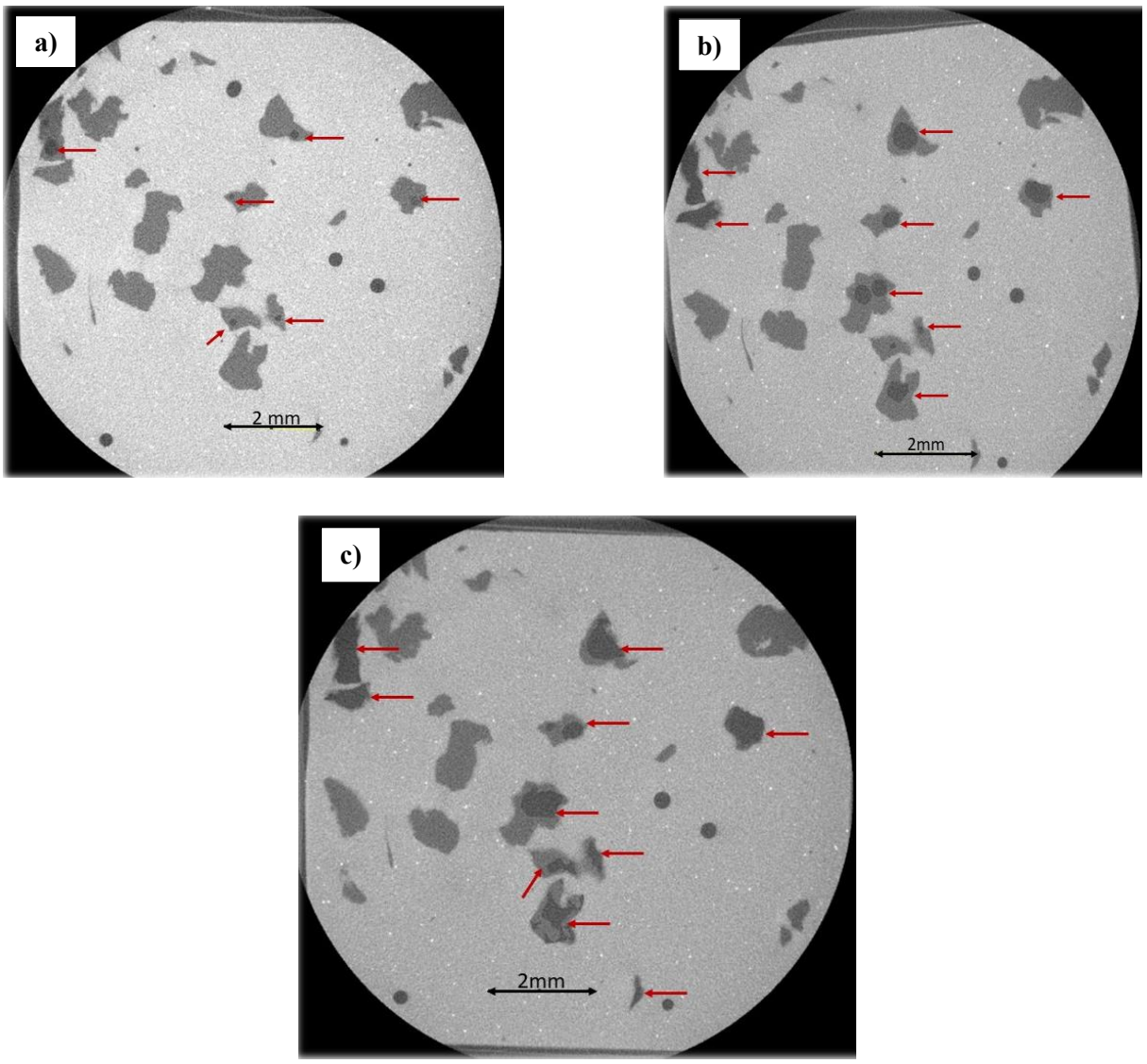


Fig. 6.8. A cross-section of AAS pastes incorporated by 0.6% of SAP by Micro-CT at the age of (a) 5h (b) 2days and (c) 7 days.

### 6.3.4.2 SAP desorption kinetics under dry condition

**Figure 6.9** represents the desorption mechanism of SAPs when exposed to a dry environment. After 5 hrs, the sample was still sealed and not exposed yet for drying, hence, the SAP particles were almost full of liquid, as shown earlier (**Fig. 6.8a**). At the age of 3 days, the volume of the black region (entrapped air) increased significantly, indicating a high amount of liquid desorbed from the SAPs **(Fig 6.9a).** At age 7 days, SAPs are empty, and all the liquid had been released to

the matrix (**Fig. 6.9b**). Furthermore, the micro-cracks start to form within the matrix at the age of 7 days.

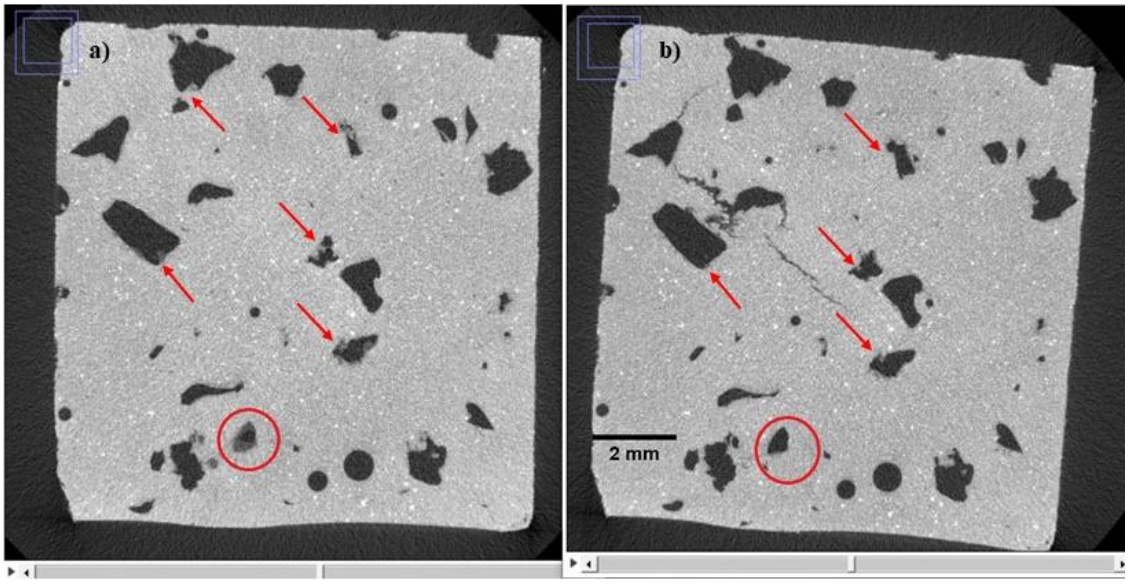


Fig. 6.9. A representative cross-section of SAP6 AAS paste by X-ray CT represents the desorption mechanism of SAP under drying conditions at age of (a) 3 days (b) 7 days.

### 6.3.5 Internal IRH

**Figure 6.10** shows the development of the IRH in control mixtures, as well as in mixtures with three pre-set levels of SAPs when sealed and exposed. At 7 days, the IRH of the control mixtures is about 82% and steadily decreasing. The drop in IRH is related to the self-desiccation that occurred as the hydration is ongoing. Noticeably, AAS mixtures internally cured with SAPs delay the development of self-desiccation, keeping the IRH at high levels. The higher the SAPs content, the higher the IRH level. As shown in **Fig. 6.10a**, the drops in IRH for 0.6% and 0.9% of SAP took place after the first 14 days of AAS hydration, indicating that the self desiccation was effectively mitigated. This agrees well with X-ray tomography results indicating the existence of water in the SAP6 mixture after 7 days, which guaranteed the needed saturated conditions for hydration to progress. Contrarily, mixtures with 0.3% of SAP experienced a gradual drop in the IRH, indicating a rapid consumption of moisture. Meanwhile, mixtures without SAPs undergo a severe drop in IRH. For instance, the IRH drop for C3 and C6 mixtures at 7 days were around 16% and 15%, respectively. This reveals that the additional free water

(i.e., higher liquid content) did not play a predominant role in tuning the IRH level and was less effective than SAPs cured AAS mixtures.

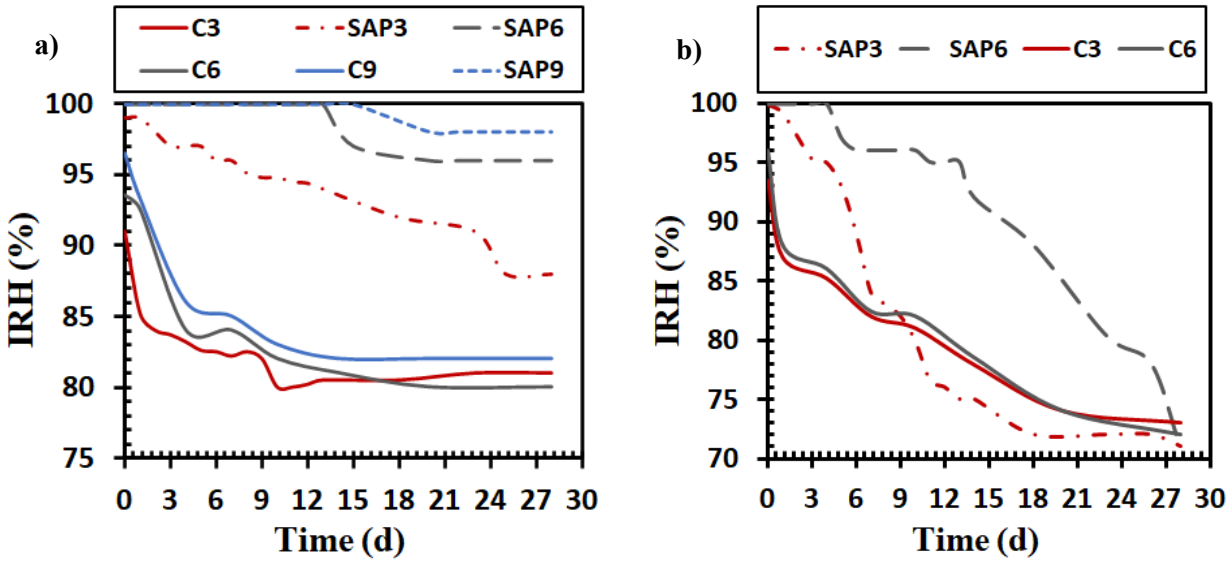


Fig. 6.10. Influences of SAP dosage and w/b on the internal relative humidity of AAS under (a) sealed; (b) drying conditions

The internal humidity development of the AAS mixture, when exposed to a dry environment, is illustrated in **Fig. 6.10b.** Internally cured mixtures by SAP heightened the reduction rate of IRH. The IRH drop is delayed in SAP6 mixtures and starts to drop at the age of 5 days. As explained in the X-ray tomography (**Fig. 6.8**), SAPs released all of the stored liquid inside the AAS matrix, which helped to maintain the IRH at a high level. However, the SAP3 mixture starts to drop earlier and experienced a steeper slope of reduction. This indicated that the incorporation of 0.3% of SAP is less efficient in maintaining the IRH, and the liquid amount absorbed by 0.3% of SAP was not enough to meet the drying demand. Generally, the higher the SAP dosage, the longer the time needed for IRH to start dropping.

### 6.3.6 Autogenous shrinkage

During hydration, SAPs can reduce self-desiccation and maintaining a high IRH level. Moreover, autogenous shrinkage is highly correlated to the IRH drop rate, in that the slower the IRH rate drops, the reduced amounts of developed autogenous shrinkage (Chen et al., 2021).

**Figure 6.11** illustrates the influence of internal curing on the AAS autogenous shrinkage over the investigated period. Measured autogenous shrinkage decreased as the SAP dosage increased. For example, adding 0.6% and 0.9% of SAP had mitigated autogenous shrinkage within the initial 28 days by around 90%. On the other hand, a slight change in the autogenous shrinkage occurred by increasing the w/b ratio. Control mixtures showed the highest early rate of shrinkage development, reaching -1300 με at 1 day and around -3000 με at 7 days. Water is consumed in the hydration process along with being physically absorbed by reaction products. This will lead to the formation of a high volume of mesoporous in the matrix and consequently greater capillary tension, which is the driving force for autogenous shrinkage (Lura et al., 2006; Sakulich & Bentz, 2013).

The IC water entrained by SAP is more effective in reducing autogenous shrinkage than adding free mixing water. For instance, C9 exhibited -4590 με while SAP9 showed -328 με. As shown in **Fig. 6.11**, all mixtures free of SAPs experienced a more pronounced shrinkage development rate than those mixtures with SAPs due to the intense hydration. Whereas the IRH decreased significantly and caused capillary pressure, and the results of the autogenous shrinkage development correlate with IRH development over time (**Fig. 6.10a**).

Mixtures incorporating SAPs showed low shrinkage development even after the deceleration period (i.e., 7 days). Furthermore, this positive effect was more pronounced by increasing the SAPs dosage. This difference in shrinkage behavior between AAS mixtures with and without SAPs can be attributed again to the introduced IC water types that lead to different pore structures and hydration kinetics.

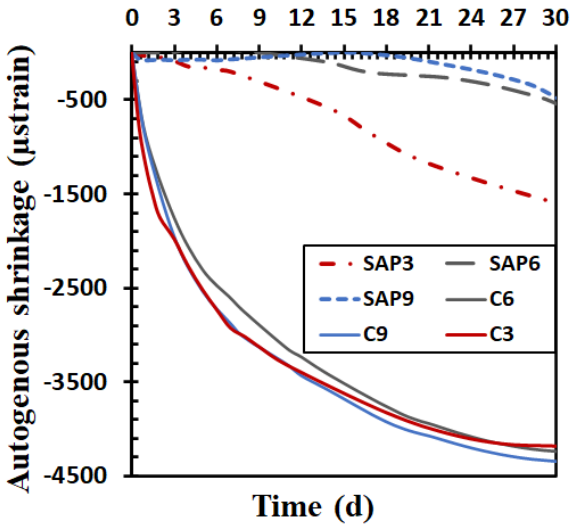


Fig. 6.11. Influences of SAP dosage and w/b on the autogenous shrinkage of AAS

The compensation factor (CF) of SAP dosages at various ages was calculated and shown in **Fig. 6.12**. Noticeably, 0.3% of SAP was not enough to compensate for the autogenous shrinkage, likely since insufficient water is available along with large spaces between effective SAP particles (space between SAP's cavities is larger than the influence zone of the curing liquid. This means that at the early age of slag hydration of SAP3 mixture, some point inside the matrix experienced self-desiccation. Consequently, this is due to that the entrained IC water doesn't need the hydration demand (Assmann, 2013). This agrees with the IRH development of AAS with 0.3% SAP, as illustrated in **Fig. 6.10a**. In contrast, the CF was higher for SAP6 and SAP9 and exceeds 1, which indicates a slight autogenous expansion during early ages. This expansion is attributed to the formation of rich Si gel leading to an overall expansion (Sakulich & Bentz, 2013). Nonetheless, the CF for all SAP dosages depleted with time. After 28 days, the CF for SAP6 and SAP9 were almost the same (i.e. around 90%) which is consistent with previously reported AAS results (Song et al., 2016). As the hydration is ongoing, the moisture entrained by SAP decreases gradually, resulting in a lower compensation at later ages. Micro CT results confirmed a high proportion of liquid released by the end of 7 days.

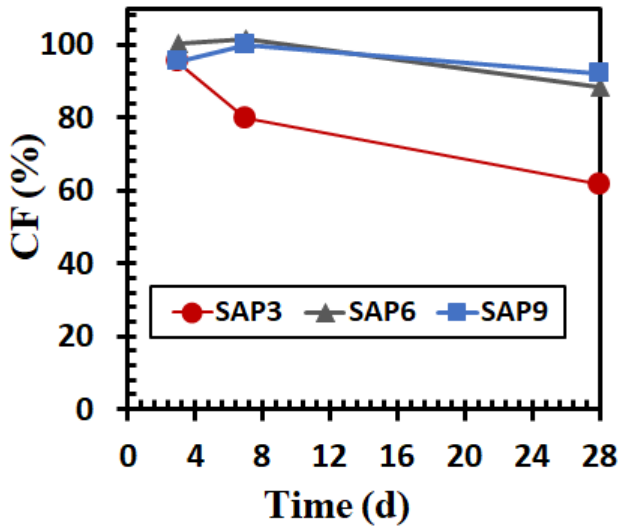


Fig. 6.12. Compensation percentage of AAS incorporated by SAPs

As shown in **Fig. 6.11 and Fig. 6.12**, increasing the SAPs dosage above 0.6% did not induce a significant reduction in the autogenous shrinkage. This indicates that adding 0.6% SAP was enough to compensate for the autogenous shrinkage and the SAP's liquid absorption capacity could already provide the needed moisture saturated condition to the AAS matrix. This was confirmed by IRH results (**Fig. 6.10a**) and also confirmed by the X-ray tomography results (**Fig 6.8),** where SAPs did not release the entirety of the absorbed solution to the matrix and continued counteracting of autogenous shrinkage during the deceleration period (i.e., 7 days). Hence, it can be stated that 0.6% SAPs is the optimal content in terms of autogenous shrinkage mitigation.

This means that at an increased content of superabsorbent polymer (i.e., >0.6%), not all the water from the SAPs is needed to alleviate autogenous shrinkage. This contributes to the further formation of macropores leading to a significant reduction in the compressive strength, as discussed in 6.3.2.

### 6.3.7 Total drying shrinkage

Drying shrinkage happens due to capillary water evaporation as a result of moisture gradient between the surface and inside of the matrix (Assmann, 2013). Thus, in the case of external

environmental contributions, the effectiveness of IC by SAP on the total shrinkage of the AAS system needs investigation.

The total shrinkage of AAS mortars exposed to 45±5% RH dry environment is shown in **Fig. 6.13**. The total shrinkage development had been affected by two factors: the inclusion of SAP and the amount of additional free mixing water. As shown in **Fig. 6.13**, the two factors had induced opposite trends. Adding more water resulted in higher total shrinkage, and the higher the total w/b ratio, the greater the shrinkage. Conversely, SAP internally cured AAS, which exhibited reduced shrinkage.

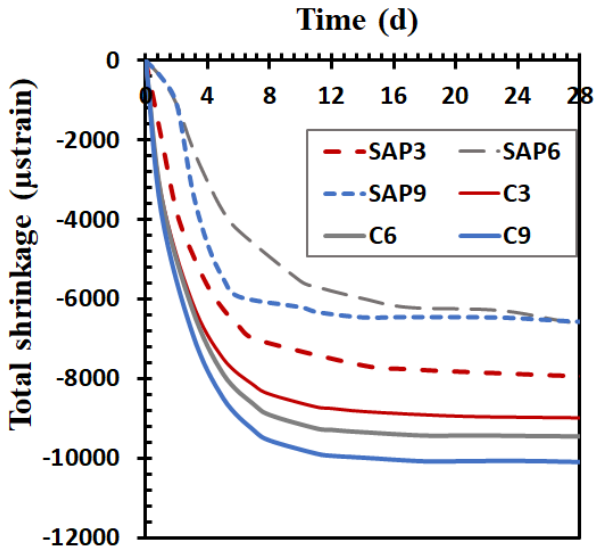


Fig. 6.13. The total shrinkage of AAS mortars

On the other hand, internal curing by SAPs showed a different trend especially at an early age (i.e. first 7 days). Mixtures with SAPs exhibited much lower shrinkage compared to those without SAP when both have the same total w/b ratio. **Figure 6.14** shows the compensation factor as a function of SAP dosage based on the same total w/b. Mixture SAP3 showed the lowest efficiency in mitigating the total shrinkage at 28 days by around 12%, while it was 30% and 35% for SAP6 and SAP9, respectively. This trend is analogous to the internal relative humidity development, explained earlier (**Fig. 6.10b**). SAP mixtures remarkably tuned the rapid reduction in IRH, specifically at higher dosage (i.e., 6% SAP) maintained the IRH above 90%

for the first 14 days. This was not achieved by increasing the free water addition. This indicates that self-desiccation is more pronounced for mixtures without SAPs. Moreover, the shrinkage measurements revealed that the influence of entrained liquid on autogenous shrinkage overrides the influence of residual shrinkage. This indicates that the enhancement caused by SAPs to the overall shrinkage behavior of AAS is related to the IC effect caused by liquid release from SAP during the drying process rather than a chemical effect.

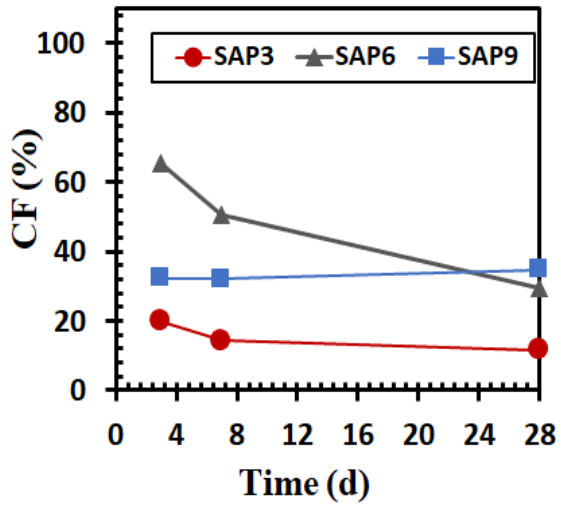


Fig. 6.14. Compensating percentage for total shrinkage of AAS incorporated by SAP

### 6.3.8 Internal pore structure

The effect of SAP on the pore structure of AAS is investigated using MIP. The pores in AAS can be classified as gel pores, capillary porosity, and voids. Gel porosity ranges from 2-10 nm, which is directly proportional to the hydration degree. Capillary porosity (d >10 nm) is related to both the w/b ratio and hydration kinetics (Kumar & Bhattacharjee, 2003). As shown in **Fig. 6.15a,** increasing the SAP dosage or the total w/b increases the AAS total internal porosity.

In principle, when the weff/b ratio increases, the volume fraction of capillary pores also raises. High weff/b leads to more interstitial spaces (which would contain capillary liquid) in the matrix at early ages, as illustrated in **Fig. 6.6b, c** (Jensen & Hansen, 2001; Li et al., 2020; Powers & Brownyard). Therefore, the space after the hydration and self desiccation would be

larger (Powers & Brownyard). Noticeably, the inclusion of SAP decreased the porosity when compared to the control mixtures at the same total w/b ratio. For instance, SAP6 decreased the percentage of fine pores with diameters ranging from 10-100 nm compared to C6. This can be attributed to less available free water (lower weff/b ratio than C6). Despite the confirmed early liquid releasing from SAPs to the AAS matrix (i.e., after setting time as confirmed by Micro-CT), the internal pore structure of AAS is already formed, which is linked to the initial $w_{eff}$/b ratio (Scrivener et al., 2016). Therefore, C6 showed higher porosity. This indicates that, after forming the initial pore structure, the AAS microstructure is more dense due to the IC effect (Oh & Choi, 2018).

It can be concluded that the different spatial distribution of the liquid in both types, namely the control and SAP mixtures, lead to different pore structures in AAS hardened pastes (**Fig. 6.6**). Furthermore, the changes in the porosity by MIP coincide with those in the reported strengths earlier **(Fig. 6.4).** The incorporation of SAP increased the proportion of micro-voids. Moreover, increasing the SAPs dosage contributed to a higher proportion of micro voids, as shown in **Fig. 6.15b**. For instance, the inclusion of high content of SAPs (i.e., 0.9%) led to the formation of a high proportion of micro voids, which significantly reduced strength.

Moreover, the initially formed porosity induced either by SAPs or additional water may not be significantly compensated by the advanced hydration (Justs et al., 2015).

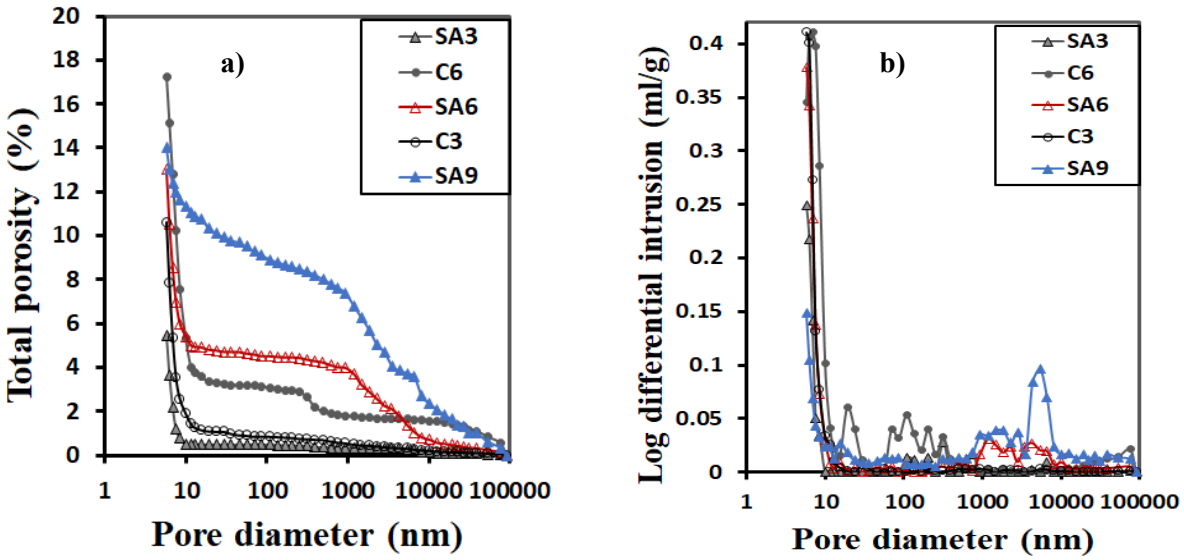


Fig. 6.15. (a) Cumulative porosity; (b) Pore size distribution of AAS pastes incorporated by SAPs.

### 6.3.9 Surface porosity

The formed voids by SAP cannot be detected by MIP, which are considered sealed pores. Therefore, they can be evaluated by analyzing the open porosity of the mixtures (P. Kumar Mehta & Paulo J. M. Monteiro, 2014).

The effect of SAP on the surface porosity of AAS was evaluated based on the vacuum absorption results (Behfarnia & Rostami, 2018; P. Kumar Mehta & Paulo J. M. Monteiro, 2014). **Figure 6.16** represents the results of the surface porosity analysis at 28 days. The influence of the w/b ratio on the surface porosity is more pronounced than the SAPs mixtures. The most significant reduction was induced by adding 0.6% SAP (i.e., around 18% compared with C6). Thus, it can be stated that SAPs improved the surface porosity of AAS mixtures at the same total w/b ratio.

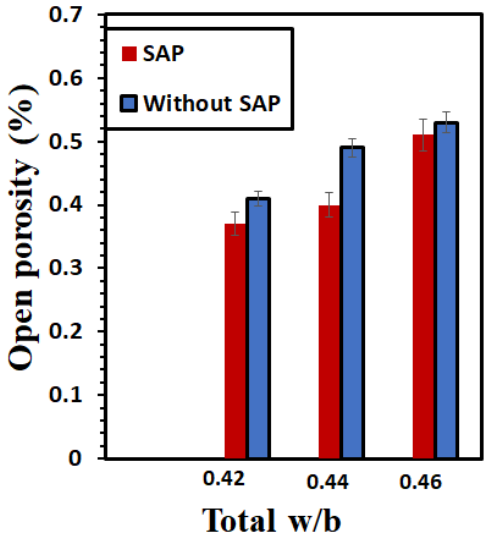


Fig. 6.16. Open porosity of AAS with and without SAP

According to Mehta and Monterio (2013), drying mass loss is water evaporation under drying conditions and is directly related to the surface pore structure. The change in the amount of evaporation means different surface porosity. **Figure 6.17** shows the mass loss of mixtures with and without SAP. Increasing the total w/b ratio or the SAP dosage contributed to higher drying mass loss. Meanwhile, at the same w/b ratio, SAP reduced the mass loss. For instance, SAP6 lost less mass than C6. This indicated better water retention for specimens internally cured by SAP and improved abilities to direct the internal curing water to enhance hydration. However, at a high dosage of SAP (i.e., 0.9%), the SAP9 mixture showed an opposite trend in mass loss and showed a high evaporation rate.

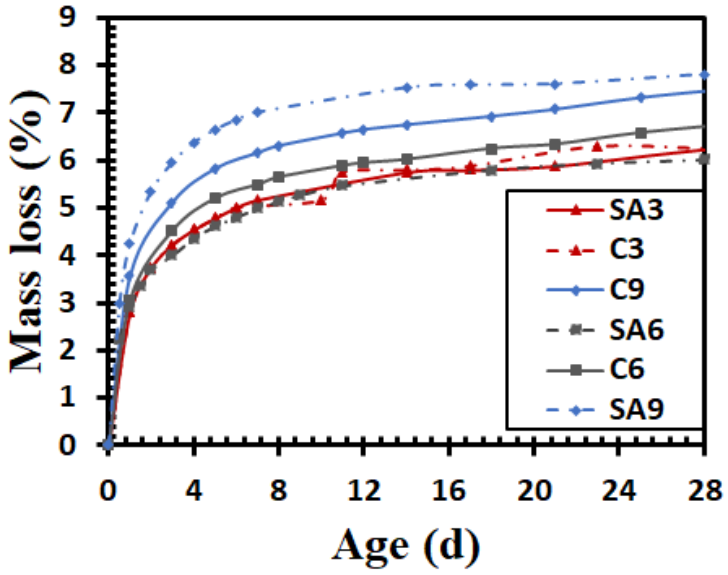


Fig. 6.17. Mass loss for AAS mixtures with and without SAP

Nevertheless, both results from vacuum absorption and mass loss show that samples with reduced mass loss demonstrated lower surface porosity, as shown in **Fig. 6.16 and Fig.6.17**. Consequently, water permeation is reduced effectively by SAP addition. However, SAP9 showed an opposite trend, which is attributed to its impact on the matrix densification, as shown in the internal porosity results (**Fig. 6.15**). Nevertheless, SAP9 decreased the shrinkage by around 30% when compared to the control mix C9, despite the higher evaporation rate. This can be ascribed to the fact that water in SAP9 seems to evaporate easier from the larger pores, which have higher mobility and causes less shrinkage due to drying compared with capillary pore water.

### 6.3.10 Hydration under drying condition

**Figure 6.18** depicts the thermogravimetric analysis of AAS mixtures at age 28 days. A high-intensity endothermic peak between 30 °C and 220 °C is attributed to C-S-H and aluminates decomposition, while the other peak between 275°C -425°C corresponds to hydrotalcite-like phases (Neto et al., 2008). These two peaks can be utilized to estimate the degree of hydration in AAS according to published reports from 2021 (Chen et al., 2021).

Mixtures incorporating 0.3% and 0.6% SAPs exhibited increased total mass loss values up to 220°C when compared to mixtures with the same w/b while without SAPs. For instance, the hydration degree for the C3 mixture increased by 8% when 0.3% SAP was incorporated (SAP3).

At SAP dosage of 0.9%, the hydration degree decreased by 11% compared to the mixture with the same $w_{eff}$/b ratio (C9). Interestingly, it can be noted that under a dry environment, the hydration degree did not increase by the inclusion of a high SAP dosage (i.e., 0.9%) or the free added water (i.e., 0.46). This can be explained by the lower surface quality and anti permeability for mixtures with a high total w/b ratio (Behfarnia & Rostami, 2018). Moreover, increasing the total w/b ratio leads to an increase in the interconnectivity of the pore structure, which leads to higher permeability (Behfarnia & Rostami, 2018; Feng et al., 2004). This reduction in the surface quality suggests that, as one increases the water loss, less water is available for further hydration, which yields a reduction in hydration degree.

This observation implies that internal curing by SAP with a lower dosage of SAP (i.e., 3%-6%) enhances the hydration of AAS, even when exposed to dry conditions.

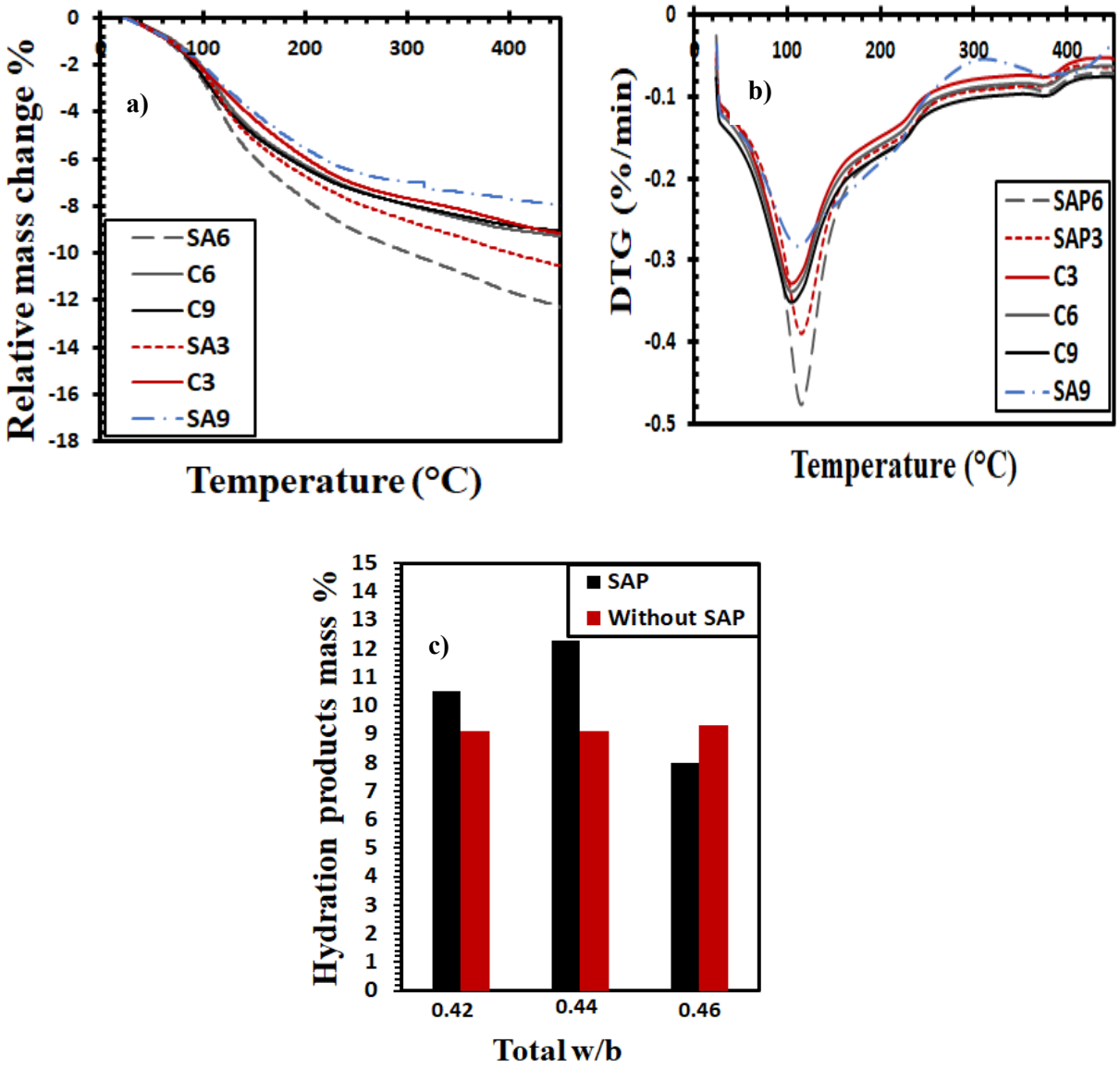


Fig. 6.18. TGA of AAS mortars incorporated with and without SAP; (c) Estimated % of hydration products mass of AAS under drying conditions at 28 d

### 6.3.11 Relationship between pore structure and shrinkage

As has been commonly reported, internal curing by SAP provides evenly distributed reservoirs inside the matrix. Under sealed conditions, internal curing compensated for the chemical and autogenous shrinkage efficiently for AAS mortars. However, as AAS is exposed to drying conditions, the entrained water from SAP will be lost due to drying diminishing the internal

curing effect. For instance, the CF for SAP6 undersealed at 28 days was about 90%, which was dropped to 30% under drying conditions. Hence, it is important to examine the dependence of the shrinkage and mass loss due to evaporation for both internally cured mixes and free added water ones.

**Figure 6.19** presents the shrinkage strain as a function of mass loss. As expected, the total shrinkage had been reduced by SAP addition and occurred over a long period even the mass loss of AAS was high. Hence, it can be stated that water in SAP seems to evaporate easier from larger pores, which is less effective for shrinkage. This also explains the decrease in total shrinkage as SAP dosage increased while exhibiting high mass loss due to water evaporation.

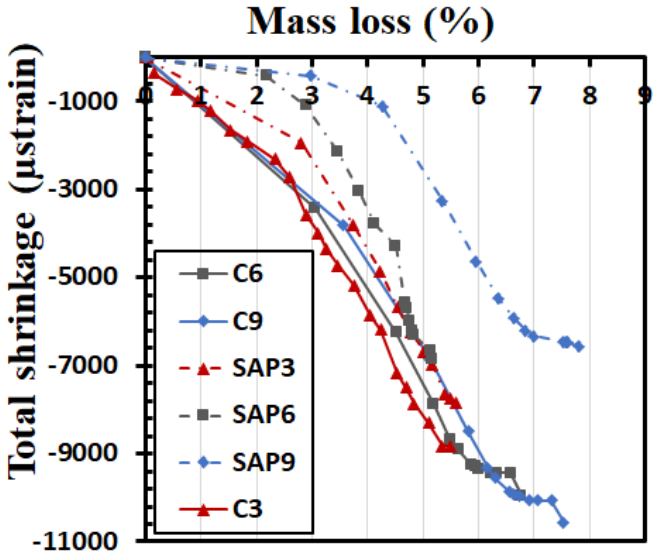


Fig. 6.19. Shrinkage vs mass loss of control and internally cured AAS mixes

Control mixtures showed a steeper slope for the shrinkage-mass loss curve than mixtures without SAPs. The same mass loss in a matrix with finer pores leads to higher shrinkage (Assmann, 2013; Zhutovsky & Kovler, 2013). Hence, for the same mass loss, higher shrinkage took place for mixtures with lower w/b. This is expected since the lower w/b ratio results in finer porosity, which was further confirmed by MIP (Zhutovsky & Kovler, 2017).

AAS mixtures incorporating SAPs exhibited a lower slope for the shrinkage-mass loss curve. Moreover, the slope for SAP3 was steeper than that of SAP6 and SAP9. This indicates that the efficiency of internally cured AAS by SAP in lowering the permeability increases with reducing

SAP dosage. This result agrees very well with the porosity analysis. For instance, the finer porosity and higher degree of hydration of SAP6 compared to SAP9 lead to lower permeability (lower proportion of micro and macropore), which helps to retain the water. Consequently, it can be stated that the SAP6 mixture has more capabilities in controlling the water (i.e., less water effectively lost) which creates more accessible water used for hydration. Hence, the limited ability of further additions of SAP (>0.6%) in enhancing the shrinkage behavior of AAS when exposed to low RH is due to the higher surface porosity and higher permeability.

### 6.3.12 Microstructure evolution

Image analysis of the SAP6 matrix at 7 days shows the formed hydration products layer around the macro voids (white borderline in **Fig. 6.20**). This layer confirms the densification of the AAS matrix due to SAP. This layer will be investigated further by SEM-EDS. The light and dark blue represent the air void and SAP microstructure, respectively. Micro-cracks were detected to emanate from the macro-voids, which indicated a high volumetric strain due to the drying shrinkage. This is confirmed through previously reported shrinkage results, showing about 85% of the total shrinkage of AAS occurred within the first 7 days (Al Makhadmeh & Soliman, 2020; Neto et al., 2008).

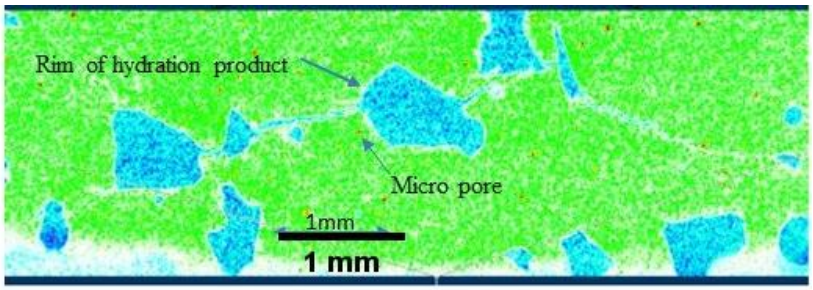


Fig. 6.20. Micro-CT image-based analysis: multi-phase microstructures for SAP6 AAS mix under dry condition

**Figure 6.21** represents SEM on the fracture surfaces of the AAS mixture incorporating SAP at age 28 days. The voids induced by SAP had an irregular shape. The dried SAP particles can be clearly distinguished based on their porous microstructure. **Figure 6.21a** shows the SAP after

being desorbed, which exhibits a curly cottony microstructure. After the desorption of SAP, voids are formed inside the matrix, where this void exhibits a smoothly curvy surface as shown in **Fig 6.21a**. This agrees well with the desorption mechanism of SAP (i.e., inside-out drying process) as demonstrated by the X-ray tomography (**Fig.10**). However, no hydration products were found inside the large void, which can be attributed to the inability of the amorphous C-A-S-H gels (90% of hydration product) to grow in large voids in the AAS system (Li et al., 2020). Nonetheless, at the interface between SAPs void and the AAS paste, a layer of hydration products was formed and detected by EDX (**Fig. 6.22**).

SEM showed evidence of the presence of agglomeration in the AAS pastes whereas **Fig. 6.21b** shows accumulated cottony structure, which indicates that some SAP particles were agglomerated. This agglomeration is attributed to the inadequate dispersion of particles during mixing (Jensen & Hansen, 2001). This agglomeration leads to the formation of large voids (around 1000 μm) which have a direct impact on the strength and pore structure of AAS, especially at high concentrations of SAP (>0.6%).

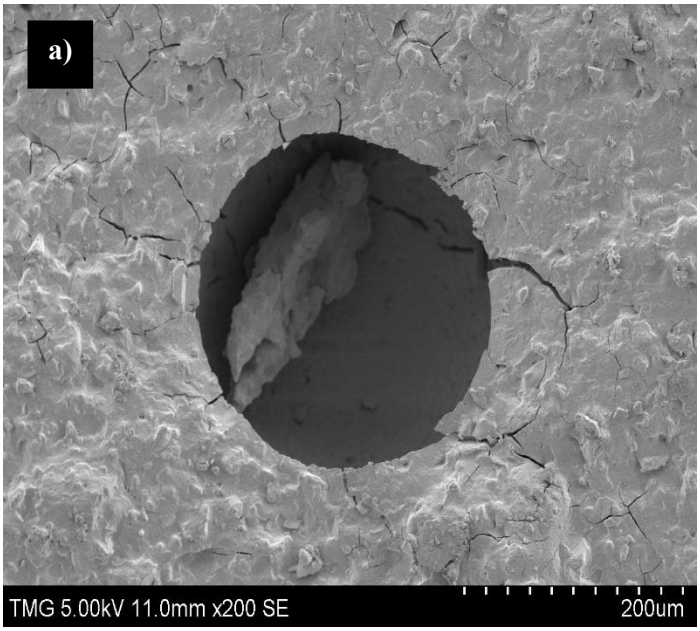

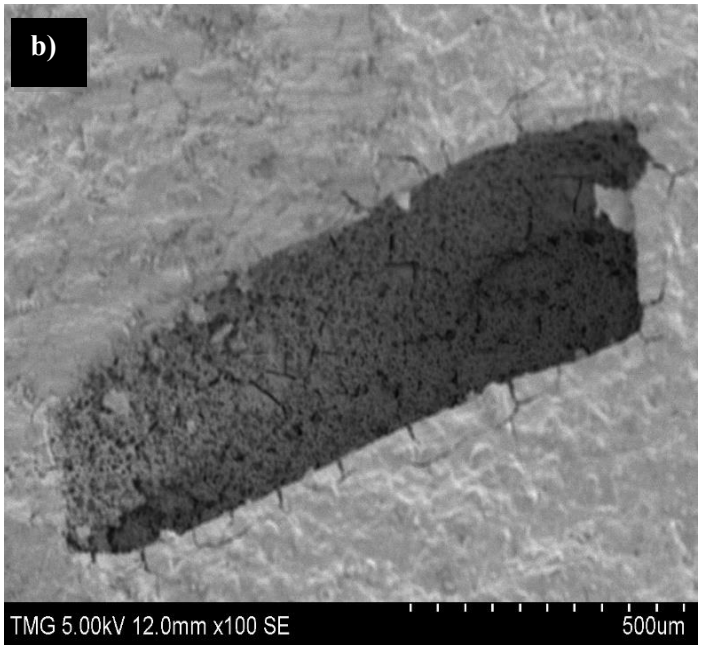
b)
TMG 5.00kV 12.0mm x100 SE
500um

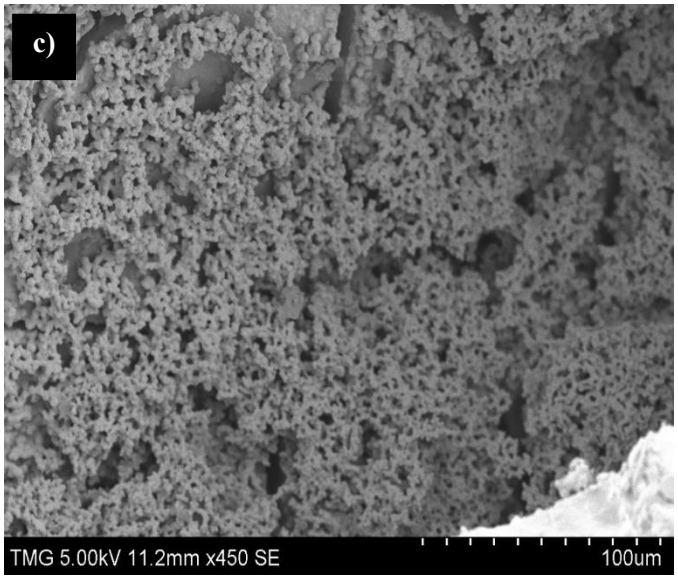
c)
TMG 5.00kV 11.2mm x450 SE
100um

Fig. 6.21. Microstructure after 28 days for AAS paste incorporated SAP presents: (a)SAP void (b) Agglomeration of SAP (Cottony structure of SAP) (c) SAP microstructure

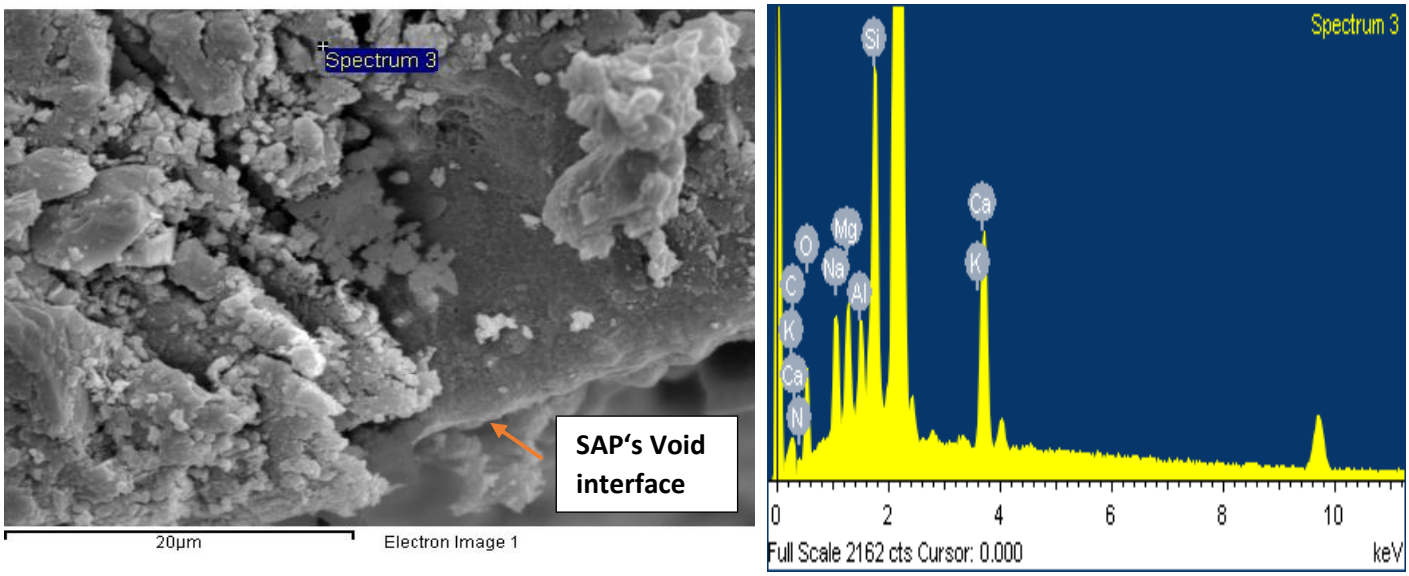


Fig. 6.22. SEM (EDX) analysis for AAS incorporated by SAP

The EDX analysis at the rim of reaction products around SAP was performed on six points, which yielded the following average atomic ratios: Ca/Si:1.06, Al/Si:0.33, Mg/Al:1.3. These findings indicate the formation of C-A-S-H and hydrotalcite, which are the main reaction products in AAS systems (Chen et al., 2021), which are further confirmed by previously published research (Wang & Scrivener, 2003). This gives solid evidence that the efficiency of SAP in mitigating the total shrinkage of AAS when exposed to a dry environment can be related to enhanced water retention performance due to changes in the surface pore structure and increasing the degree of hydration. Furthermore, as shown, SAP showed a significant role in overriding the autogenous shrinkage which contributes to enhanced performance under drying conditions decreased residual shrinkage.

The incorporation of 0.9% of SAP did not show a significant enhancement in AAS properties in terms of mitigating the shrinkage, compressive strength (i.e., decreasing the strength owing to SAP serving as voids), permeability, and the surface quality, Therefore, by considering the impact of including a high dosage of SAPs on the compressive strength, durability, and the limited further enhancing efficiency in mitigating the autogenous and the total shrinkage of internal curing. It can be stated that 0.6% can be the benchmark content of SAPs inclusion in AAS.

## 6.4 Conclusion

- SAP exhibited lower absorption capacity in AAS pore solution due to the charge screening effect of the dissolved ion, mainly the divalent cation $Ca^{2+.}$
- X-ray computed tomography confirms that in AAS incorporated by SAP, the SAPs tend to desorb liquid to the matrix before 5h (i.e., after setting time). A certain quantity of liquid is still stored in the SAP after 7 days of reaction, indicating the further potential for assisting hydration and mitigating the shrinkage at a later age. These findings are contrary to the desorption under dry conditions, where the liquid is completely at 7 days.
- The addition of SAPs to AAS mixtures resulted in 90% reductions in the autogenous shrinkage. SAP postponed the drop of the IRH; however, this effect was more pronounced as the SAP content increased. This is of significant importance in preventing early-age cracking of restraint AAS structures.
- The adverse effect of internal curing by SAPs on the compressive strength can be diminished and minimized especially in AAS made with low to moderate SAP content (0.3%-0.6%).
- The IC water entrained by SAPs and the additional free mixing water differently affected the AAS reaction process, pore structure, and the development of IRH.
- The amount of released liquid from SAPs into the matrix is crucial to the efficient counteraction to shrinkage.

- The efficiency of internally cured AAS by SAP in refining pore structure increases with reducing SAP dosages.
- Internally cured AAS by SAP maintained better self-curing conditions for AAS under drying conditions, were 0.6% of SAP allowed a 26% increase in the degree of hydration under drying conditions herein. Also, an 18% reduction in the surface porosity was achieved.
- The incorporation of a high dosage of SAP (i.e., 0.9%) impacted the properties of AAS. A significant strength loss of 22% was achieved with no further benefit in reducing the shrinkage. Moreover, under poor curing conditions, AAS incorporated by 0.9% SAP adversely affected the hydration degree through an 11% reduction, which led to lower surface quality and higher permeability.
- SAP incorporation improved the overall shrinkage behavior of AAS. This effect should be attributed to the firm alleviation influence of SAP on the autogenous shrinkage, significantly decreasing total shrinkage, improving the pore structure, and changed the evaporation mechanisms which consequently created high internal moisture during drying.
- SAP compensated the effect of the w/b ratio on AAS properties.
- SAPs showed an efficient ability as an internal curing agent in enhancing the engineering performance of AAS and can contribute to its wider practical and environmentally efficient application.

# Chapter 7 - Synergetic effect of SAP and SRA in mitigating the shrinkage of alkali-activated slag binders.

## 7.1 Introduction

As discussed in Chapter 5, shrinkage-reducing admixture is a viable technique in mitigating both drying and autogenous shrinkage. Despite demonstrated effectiveness in mitigating AAS shrinkage, SRA was found to adversely affect early hydration.

Chapter 6 showed that the inclusion of superabsorbent polymer (SAPs) as an internal curing agent preserves a high internal relative humidity inside the AAS matrix, which subsequently reduces the self-desiccation. Thus, the extensive tensile stresses are avoided, thereby decreasing the autogenous shrinkage significantly. Moreover, SAPs addition was found to improve and enhance hydration at a later age due to the internal curing effect.

Both chapters emphasized the high efficiency of the internal curing by SAPs in mitigating autogenous shrinkage, shown through a reduction of 90% for autogenous shrinkage, compared with 46% for SRA. SAPs have also shown a low reduction effect on total drying shrinkage in AAS, having a reduction in total drying shrinkage of 29%. Finally, SRA shows, on average, a reduction in the total shrinkage of around 40-50%.

To optimize the benefits and improve their efficiencies on autogenous and drying shrinkage of AAS, a hybrid mitigation strategy combined with both SRA and SAPs was studied in this chapter. At the date of submission and to the best of the author's knowledge, no previous research regarding the combined effect of SRA and SAPs on the shrinkage behavior of AAS has been published. Therefore, understanding this hybrid mitigation strategy can enhance the shrinkage behavior of AAS and enable determining the optimal designs for a particular application. This work aims to understand the synergetic effect of SAP and SRA on the shrinkage of AAS. The interactions between both mitigation strategies were investigated.

## 7.2 Specific approaches

SRA is an amphiphilic compound that consists of a polar functional group (i.e., hydrophilic head) that is connected to a non-polar hydrocarbon chain (i.e., hydrophobic tail). A potential

hydrophobic interaction between SAPs polymeric networks and the SRA molecule occurs. Therefore, to reveal the possible mutual influence between both admixtures, an analysis of pore solutions of AAS paste was done. To this end, samples were extracted to investigate the possible interaction effects between SAPs and SRA (i.e., swelling capacity for SAPs and surface tension).

SAPs absorption was characterized in various liquids using optical microscope images. The absorption in AAS paste was evaluated by X-ray computed microtomography and microscope. Image J software was used to analyze the results.

Hydration kinetics were studied by isothermal heat flow calorimetry. Moreover, in this study, autogenous, total drying shrinkage tests, and continuous monitoring of internal relative humidity change were performed. The microstructure of optimized AAS pastes was qualitatively described by SEM.

*Mixing procedure*: Initially, the sand and slag were mixed at a low speed for 1 min, then the dry SAPs were added and mixed for 1 min to ensure homogenous distribution. Then, half of the blended solution of waterglass and SRA was added and mixed at low speed for 30 s, after which the remaining amount of solution was added and mixed first at medium speed for 1 min. The mixture characteristics are presented in **Table 7.1.**

Table 7.1 Mixtures of AAS pastes and mortars

| Mix ID | SAP (%) | SRA (%) | Effective w/b | Extra water |
|---|---|---|---|---|
| OPC | 0 | 0 | 0.4 | 0 |
| Control | 0 | 0 | 0.4 | 0 |

| | | | | |
|---|---|---|---|---|
| SAP3 | 0.3 | 0 | 0.4 | 0.02 |
| SAP6 | 0.6 | 0 | 0.4 | 0.04 |
| SRA3 | 0 | 3 | 0.4 | 0 |
| SRA6 | 0 | 6 | 0.4 | 0 |
| S3-0.3 | 0.3 | 3 | 0.4 | 0.02 |
| S6-0.3 | 0.3 | 6 | 0.4 | 0.02 |
| S6-0.6 | 0.6 | 6 | 0.4 | 0.04 |

## 7.3 Results and discussion

### 7.3.1 SAP swelling capacity in various AAS pore solutions

**Figure 7.1** shows the microscopic images of SAPs particles and the visual changes in the volume when mixed with distilled water, extracted pore solutions from AAS mixtures, AAS pore solution with SRA. Additionally, the absorption was also measured when SRA was added after the extraction of the AAS pore solution; in order to distinguish between SRAs effect on SAPs absorption from the SRA influence on the AAS pore solution during slag hydration (i.e., SRA affects the concentrations of the ions as discussed in Chapter 5).

SAPs showed a significantly lower absorption capability in the extracted pore solution compared to that in distilled water, as shown in **Fig. 7.2**(a,b). This reduction in the absorption can be attributed to the charge screening effect induced by the high ion concentrations in the pore solution (Farzanian et al., 2016; Pourjavadi et al., 2013). AAS pore solution exhibits a significat concentration of ions divalent cations (Puertas, Fernández-Jiménez, et al., 2004). Specifically, $Ca^{2+}$ is considered to be an effective binder for carboxylic acid that bridges the negative charges of polymer chains. Previous research has demonstrated that this electrostatic interaction leads to supramolecular systems, which are aligned with a hydrogel shrinkage (Kang et al., 2017; Richter et al., 2008; Schröfl et al., 2012). Furthermore, the interaction of SAPs and $Ca^{2+}$ ions was confirmed in Chapter 6.

SAPs swelling is the highest in the pure AAS pore solution (**Fig. 7.2a**), whilst SAPs absorption was reduced by 42% in the solution with added SRA after extraction when compared to pure AAS pore solution. These results are likely because SRA is an amphiphilic compound that consists of a polar functional group (i.e., hydrophilic head) connected to a non-polar hydrocarbon

chain (i.e., hydrophobic tail) (Zana, 2005). A potential hydrophobic interaction between SAP polymeric networks and the SRA tails occurs, leading to an increase in the SAP's network stiffness (Guzmán et al., 2016; Nylander et al., 2006). This hydrophilic interaction explained the high reduction in the absorption capacity.

Additionally, it is worth noting that the SAPs absorption in the AAS pore solution incorporated SRA reduced by 20% when compared to that in pure AAS pore solution. This behavior can be explained by the following two counteracting effects. On the one hand, the pronounced influence of the hydrophobic interaction between SAPs and SRA leads to a reduction in absorption. On the other hand, the effect resulted from SRA influence on the alkalinity of the pore solution during slag hydration. This effect is mainly related to the decreasing of $Ca^{2+}$ concentration in the pore solution, as confirmed in Chapter 5, which positively reduces the electrostatic interaction and the charge screening effect. Consequently, this puts a finite limit to the absorption reduction.

Moreover, **Table 7.2** shows the pH measurements and confirms that the addition of SRA after the pore solution extraction does not alter the alkalinity, and the influence of SRA on the slag dissolution was avoided. The influence of hydrophobic interactions on absorption is more pronounced in this case.

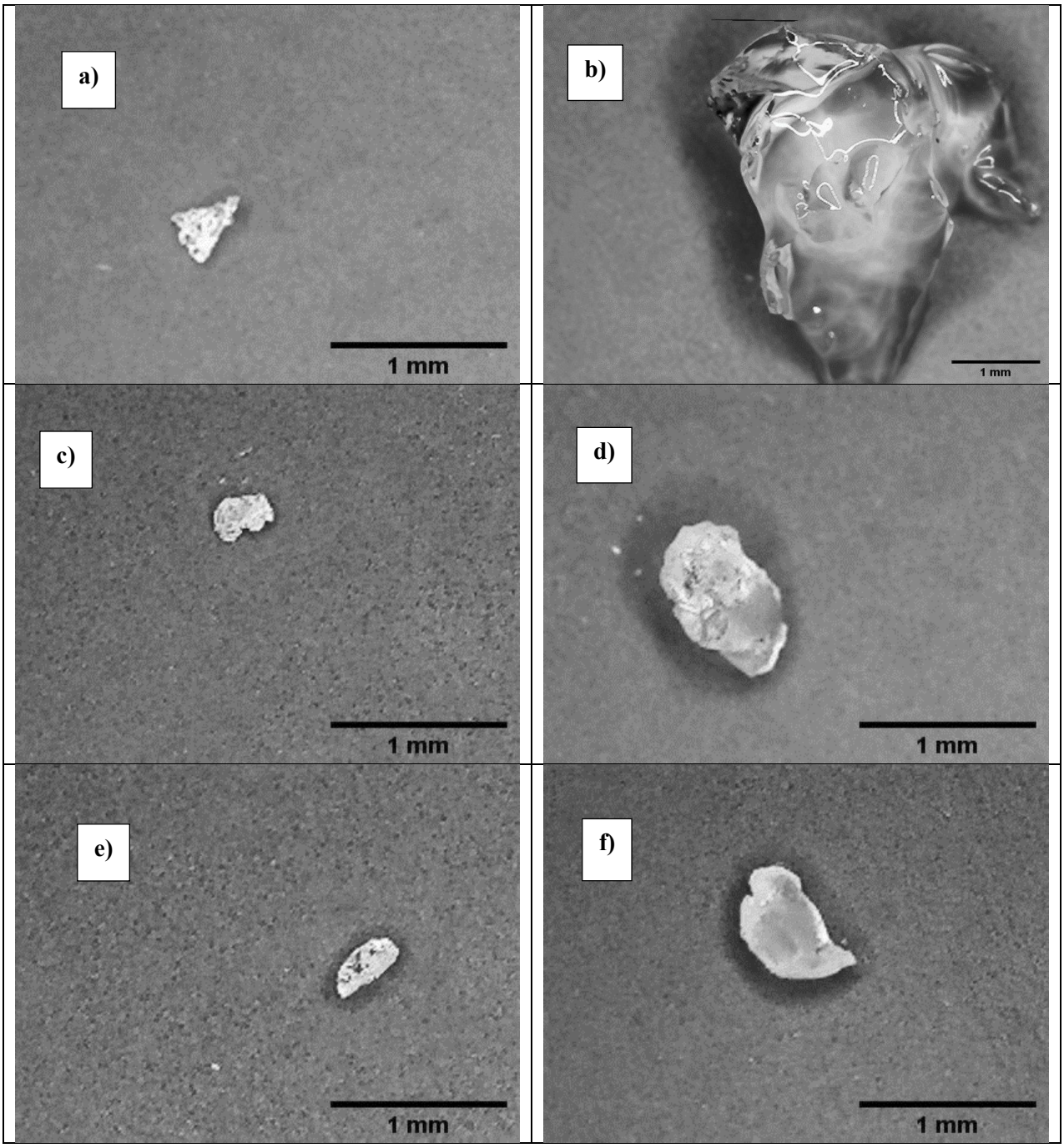

Fig. 7.1. Optical images of dry and absorbed SAP particles in distilled water (a, b) and in the extracted AAS pore solution (c, d).; (e,f) in the extracted pore solution with SRA. All images have the same magnification

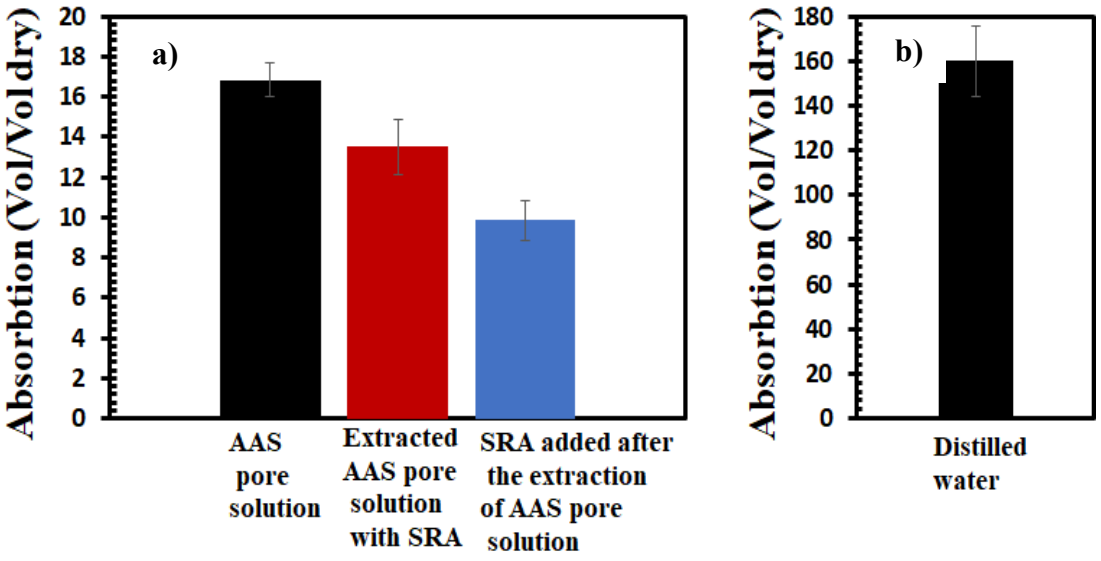


Fig. 7.2. SAPs absorption in pure, with SRA, added SRA AAS pore solution; (b) Absorption in distilled water

Table 7.2 pH measurements of abortion solutions

| AAS pore solutions | pH values |
|---|---|
| Pure pore solution | 13.81 |
| Pore solution incorporated SRA | 13.52 |
| SRA added after extraction to the pore solution | 13.79 |
| Distilled water | 7.60 |

### 7.3.2 Characterization of SAPs absorption in AAS paste

SAPs absorption in AAS paste is shown in **Fig. 7.3** represents the formed macro-voids in the AAS paste containing both only SAPs and paste combined with SAPs and SRA. The representative cross-sections of SAP6 and S6-0.6 AAS pastes obtained by X-ray microtomography, and microscopes images indicate that macro voids notably are larger in AAS paste without SRA.

The areas of macro-voids were measured by ImageJ, and the probability size distribution of these macro voids is illustrated in **Fig. 7.4**. The macro-voids in the hybrid AAS mixture appeared to be

smaller compared to AAS mixtures with SAPs only, with an average macro-void area of 0.9 $mm^2$ and 1.4 $mm^2$, respectively. These values correlate well with the results obtained in **Fig. 7.2**. The results obtained above regarding SAPs absorption sheds light on the possible influence of SRA on the SAPs behavior in AAS paste which should be considered in designing AAS systems combining SRA and SAPs.

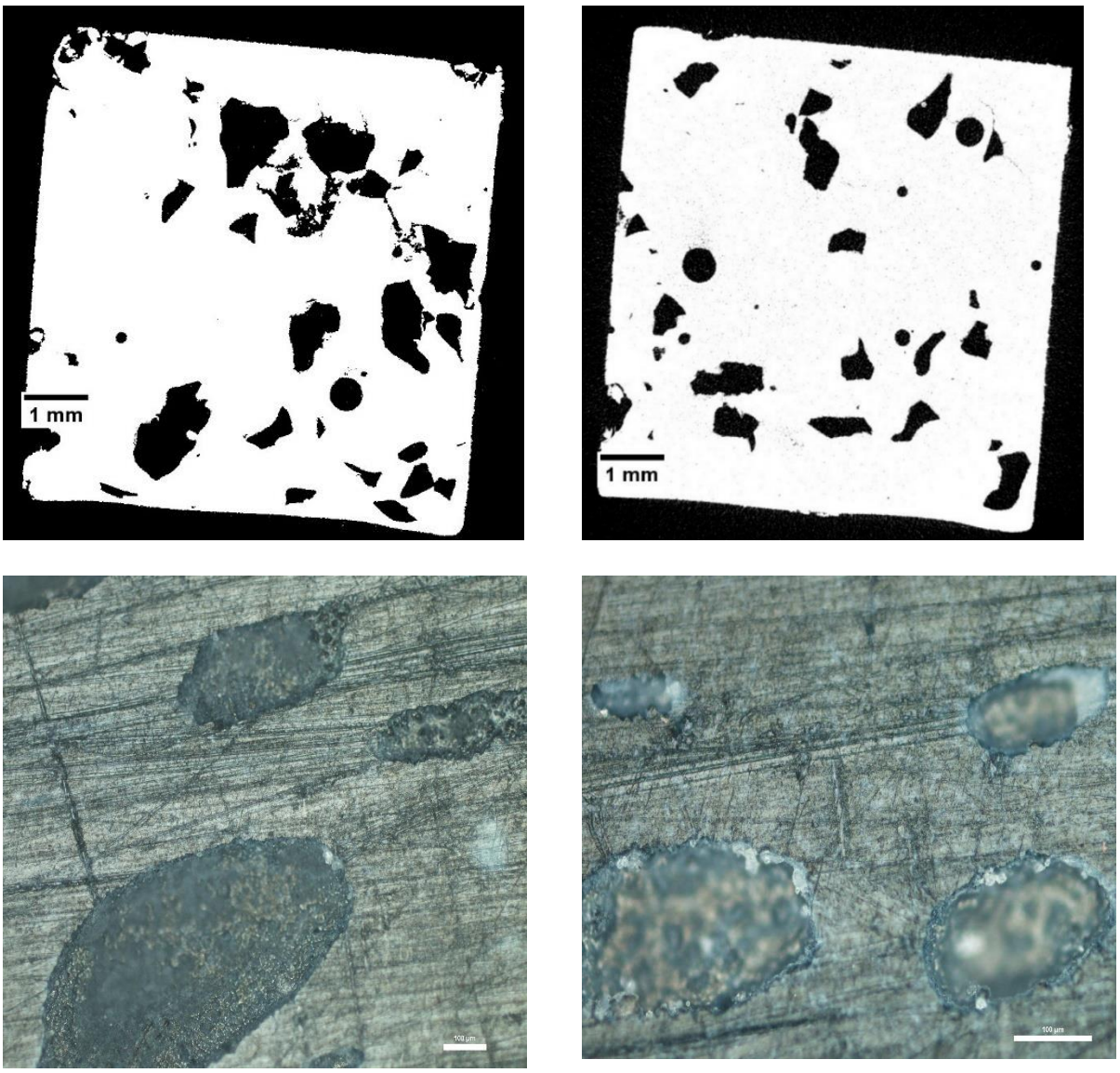


Fig. 7.3. Representative cross-sections of SAP6 (left) and S6-0.6 (right) AAS pastes by X-ray microtomography and microscope, respectively.

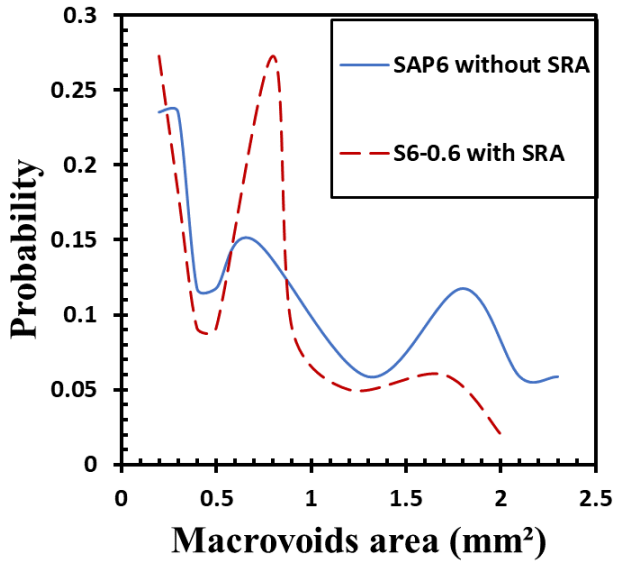


Fig. 7.4. Macrovoids size distribution in AAS paste with and without SRA

### 7.3.3 Surface tension

The surface tension of the pore solution significantly affects the shrinkage development of AAS (Kumarappa et al., 2018). Adding SRA reduces the surface tension of the pore solution leading to a lower shrinkage (Bílek et al., 2018; Kumarappa et al., 2018; Palacios & Puertas, 2007). **Figure 7.5** shows the surface tension for the extracted AAS pore solutions from various mixtures.

Mixtures without SRA exhibited the highest surface tension value (57 mN/m). Surface tension was effectively reduced by around 18% as 3% SRA was added. The higher the SRA dosage, the lower the surface tension. For instance, increasing the dosage from 3% to 6% lowered the surface tension by about 11%. On the other hand, incorporation of SAPs individually showed a negligible effect on the surface tension, whereas SAP6 had almost the same surface tension value as the control.

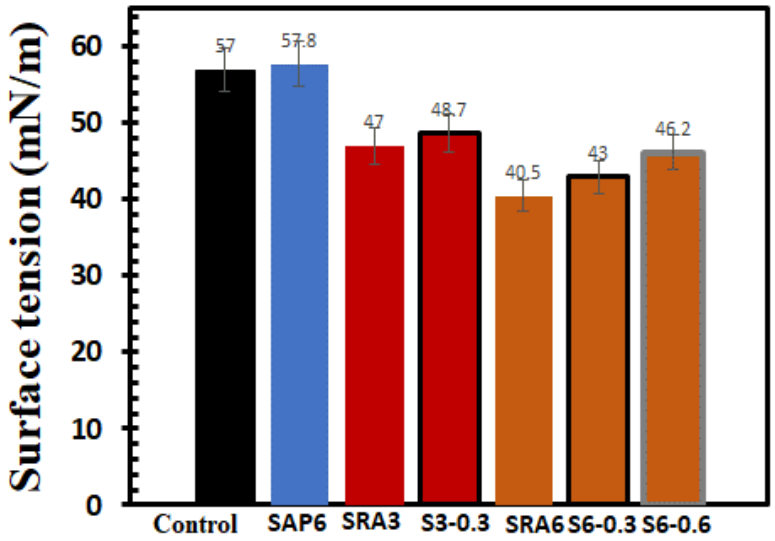


Fig. 7.5 Influence of SRA and SAP on the surface tension of extracted AAS pore solution

The combined system of SRA and SAPs showed another trend. With the same SRA dosage, the surface tension of the AAS pore solution increased by SAP inclusion. The values for S6-0.3 and S6-0.6 were higher by 6% and 14% compared to SRA6, respectively. The inclusion of SAP had decreased the efficiency of SRA in reducing the surface tension. The contributed hydrophobic interactions can explain this hybrid effect of SAP and SRA on the surface tension of the AAS pore solution. **Figure 7.6** shows a schematic that represents the polymer-surfactant system. In individual pore solution systems, SRA reduces the surface tension until a threshold concentration, as discussed in chapter 5. After reaching this CMC, micelles (i.e. surfactant's aggregation) form and limit any further reduction (Rajabipour et al., 2008). In a hybrid system, the polymer chains act as aggregation nuclei because of the strong integrations between (SRA and SAP), yielding to the formation of micelles along with the SAP networks (**Fig. 7.6**).

This behavior can explain the increase in the surface tension as SAPs dosages increased in both mixtures S6-0.3 and S6-0.6. When the SAP content increases, more micelles are formed and adsorbed by SAP chains leading to lower free SRA concentration in the solution, which consequently decreases the SRA efficiency by reducing the surface tension of the AAS pore solution (Guzmán et al., 2016). It can be concluded that the lower the concentration of SAPs, the higher the efficiency of SRA.

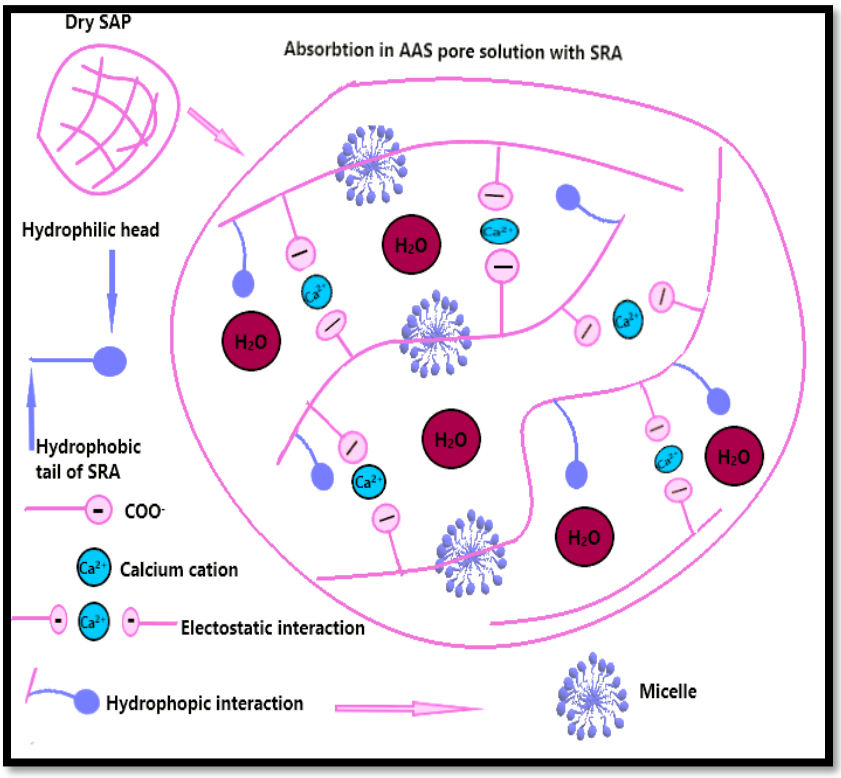


Fig. 7.6 Proposed hypothetical structure of SAP explaining interactions of SAPs in AAS pore solution and with SRA molecules.

### 7.3.4 Autogenous shrinkage and IRH

**Figure 7.7** shows a comparison between SAPs and SRA effect individually and combined on the IRH development. Adding SAPs was more effective in maintaining the IRH at a higher level. As shown in **Fig. 7.7,** AAS mixtures incorporating SRA and SAP showed a slight reduction in the IRH when compared to mixtures with SAP only. For instance, the IRH development curve for the S3-0.3 mixture was below that of the SAP3 mixture and above the curve for SRA3. Thus, it can be stated that the inclusion of SRA has decreased the efficiency of SAP in maintaining high IRH due to their chemical interactions, which reduced the absorption/desorption of SAPs.

The measurements of autogenous shrinkage of AAS mixtures are shown in **Fig. 7.8**. Autogenous shrinkage is directly proportional to the surface tension of the pore fluid and the changes in IRH (Hu et al., 2019). **Figure 7.8a** showed the individual effect of SRA and SAPs on the autogenous shrinkage. Adding SRA at dosages 3% and 6% decreased the autogenous shrinkage at 28 days by

16% and 46%, respectively. This reduction originated from the SRA role in decreasing the surface tension of the pore solution (**Fig. 7.5**) and the slight increase in IRH is because of the delayed hydration (**Fig. 7.7**). SAPs inclusion was more effective in mitigating the autogenous shrinkage of AAS. Adding the SAPs at rates 0.3% and 0.6% caused a reduction of 53% and 90%, respectively. This can be ascribed to the SAP's role in mitigating the IRH drop (**Fig. 7.7**).

Thus, it can be concluded that SAPs were more effective in reducing autogenous shrinkage than SRA. Furthermore, 0.6% of SAPs provided the saturated condition to the matrix and thus, reduced the autogenous shrinkage of AAS to a level less than that in OPC (**Fig. 7.8a**).

**Figure 7.8b** shows the autogenous shrinkage development of AAS mixtures incorporating SAPs and SRA. The combination of SAPs and SRA in AAS enhanced the role of SRA in mitigating the autogenous shrinkage of AAS. This is consistent with OPC-based systems incorporating SRA and SAPs (Wehbe & Ghahremaninezhad, 2017). On the other hand, this hybrid system reduced the efficiency of SAPs in restraining the autogenous shrinkage. As shown in **Fig. 7.8**, the early shrinkage rates development (i.e., 7 days) in AAS incorporated SAP and SRA were higher than that of AAS with SAP only. On the other hand, these hybrid AAS mixtures exhibited lower autogenous shrinkage rate development compared to those in SRA mixtures, suggesting that combining SAPs and SRA promoted higher efficiency of SRA in mitigating the autogenous shrinkage.

AAS mixtures S3-0.3, S6-0.3, and S6-0.6 reduced the autogenous shrinkage by 47%, 53%, and 49%, respectively, compared to the control. Mixtures with the same SAPs content exhibited lower autogenous shrinkage as the SRA increased. This is due to the reduction in the pore solution surface tension (**Fig. 7.5**) combined with the increase in the IRH level (**Fig. 7.7**).

At the same SRA dosage, increasing SAPs content surprisingly exhibited higher autogenous shrinkage. For instance, the S6-0.6 mixture exhibited about 7% more than that of S6-0.3. The inclusion of higher SAPs content had led to a higher pore solution surface tension of the pore fluid (**Fig. 7.5**). Although the IRH was at a higher level in mixture S6-0.6, the autogenous shrinkage was still high. This suggested that the surface tension of the pore solution has a more significant influence on the autogenous shrinkage than the IRH. Therefore, it can be stated that both SAP and SRA counteracted the effect of each other in restraining the autogenous shrinkage. This behavior is attributed to the explained chemical interactions between both. SRA caused a

reduction in the absorption capacity of SAP and affected the SAP's desorption process due to the reduction of the surface tension of the pore's fluid, yielding to lower capillary force, which decreases the desorption of SAP (Buchholz and Graham, 1998). Simultaneously, SAP inclusion leads to an increase in the surface tension due to the hydrophobic interaction between SRA molecules and SAP networks (**Fig. 7.6**). Consequently, the inclusion of a lower SAP dosage is more beneficial when combined with SRA in AAS systems.

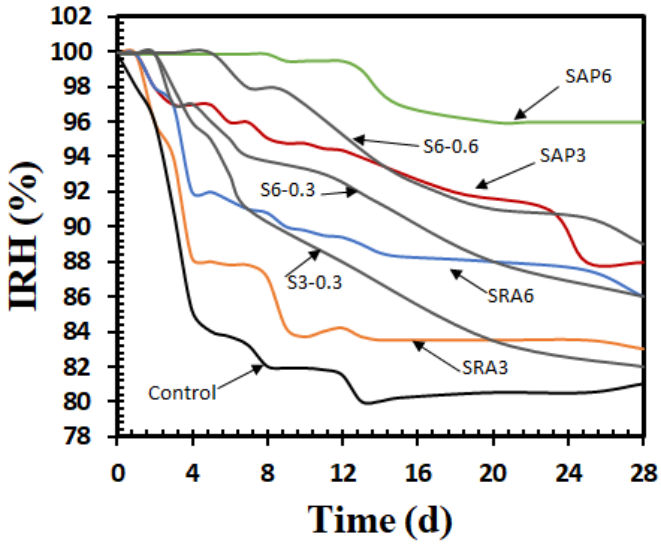


Fig. 7.7 Internal relative development in AAS mortars incorporated with SAP and/or SRA

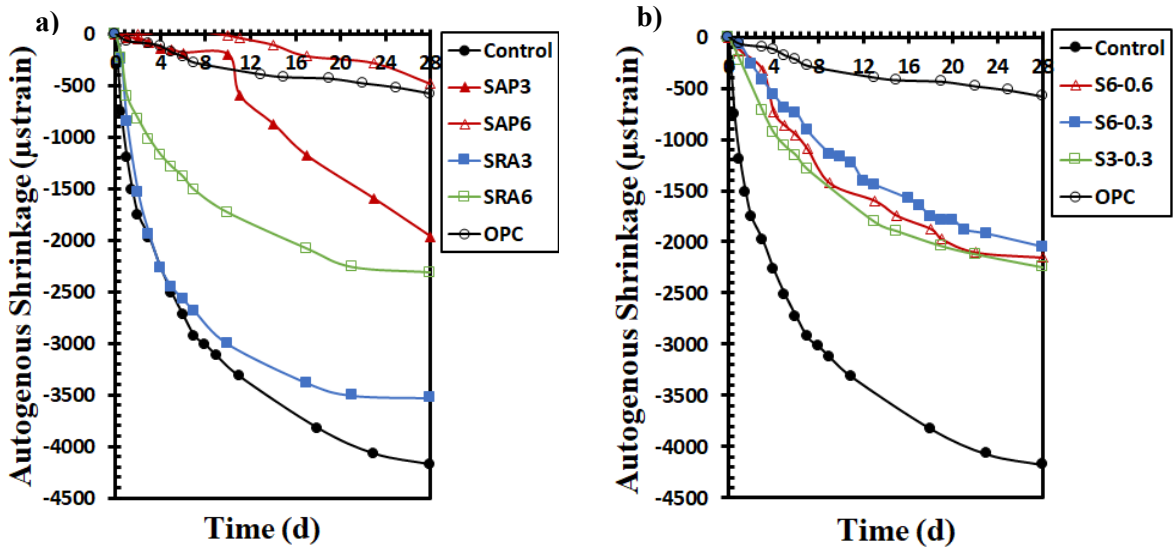


Fig. 7.8. The autogenous shrinkage of AAS (a) Individual usage of SAP and SRA; (b) Hybrid system

### 7.3.5 Total drying shrinkage

**Figure 7.9** illustrates the total shrinkage evolution for AAS specimens. The total shrinkage of the control AAS mixture was very high and reached about -9300μ strain. Adding SRA and SAP had significantly affected the total shrinkage development. For instance, adding 3% and 6% SRA had reduced the total shrinkage by about 30% and 41% compared to the control mixture at age 28 days, respectively.

This significant reduction is mainly attributed to the efficiency of SRA in reducing the surface tension yielding to lower capillary stresses (i.e. Laplace law) on the solid skeleton (Kumarappa et al., 2018). Adding 6% SRA reduced the surface tension of AAS pore solution by 29%, as discussed in **Fig. 7**.5. Furthermore, the inclusion of SRA promoted higher hydrotalcite-like phase formation in hydration products which are voluminous crystals that can compensate for the shrinkage, as proved in chapter 5.

Interestingly, the incorporation of SAPs showed a beneficial effect on the total drying shrinkage of AAS. Internal curing by SAP provides evenly distributed reservoirs inside the matrix (Oh & Choi, 2018). Under sealed conditions, internal curing compensated the autogenous shrinkage of AAS mortars efficiently (Song et al., 2016). Mixtures incorporating 0.3% and 0.6% SAP showed a reduction in shrinkage with about 15% and 29%, respectively, compared to the control. However, the role of SAPs in mitigating the total drying shrinkage was less effective than that of SRA.

**Figure. 7.9b** shows the influence of the hybrid system of SRA and SAPs. AAS incorporating both SRA and SAP showed the lowest shrinkage compared to other mixtures. For instance, mixture S6-0.3 showed the lowest shrinkage value of -2980 μ strain. However, by increasing SAPs content to 0.6% at constant SRA content, a reduced shrinkage reduction efficiency was achieved. This can be explained by the higher degree of hydrophobic interaction that influences the free concentration of SRA in the AAS pore solution, which subsequently affects the main role of SRA in reducing the surface tension yielding higher shrinkage, as discussed above. On the other hand, at constant SAPs content, increasing SRA resulted in a lower shrinkage reduction. Nonetheless, the improvement in the shrinkage performance of AAS was more

remarkable for mixtures incorporating higher SRA and lower SAP. These results are consistent with the results of autogenous shrinkage.

Hence, it can be stated that the hybrid mitigation technique was efficient in AAS, reaching the same shrinkage level as that in OPC. Mixture S6-0.3 exhibited a shrinkage value of -2980 µstrain compared with -2750 µstrain for the OPC mixture. This observed shrinkage behavior is significant in the use of such a hybrid system in mitigating the substantial shrinkage in AAS.

As confirmed that each mitigation strategy of SAPs and SRA showed different mechanisms in mitigating the shrinkage of AAS, combing both mechanisms successfully led to enhancing shrinkage behavior of AAS shrinkage. This enhancement originates from the fact that both factors of IRH and the surface tension were kept at a suitable level in the hybrid AAS system, and the enhanced formation of hydrotalcite-like phases in the presence of SRA decreased the amount of shrinkage. However, it should be considered that the potential interaction of SAP and SRA and their combined influence on mitigation of the shrinkage of AAS mainly depends on the concentration of each constituent.

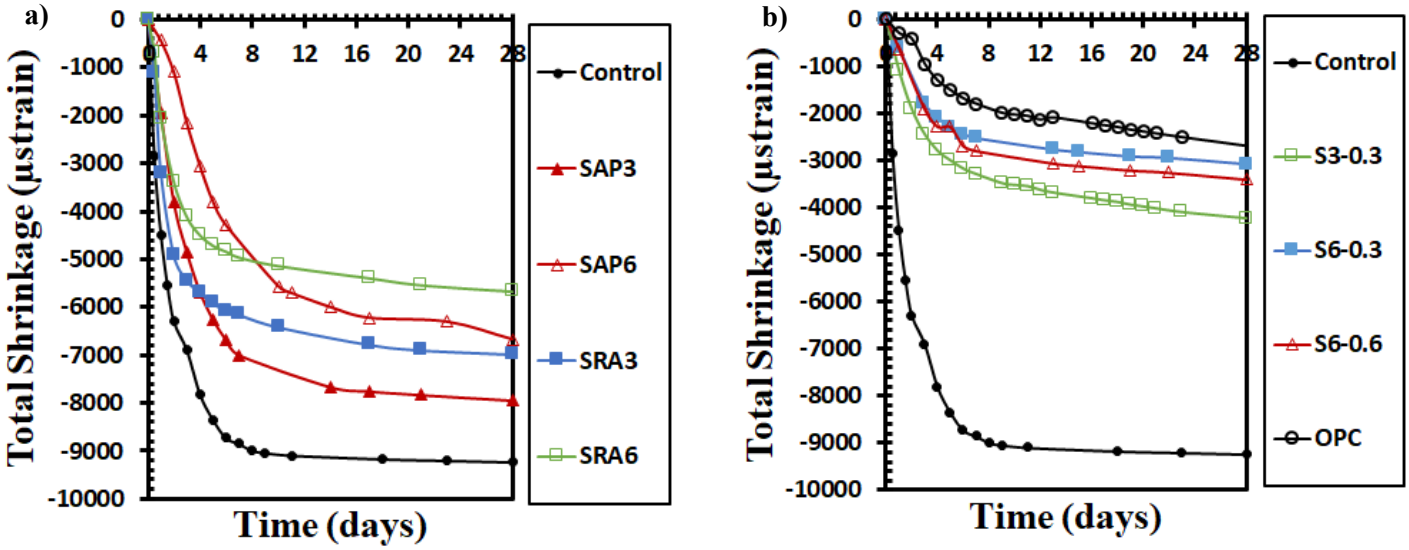


Fig. 7.9. The total drying shrinkage of AAS (a) Individual usage of SAP and SRA; (b) Hybrid system

### 7.3.6 Heat evolution results

The heat flow rates of AAS mixtures with individual and combined SAP and SRA mixtures are presented in **Fig. 7.10**. As observed, the rate of hydration is significantly lower when SRA is

added. The time to reach the peak (TTRP) is extended by increasing the SRA dosage, as can be seen in SRA3 and SRA6 mixtures. This retardation is attributed to the fact that SRA reduces the pore solution's alkalinity by lowering the concentration of dissolved ions in the pore solution, as explained in Chapter 5. Furthermore, a reduction in the hydration peak and a slight delay in its occurrence is induced by SAP inclusion. This can be explained by (1) the slow liquid releasing rate to the matrix is entrained by SAP, or in other words, the stored liquid inside SAPs is not directly available for the reaction, and (2) as shown in Chapter 6, some $Ca^{2+}$ alkali ions, which are dissolved from slag, are likely used up by SAPs**.** This causes a reduction in the concentration in the pore solution that affects the reaching of the critical Ca/Si ratio that contributes to C-A-S-H gels formation. Thus, a lower amplitude of the acceleration peak is noticed with increasing SAP content.

The hybrid system showed a reduction in hydration peak and a significant extension of TTRP. **Table 7.3** represents a comparison of calorimetric results obtained for the individual and hybrid systems of AAS. The total heat released from AAS paste up to age 3 and 7 days was used to estimate the relative hydration degree (i.e., rel.$\alpha_{hyd\_3D}$ and rel.$\alpha_{hyd\_7D}$). The relative hydration degrees were normalized to the control mixture. All hybrid AAS mixtures showed a significant reduction in the 3 days relative hydration degree, with results up to a 28% reduction. This indicated that the retardation effect of the hybrid system was more pronounced than that caused by the individual addition of SRA or SAPs.

Moreover, increasing the SRA dosage in the hybrid system combined with SAPs led to a significant retardation effect. For instance, the TTRP for S3-0.3 and S6-0.3 mixtures was 37.6h and 46.9h, respectively. This can be attributed to the reduced desorption of SAPs that depends on the surface tension of the liquid and the corresponding capillary pressure (Buchholz and Graham, 1998). Thereby, the reduction in the surface tension induced by increasing SRA dosage decreased the capillary pressure. Consequently, this affects the desorption of SAPs, leading to a slower hydration rate. However, more research is needed to understand the desorption process of SAPs when combined with SRA in AAS systems.

Nevertheless, as the hydration reaches the age of 7 days, this effect on the hydration decreased, where the achieved rel.$\alpha_{hyd\_7D}$ was comparable to that of the control mixture (**Table 7.3**).

However, there was a higher rel.$\alpha_{hyd\_7D}$ for mixture S6-0.6 when compared to S6-0.3, which is most probably attributed to the internal curing effect of SAP.

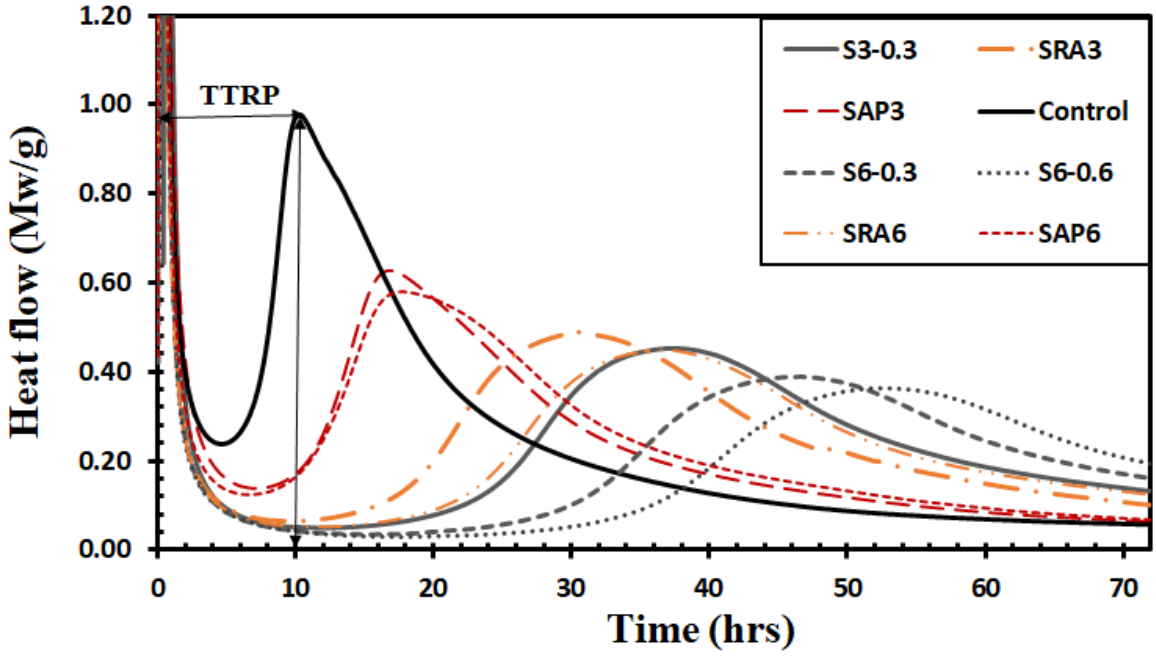


Fig. 7.10. The heat of hydration curves of AAS pastes

Table 7.3 Summary of influence of SAP and SRA on TTRP and relative hydration degree of AAS pastes

| Mixture ID | TTRP | rel.$\alpha_{hyd\ 3D}$ | rel.$\alpha_{hyd\ 7D}$ |
|---|---|---|---|
| Control | 11.3 | - | - |
| SRA3 | 30.1 | 0.97 | 1.03 |
| SRA6 | 36.5 | 0.92 | 1.02 |
| SAP3 | 16.3 | 0.91 | 0.94 |
| SAP6 | 17.6 | 0.93 | 0.95 |
| S3-0.3 | 37.6 | 0.87 | 0.99 |
| S6-0.3 | 46.9 | 0.76 | 0.94 |
| S6-0.6 | 53.8 | 0.72 | 0.98 |

### 7.3.7 Compressive strength

The compressive strength at the age of 3, 7, and 28 days for AAS are presented in **Fig. 7.11.** The hybrid system exhibited low 3 days strength. Moreover, increasing either SRA or SAPs content led to lower values. For instance, mixture S6-0.3 gained around 18 MPa, which can be attributed

to the lower relative hydration degree at 3 days as shown in **Table. 7.3**. The 7 days strength followed the same trend. This decrease in the strength can be ascribed to the delayed densification for the AAS microstructure, due to the SRA addition. This is contrary to mixture S3-0.3, which has a lower SRA and SAP, which showed a 7-day strength similar to that in the SAP3 mixture. This can be explained by the faster reaction kinetics for S3-0.3 when compared with the other hybrid mixtures (**Fig. 7.11**).

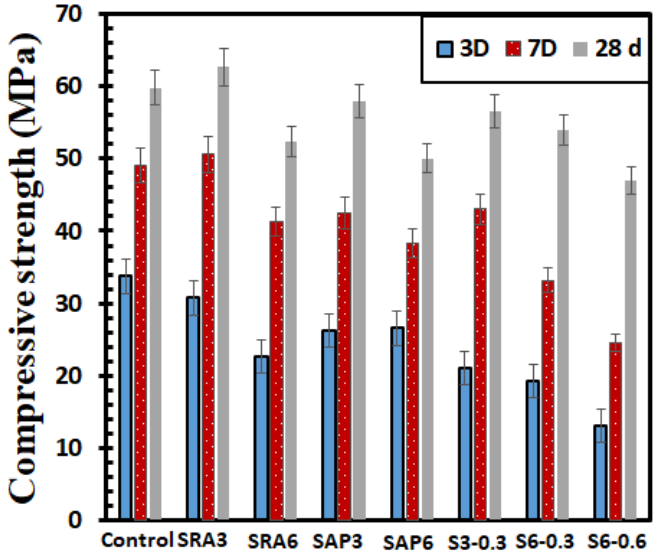


Fig. 7.11. Effect of individual and combined inclusion of SAP and SRA on AAS mortars

**Figure 7.12** compares the 28 compressive strengths of AAS mixtures. All results have been normalized to the compressive strength of the control mixture. The compressive strength for all AAS mixtures showed a reduction except SRA3, which almost exhibited the same strength as the control. Further increasing the SRA dosage to 6% caused a 13% reduction in strength. This can be attributed to the increase of pores proportion with diameters ranges from 1.0 to 0.1 μm (Palacios & Puertas, 2007).

Furthermore, internal curing by 0.3% SAP also showed a negligible effect on the compressive strength. This can be ascribed to the enhanced in AAS hydration compensating voids originated from SAP, as explained in Chapter 6. A concentration of 0.6% of SAP significantly decreased the strength by 16%. The hybrid mixtures exhibited high 28-compressive strength, overcoming the early age low strength. Moreover, the reduction in the strength induced by the increased

dosage SRA addition was less severe in hybrid mixtures. For instance, increasing SRA from 3% to 6% reduced the strength by18% as compared to 4% in hybrid mixtures at constant SAPs (i.e., 0.3%). This could be attributed to the counterbalance effect of macro-voids formation which outweighs potential hydration improvements due to the internal curing effect. Additionally, the less formed macro voids induced by SAP in the hybrid system compared with individual usage of SAP can contribute to this enhancement. Therefore, the interaction between both SAPs and SRA compensated for the adverse effect of individual increment of their dosages on the 28-compressive strength. Nonetheless, mixture S6-0.6 mixture (i.e., highest dosages from both SRA and SAPs) showed a 21% reduction in the strength, despite the lower average sizes of generated SAPs voids in the hybrid AAS system (**Figs. 7.3 and 7.4**). This reduction is attributed to the delay in microstructure densification and a higher proportion of micro-pores (Palacios & Puertas, 2007).

Considering the effect of the hybrid system on the shrinkage and the compressive strength, the usage of the hybrid system in AAS with lower SAP content was showed significant benefits.

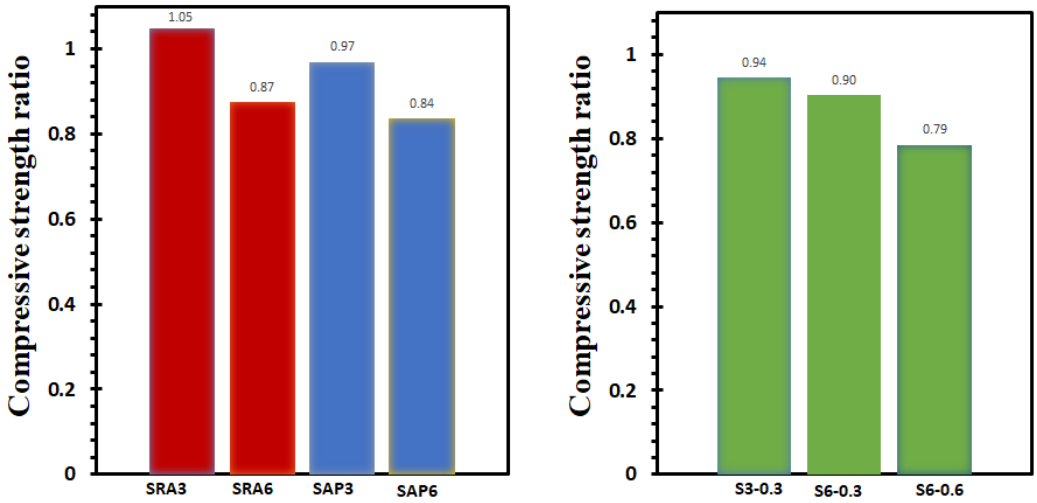


Fig. 7.12. Effect of SRA and SAP on the 28- compressive strength (Normalized to the control AAS)

### 7.3.8 Scanning electron microscopy

**Figure 7.13** presents micrographs of the optimized combination of SAP and SRA (6% SRA and 0.3% SAP). Based on the shrinkage measurements, AAS activated without either SRA or SAPs exhibited significant shrinkage (i.e. -4150με). This high tension leads to micro-cracks that propagate through the matrix and reaction products (**Fig.7.13a)**. However, for the optimum mixture S6-0.3, autogenous shrinkage was around 53% lower than the control mixture was achieved. Thus, the matrix experienced a lower tension, decreasing the intensity and micro-cracks formation in the AAS matrix (**Fig.7.13b**).

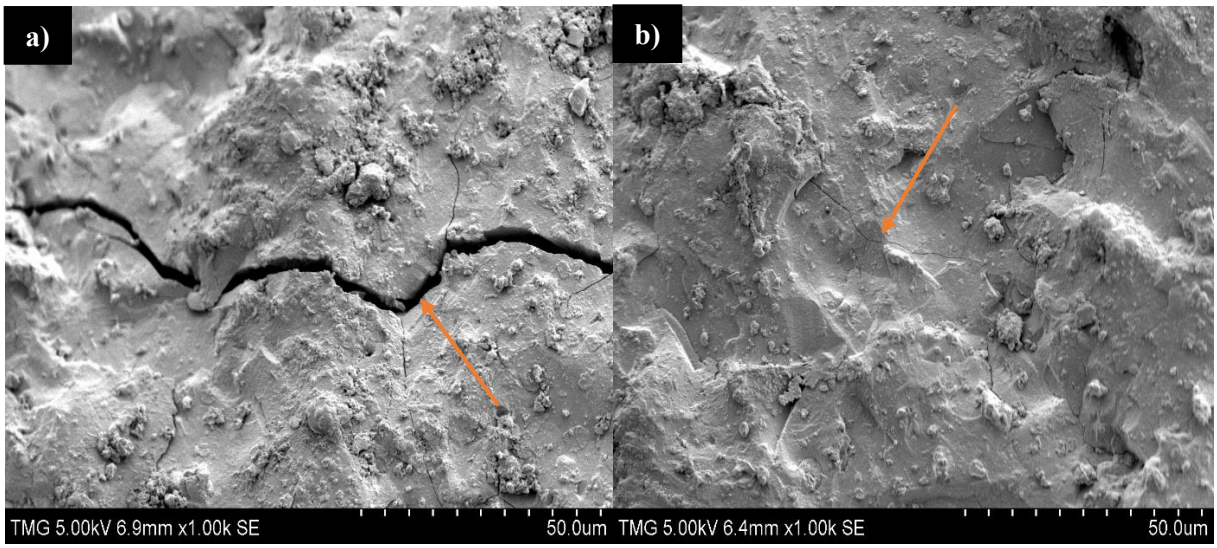


Fig. 7.13 SEM images show the effect of an optimized mixture combining SAPs and SRA on shrinkage micro-cracking of AAS.

## 7.4 Conclusion:

- The hydrophobic interaction between SAPs and SRA has dual effects including (1) decreasing the absorption/desorption capacity of SAP, and (2) increasing the surface the surface tension of the pore solution.
- The addition of SRA decreased the efficiency of SAPs in maintaining high IRH, yielding lower efficiency in mitigating the autogenous shrinkage in AAS.
- The hybrid system was found to have lower autogenous shrinkage compared with individual addition of SRA, due to the counteracting effects of SAP and SRA, which kept the surface tension and the IRH at a suitable level.
- Individually, the inclusion of SAPs was more effective in mitigating autogenous shrinkage than SRA with a reduction of 90% compared with 46% for SRA.
- Individually, the addition of SRA showed higher efficiency than SAPs in mitigating the total drying shrinkage in AAS with a reduction of 41% and 29%, respectively.
- The hybrid system significantly mitigated the total drying shrinkage of AAS. The inclusion of 6% SRA and 0.3% SAP showed the highest shrinkage reduction, with results up to a 69% reduction.
- The hybrid system in AAS led to a pronounced retardation effect on AAS hydration compared with the individual inclusion of either SAPs or SRA. Based on the findings of Chapters 5, Chapter 6, and this Chapter, the pronounced early retardation behavior of the hybrid system on AAS hydration can be attributed to: (1) the influence of SRA on the alkalinity of the AAS pore solution and the depletion in the concentration of dissolved ions (Chapter 5), (2) the slow desorption of liquid entrained by SAP (Chapter 4), (3) the additional crosslinking interaction between SAPs and $Ca^{2+}$ ions (Chapter 4), and (4) SRAs reduction effect in the capillary pressure that leads to a decrease in SAP's desorption capabilities (Chapter 5).
- The hybrid system showed an adverse effect on the early compressive strength due to the lower hydration degree at 3 days. However, the late strength increased due to the internal curing effect of SAP.
- The combination of both SAPs and SRA compensated for the adverse effect of individual increasing content on the 28- compressive strength.

- The most important aim of this work was to test if shrinkage of AAS can be efficiently reduced reaching that in OPC while keeping the high strength. This goal was achieved by preparing AAS combined with SRA and low content of SAP (0.3%).

# Chapter 8 Conclusions, Contributions, and Future works

## 8.1 Overall conclusions

This dissertation investigated and tested multiple techniques to counteract the shrinkage of AAS. Through these investigations, a practical and comprehensive understanding of the roles of each strategy in the AAS system was obtained, mainly focusing on:

- The behavior and working mechanisms of each mitigation technique, as well as their combined interactions and efficacy, in AAS, and
- The corresponding physical impact on shrinkage.

The main concluding remarks for each area are presented in individual subsections.

### 8.1.1 Interactions of SRA in AAS

The impact of SRA based on its nature on AAS hydration was extensively investigated. A step further was taken to relate its impact on the autogenous shrinkage of AAS. The main findings of chapter 5 are presented as follow:

- The addition of SRA led to a retardation effect on AAS hydration which is proportional to SRA dosage. The liquid phase analysis revealed that the presence of SRA impacted the soluble amount of ionic species, reduced the alkalinity of AAS pore solution, and directly impacted the alkaline activation rate and strength development. This investigated behavior adversely influenced the early ages compressive strength, due to the explained reduction in the reaction rate by isothermal conductivity and TGA. However, high dosages of SRA had a negative impact on the later compressive strength which caused a reduction by about 11%, due to the effect of interactions between SRA and the AAS pore solution.
- The characterization of calcium silicate hydrate in AAS by $^{29}$Si MAS NMR shows that the presence f SRA contributed to a reduction in Si $Q^2$ units in the C-S-H gel, indicating a shorter linear chain and a slight reduction in Al/Si ratio in the gel structure. The lower polymerization degree of C-A-S-H gels of SRA mixtures indicates that the Si chains in SRA mixtures experience less intense C-A-S-H syneresis (i.e., contraction of silicate gel's structure) during the polymerization process, which subsequently decreases the autogenous shrinkage.

- The larger volume of hydrotalcite-like phase crystals and lower amounts of C-A-S-H were detected in AAS mixtures containing SRA. This is proportional to the SRA dosage as confirmed by TGA, XRD, and SEM-EDX analysis. This is an important result as the enhanced formation of such crystals contributes to restraining the deformation of C-A-S-H upon drying yielding lower shrinkage.

  Moreover, the enhanced formation of the hydrotalcite-like phase can be invoked to explain the reduction of ions concentration of the pore solution containing SRA.
- The results from BET analysis indicate that SRA influences the pore structure of AAS pastes mainly by reducing the gel porosity, which is directly linked to the C-A-S-H formation rather than the modification of the capillary pore structure.
- The influences of SRA on surface tension, hydration rate, formation of C-A-S-H, and IRH dominate the resultant AAS's shrinkage.

### 8.1.2 The role of superabsorbent polymer in AAS

- SAPs showed a successful long-term inhibition of self-desiccation if the amount of desorbed liquid satisfies the amount of chemical and autogenous shrinkage at a maximum degree of reaction. The efficiency of SAPs in mitigating the autogenous reached 90% at 28 days.
- Desorption kinetics of SAPs (i.e., amount and time of releasing) is crucial as it influences the efficiency to counteract the shrinkage. X-ray computed tomography confirms that, in AAS incorporated by SAP, SAPs tend to desorb liquid to the matrix before 5h (i.e., after setting time). A certain quantity of liquid is still stored in the SAP after 7 days of reaction, which indicates the further potential for assisting hydration and mitigating the shrinkage at a later age. Contrary to the desorption under dry conditions where the SAP's liquid is completely lost after the first 7 days,
- The liquid supplied by SAPs influenced the AAS reaction process, pore structure, and the development of IRH. The degree of hydration and porosity of control mixtures at 7 days shows somewhat higher values.
- SAP incorporation improved the overall shrinkage behavior of AAS and the reduction efficiency reached up to 30% at 28 days. This effect should be attributed to the firm alleviation influence of SAP on the autogenous shrinkage, significantly reduced the total

shrinkage, improved the pore structure, and changed the evaporation mechanism which consequently created high internal moisture during drying.

- SEM showed evidence that SAP-originated cavities in AAS paste are free of reaction products which are unlike that in the OPC system where portlandite formation was detected within the SAP voids. Moreover, the presence of agglomeration was detected by SEM images; this agglomeration leads to the formation of large voids (around 1000 μm) which have a direct impact on the strength. This agglomeration is attributed to the inadequate dispersion of particles during mixing, showing that care should be taken when a high content of SAPs (i.e., > 0.6%) is used.
- The adverse effect of internal curing by SAP on the 28-compressive strength can be diminished and minimized especially in AAS made with low to moderate SAP content (0.3%-0.6%). Compared to control AAS mixtures with the same total w/b ratio, AAS internally cured by SAPs exhibited slightly higher strength values. This positive effect is more obvious in the case of AAS prepared at a low w/b ratio.
- Internal curing by SAPs yielded better AAS performance in terms of shrinkage reduction, assisting the hydration degree, enhancing the surface quality, and anti-permeability compared to control mixtures. Nevertheless, incorporation of high SAPs contents (i.e., >0.6%), adversely affected the properties of AAS.

### 8.1.3 The hybrid system of SRA and SAP

Based on the experimental analysis, SAP was efficient in mitigating the autogenous shrinkage by up to 90%, while also indicating a ~30% lower efficiency in reducing the total drying shrinkage. Interestingly, SRA exhibited a 46% lower efficiency in reducing the autogenous shrinkage compared to that of SAP but showed a 41% reduction in the total drying shrinkage of AAS. Therefore, to combine these effects, a hybrid system of AAS incorporated SAP and SRA was examined. The synergetic effect of SAPs and SRA in AAS pates and mortars was investigated to optimize the benefits and improve their influence on shrinkage reduction efficiency. The main findings of this chapter are:

- The addition of SRA adversely influenced the absorption capacity of SAPs, whilst SAPs affected the SRA efficiency and contributed to increasing the surface tension values.

These observed behaviors are attributed to the potential hydrophobic interaction between SAPs polymeric networks and the SRA tails.

- The addition of SRA decreased the efficiency of SAPs in mitigating the autogenous shrinkage in AAS, due to the lower absorption/desorption of SAPs in the presence of SRA. On the other hand, the hybrid system was found to have lower autogenous shrinkage when compared with individual addition of SRA, due to the counteracting effect of SAP and SRA which kept the surface tension and the IRH at a suitable level.
- The hybrid system of the two mitigation techniques was efficient in AAS and mitigated the total drying shrinkage reaching levels shown in OPC. This observed shrinkage behavior is significant in the use of this hybrid system for mitigating the substantial shrinkage in AAS. The hybrid system of SRA and SAP also showed a better effect on the mitigation of the total drying shrinkage than the individual usage of SRA or SAP. This effect is attributed to the comprehensive influence of both the surface tension and IRH and the enhanced formation of hydrotalcite-like phases in the presence of SRA.
- A pronounced and proportional retardation behavior was observed for the hybrid system application of SAP and SRA when both effects are accumulated and combined. Based on the findings of Chapter 5, Chapter 6, and this Chapter, this retardation can be attributed to: (1) the influence of SRA on the alkalinity of AAS pore solution, which affects the concentrations of the ions as discussed in chapter 5, (2) the slow desorption of the liquid entrained by SAP where the SRA reduction effect on the capillary pressure leads to a decrease in SAPs desorption, and (3) the additional crosslinking interaction between SAPs and $Ca^{2+}$ ions (Chapter 4).
- The hybrid system showed an adverse effect on the 3-day compressive strength, and this effect becomes more significant by incorporating higher concentrations of both SRA and SAP. However, the 28-compressive strength increased due to the internal curing effect of SAP.
- Considering the detrimental effect of the hybrid system on the shrinkage and the compressive strength, the usage of the hybrid system in AAS with lower SAPs content was showed significant benefits.

- The inclusion of a lower concentration SAPs dosage is more beneficial when combined with SRA in AAS systems. This observation is of crucial importance in alleviating the high shrinkage cracking in AAS systems.

## 8.2 Contribution:

1. Through this thesis, the interactions of SRA and the pore fluid of AAS are better understood in chapter 5. The main contribution can be summarized as follow:

- This research provided important information concerning the behavior of SRA in AAS pore solutions. It was found from monitoring the surface tension of the AAS pore solution, that at a specific concentration, SRA efficiency is stopped due to micelles formation. However, CMC was identified in AAS which put a limit for further SRA efficiency and shrinkage reduction. This finding has an especially important practical implication.
- Another main contribution came from the chemical analysis of the extracted AAS pore solution which shed light on the retardation source of AAS activation containing SRA. The presence of SRA impacted the soluble amount of ionic species, reduced the alkalinity of AAS pore solution, directly impacted the alkaline activation rate strength development, and delayed the setting time.
- The investigation of phase assemblage of AAS modified with SRA unraveled another contribution. The extensive phase analysis showed that the presence of SRA led to a high rate of Hydrotalcite formation in a crystal phase ($Mg_6Al_2$. $CO_3(OH)_{16}\times 4H_2O$) consumed the Al and Mg ions. This can explain the source of the significant decline of Al and Mg ions in the pore fluid extracted from the SRA mixture. Furthermore, the dropping in the proportion of $Q^2$ (1Al) for SRA mixtures, as revealed by NMR spectra, shows that a higher portion of Al precipitated in the form of Ht- phases in the presence of SRA. This suggests the formation of such voluminous crystals contributed to enhancing the stability of the matrix and thus, restraining the shrinkage, revealing the reason for Al reduction in the research by Palacios and Puertas, (2007). Hence, the retarding influence from SRA concerns hydrotalcite-like phase growth.

2. The main contribution of chapter 6 can be summarized as follow:

- The Micro-CT technique is a medical imaging technique that has showed great potential in evaluating the inner structure and the characteristics of the materials. The desorption mechanism of SAPs pores was successfully studied by X-ray tomography and showed an inside-out drying process.
- This work shed light on determining the suitable content rate of SAPs that should be used in the AAS system to attain specific performance levels and provides a benchmark for SAPs efficiency as an IC agent in AAS. A main goal of this thesis was achieved by efficiently mitigated the shrinkage of AAS while still maintaining high compressive strength.
- The absorption capacity of SAPs is highly dependent on the pore fluid composition (i.e., the concentration of divalent ions mainly $Ca^{2+}$) degree of SAPs cross-linking which mainly affects the osmotic pressure force, which subsequently influences the swelling capacity.
- Internal curing by SAPs was demonstrated to be a powerful mitigation strategy, especially when insufficient traditional curing was applied.

3. Chapter 7 of this thesis makes important observations which can be summarized as follow:

- The hydrophobic interactions between SRA and SAPs when applying both in the AAS system are significant, however, this was beyond the scope of this dissertation. This interesting phenomenon should be investigated further in other research.
- Imaging analysis is an appropriate and accurate method that was used to study the behavior of SAPs in AAS pore solution and pore solution with SRA by optical microscope images.
- The macro voids size distribution of the SAPs was evaluated by a novel method based on image analysis on cross-sections taken of AAS pastes by X-ray tomography, which revealed the macro voids in the hybrid AAS paste appeared to be smaller compared to the SAP paste without SRA.

- Investigations in this thesis prove that the potential chemical interaction between both SAPs and SRA influences the surface tension as well as the absorption/desorption process and that this combined influence mainly dependents on the content of each.
- The late addition of SRA to the AAS mixtures can be beneficial and does not alter the slag dissolution and the concentrations of the ions. However, more investigation is needed to confirm this behavior.
- The optimized combination of SRA and SAPs efficiently reduced the total shrinkage reaching that in OPC, while keeping the high strength. This goal was achieved by preparing AAS combined with SRA and the low content of SAP.

As an overall contribution, this thesis presented important results which enable determining the optimal designs for a particular application that contributes to a broader application of AAS.
It is expected that the results of this dissertation can be used as a basis for developing a model for shrinkage prediction of AAS.

## 8.3 Future research

Concerning the experimental work provided in this thesis, some considerable enhancements for future research are proposed:

- The sustainability of SRA application in AAS and how long SRA will take advantage of SRA application should be investigated. Therefore, the potential leaching risk of SRA and the potential impact on the long-run shrinkage behavior needs to be evaluated.
- Regarding SAPs incorporation in the AAS system, some points need further investigation. It should be considered that SAPs materials exhibited different chemical and physical properties which potentially influences their performance in AAS systems. Therefore, the effect of the type of SAPs, i.e., the composition of the SAPs and the chemical structure, length, and crosslinking degree of the SAP, which are thus important influences the efficiency and performance of SAPs.
- The research presented in this dissertation focuses on applying SAPs to provide IC effect. There is a necessity of performing advanced investigations on the effect of SAPs on the

durability and physical properties of AAS systems incorporated with SAPs. This can contribute to promoting the potential of SAP as an additive that improves the durability of AAS concrete over the entire life of the concrete.

- Particle size distribution and their shape significantly affect the properties of AAS, and so it is highly recommended to investigate the effect of SAPs produced by inverse suspension polymerization, which exhibits spherical shapes which are speculated to maintain high mechanical properties. On the other hand, this kind of SAP is expensive and not commercially available.
- The compatibility of SAPs and SRA was studied in this work; however, the chemical interaction of SAPs structures and SRA molecules needs to be further investigated.
- Desorption kinetics of SAPs in a hybrid AAS system is crucial which influences shrinkage mitigation. Thus, the liquid release mechanism in AAS pastes combining both SRA and SAP should be further investigated.
- An important observation was found concerning the addition time of SRA as it was found that adding SRA after the extraction of the pore solution doesn't change the alkalinity of the pore solution. This suggests that the potential retardation effect can be avoided by delaying the addition of SRA. Nevertheless, more intensive investigations should be considered to study the potential impact of this adding procedure on the efficiency of SRA in mitigating the shrinkage of AAS.
- It is recommended to study the possible adsorption behavior of SRA onto the hydrated AAS, which has a direct effect on its efficiency in mitigating shrinkage.
- The optimized inclusion of SAPs, SRA, and hybrid systems to eliminate autogenous shrinkage are of crucial importance that can help in avoiding the highly restrained cracking tendency in AAS. Thus, the cracking behavior of AAS when restrained is a subject that should be further researched.

# References


[1] Abdalqader AF, Jin F, Al-Tabbaa A. Development of greener alkali-activated cement: utilisation of sodium carbonate for activating slag and fly ash mixtures. Journal of Cleaner Production. 2016; 113:66-75.

[2] Adamson AW. The physical chemistry of surfaces. Abstracts of Papers of the American Chemical Society. 2001;221:U320-U.

[3] Al Makhadmeh Wa, Soliman A. Effect of activator nature on property development of alkali-activated slag binders. Journal of Sustainable Cement-Based Materials. 2020:1-17.

[4] Al Makhadmeh, Wala'a, and Soliman, Ahmed. A design of experiment approach to study the influence of waterglass parameters on the shrinkage of alkali-activated slag mortars, Accepted at 9th CSCE International Specialty Conference on Engineering Mechanics and Materials, Niagara Falls, Ontario, Canada, May 2021 .

[5] Al Makhadmeh W, Soliman AM. Effect of sodium oxide on the properties of alkali activated slag mortars. Proceedings of the Annual Conference - Canadian Society for Civil Engineering; Canadian Scociety for civil engineering, Pointe Claire, Quebec, Canada, June; 2019..

[6] Al Makhadmeh W, Soliman AM. Comparative analysis of reaction kinetics of one and two parts alkali activated slag. Proceedings of the Annual Conference - Canadian Society for Civil Engineering; Canadian Scociety for civil engineering, Pointe Claire, Quebec, Canada, June; 2019.

[7] Assmann A. Physical properties of concrete modified with superabsorbent polymers. 2013.

[8] ASTM C191. Standard test methods for the time of setting of hydraulic cement by Vicat needle. West Conshohocken (PA): Annual Book of ASTM Standards; 2005.

[9] ASTM C1679. Standard practice for measuring hydration kinetics of hydraulic cementitious mixtures using isothermal calorimetry. West Conshohocken (PA): ASTM International; 2017.

[10] ASTM C109 / C109M-20b, Standard Test Method for Compressive Strength of Hydraulic Cement Mortars (Using 2-in. or [50 mm] Cube Specimens), ASTM International, West Conshohocken, PA, 2020.

[11] Atiş CD, Bilim C, Çelik Ö, Karahan O. Influence of activator on the strength and drying shrinkage of alkali-activated slag mortar. Construction and building materials. 2009;23(1):548-55.

[12] B. Pease HS, Weiss J. Shrinkage Behavior and Residual Stress Development in Mortar Containing Shrinkage Reducing Admixtures (SRAs). ACI Symposium Publication.227.

[13] Babcock AE, Taylor P, editors. Impacts of Internal Curing on Concrete Properties2015.

[14] Badmann R, Stockhausen N, Setzer MJ. THE STATISTICAL THICKNESS AND THE CHEMICAL-POTENTIAL OF ADSORBED WATER FILMS. Journal of Colloid and Interface Science. 1981;82(2):534-42.

[15] Bakharev T, Sanjayan JG, Cheng YB. Effect of admixtures on properties of alkali-activated slag concrete. Cement and Concrete Research. 2000;30(9):1367-74.

[16] Bakharev T, Sanjayan JG, Cheng YB. Effect of elevated temperature curing on properties of alkali-activated slag concrete. Cement and Concrete Research. 1999;29(10):1619-25.

[17] Ballekere Kumarappa D, Peethamparan S, Ngami M. Autogenous shrinkage of alkali activated slag mortars: Basic mechanisms and mitigation methods. Cement and Concrete Research. 2018;109:1-9.
[18] Barrett EP, Joyner LG, Halenda PP. The Determination of Pore Volume and Area Distributions in Porous Substances. I. Computations from Nitrogen Isotherms. Journal of the American Chemical Society. 1951;73(1):373-80.
[19] Bazant ZP. MATHEMATICAL-MODEL FOR CREEP AND THERMAL SHRINKAGE OF CONCRETE AT HIGH-TEMPERATURE. Nuclear Engineering and Design. 1983;76(2):183-91.
[20] Behfarnia K, Rostami M. The Effect of Alkaline Solution-to-Slag Ratio on Permeability of Alkali Activated Slag Concrete. International Journal of Civil Engineering. 2018;16(8):897-904.
[21] Ben Haha M, Lothenbach B, Le Saout G, Winnefeld F. Influence of slag chemistry on the hydration of alkali-activated blast-furnace slag - Part II: Effect of Al2O3. Cement and Concrete Research. 2012;42(1):74-83.
[22] Bentur A, Igarashi S-i, Kovler K. Prevention of autogenous shrinkage in high-strength concrete by internal curing using wet lightweight aggregates. Cement and Concrete Research. 2001;31(11):1587-91.
[23] Bentz DP, Geiker MR, Hansen KK. Shrinkage-reducing admixtures and early-age desiccation in cement pastes and mortars. Cement and Concrete Research. 2001;31(7):1075-85.
[24] Bentz DP, Snyder KA. Protected paste volume in concrete - Extension to internal curing using saturated lightweight fine aggregate. Cement and Concrete Research. 1999;29(11):1863-7.
[25] Bernal SA, Mejía de Gutiérrez R, Provis JL. Engineering and durability properties of concretes based on alkali-activated granulated blast furnace slag/metakaolin blends. Construction and Building Materials. 2012;33:99-108
[26] Beushausen H, Gillmer M, Alexander M. The influence of superabsorbent polymers on strength and durability properties of blended cement mortars. Cement and Concrete Composites. 2014;52:73-80.
[27] Bílek V, Kalina L, Novotný R. Polyethylene glycol molecular weight as an important parameter affecting drying shrinkage and hydration of alkali-activated slag mortars and pastes. Construction and Building Materials. 2018;166:564-71.
[28] Bostrom M, Williams DRM, Ninham BW. Surface tension of electrolytes: Specific ion effects explained by dispersion forces. Langmuir. 2001;17(15):4475-8.
[29] Brough AR, Atkinson A. Sodium silicate-based, alkali-activated slag mortars Part I. Strength, hydration and microstructure. Cement and Concrete Research. 2002;32(6):865-79.
[30] Brunauer S, Emmett PH, Teller E. Adsorption of gases in multimolecular layers. Journal of the American chemical society. 1938;60(2):309-19.
[31] Buchholz and Graham, Modern Superabsorbent Polymer Technology, John Wiley & Sons, 1998.
[32] Cartwright C, Rajabipour F, Radlińska A. Shrinkage characteristics of alkali-activated slag cements. Journal of materials in civil engineering. 2015;27(7):B4014007.
[33] Chen W, Brouwers HJH. The hydration of slag, part 1: reaction models for alkali-activated slag. Journal of Materials Science. 2007;42(2):428-43.
[34] Chen W, Li B, Wang J, Thom N. Effects of alkali dosage and silicate modulus on autogenous shrinkage of alkali-activated slag cement paste. Cement and Concrete Research. 2021;141:106322.

[35] Chung S-Y, Kim J-S, Stephan D, Han T-S. Overview of the use of micro-computed tomography (micro-CT) to investigate the relation between the material characteristics and properties of cement-based materials. Construction and Building Materials. 2019;229:116843.
[36] Collins F, Sanjayan JG. Effect of pore size distribution on drying shrinking of alkali-activated slag concrete. Cement and Concrete Research. 2000;30(9):1401-6.
[37] Collins F, Sanjayan JG. Strength and shrinkage properties of alkali-activated slag concrete containing porous coarse aggregate. Cement and Concrete Research. 1999a;29(4):607-10.
[38] Collins FG, Sanjayan JG. Workability and mechanical properties of alkali activated slag concrete. Cement and Concrete Research. 1999b;29(3):455-8.
[39] de Sensale GR, Ribeiro AB, Gonçalves A. Effects of RHA on autogenous shrinkage of Portland cement pastes. Cement and Concrete Composites. 2008;30(10):892-7.
[40] Dudziak L, Mechtcherine V. Mitigation of volume changes of ultra-high performance concrete (UHPC) by using super absorbent polymers. Ultra High Performance Concrete (UHPC) Second International Symposium on Ultra High Performance Concrete. 2008:425-32.
[41] Eberhardt AB. On the mechanisms of shrinkage reducing admixtures in self con-solidating mortars and concretes 2011.
[42] Farzanian K, Pimenta Teixeira K, Perdigão Rocha I, De Sa Carneiro L, Ghahremaninezhad A. The mechanical strength, degree of hydration, and electrical resistivity of cement pastes modified with superabsorbent polymers. Construction and Building Materials. 2016;109:156-65.
[43] Fazhou Wang YZBPZL, Shuguang H. Autogenous Shrinkage of Concrete with Super-Absorbent Polymer. ACI Materials Journal.106(2).
[44] Feneuil B, Pitois O, Roussel N. Effect of surfactants on the yield stress of cement paste. Cement and Concrete Research. 2017;100:32-9.
[45] Feng X, Garboczi EJ, Bentz DP, Stutzman PE, Mason TO. Estimation of the degree of hydration of blended cement pastes by a scanning electron microscope point-counting procedure. Cement and Concrete Research. 2004;34(10):1787-93.
[46] FernandezJimenez A, Puertas F. Alkali-activated slag cements: Kinetic studies. Cement and Concrete Research. 1997;27(3):359-68.
[47] Fernandez-Jimenez A, Puertas F. Setting of alkali-activated slag cement. Influence of activator nature. Advances in Cement Research. 2001;13(3):115-21.
[48] Ferraris CF, Wittmann FH. SHRINKAGE MECHANISMS OF HARDENED CEMENT PASTE. Cement and Concrete Research. 1987;17(3):453-64.
[49] Franks F, Pedley M, Reid DS. Solute interactions in dilute aqueous solutions. Part 1.—Microcalorimetric study of the hydrophobic interaction. Journal of the Chemical Society, Faraday Transactions 1: Physical Chemistry in Condensed Phases. 1976;72(0):359-67.
[50] Gagné R. 23 - Shrinkage-reducing admixtures. In: Aïtcin P-C, Flatt RJ, editors. Science and Technology of Concrete Admixtures: Woodhead Publishing; 2016. p. 457-69.
[51] Gardner NJ, Weiss W, American Concrete I, Spring C. Shrinkage and creep of concrete. Farmington Hills, Mich.: American Concrete Institute; 2005.
[52] Garnier S. Novel amphiphilic diblock copolymers by RAFT-polymerization, their self-organization and surfactant properties. 2005.
[53] Ghafari E, Ghahari SA, Costa H, Julio E, Portugal A, Duraes L. Effect of supplementary cementitious materials on autogenous shrinkage of ultra-high performance concrete. Construction and Building Materials. 2016;127:43-8.

[54] Guzmán E, Llamas S, Maestro A, Fernández-Peña L, Akanno A, Miller R, et al. Polymer-surfactant systems in bulk and at fluid interfaces. Adv Colloid Interface Sci. 2016;233:38-64.
[55] Han YD, Zhang J, Luosun YM, Hao TY. Effect of internal curing on internal relative humidity and shrinkage of high strength concrete slabs. Construction and Building Materials. 2014;61:41-9.
[56] Hasholt MT, Jensen OM. Chloride migration in concrete with superabsorbent polymers. Cement and Concrete Composites. 2015;55:290-7.
[57] Hasholt MT, Jensen OM, Kovler K, Zhutovsky S. Can superabsorent polymers mitigate autogenous shrinkage of internally cured concrete without compromising the strength? Construction and Building Materials. 2012;31:226-30.
[58] Henkensiefken R, Nantung T, Weiss W, editors. Reducing Restrained Shrinkage Cracking in Concrete: Examining the Behavior of Self-Curing Concrete Made using Different Volumes of Saturated Lightweight Aggregate2008.
[59] Hu X, Shi C, Zhang Z, Hu Z. Autogenous and drying shrinkage of alkali-activated slag mortars. Journal of the American Ceramic Society. 2019;102(8):4963-75.
[60] Ismail I, Bernal SA, Provis JL, Hamdan S, van Deventer JSJ. Drying-induced changes in the structure of alkali-activated pastes. Journal of Materials Science. 2013;48(9):3566-77.
[61] Israelachvili J, Pashley R. The hydrophobic interaction is long range, decaying exponentially with distance. Nature. 1982;300(5890):341-2.
[62] Jang JG, Lee NK, Lee HK. Fresh and hardened properties of alkali-activated fly ash/slag pastes with superplasticizers. Construction and Building Materials. 2014;50:169-76.
[63] Jensen OM, Hansen PF. Water-entrained cement-based materials: I. Principles and theoretical background. Cement and Concrete Research. 2001;31(4):647-54.
[64] Jensen OM, Lura P. Techniques and materials for internal water curing of concrete. Materials and Structures. 2006;39(9):817-25.
[65] Jia Z, Yang Y, Yang L, Zhang Y, Sun Z. Hydration products, internal relative humidity and drying shrinkage of alkali activated slag mortar with expansion agents. Construction and Building Materials. 2018;158:198-207.
[66] Jin F, Gu K, Al-Tabbaa A. Strength and drying shrinkage of reactive MgO modified alkali-activated slag paste. Construction and Building Materials. 2014;51:395-404.
[67] Joyner LG, Barrett EP, Skold R. The Determination of Pore Volume and Area Distributions in Porous Substances. II. Comparison between Nitrogen Isotherm and Mercury Porosimeter Methods. Journal of the American Chemical Society. 1951;73:3155-8.
[68] Justs J, Wyrzykowski M, Bajare D, Lura P. Internal curing by superabsorbent polymers in ultra-high performance concrete. Cement and Concrete Research. 2015;76:82-90.
[69] Justs J, Wyrzykowski M, Winnefeld F, Bajare D, Lura P. Influence of superabsorbent polymers on hydration of cement pastes with low water-to-binder ratio. Journal of Thermal Analysis and Calorimetry. 2014;115(1):425-32.
[70] Kang S-H, Hong S-G, Moon J. Absorption kinetics of superabsorbent polymers (SAP) in various cement-based solutions. Cement and Concrete Research. 2017;97:73-83.
[71] Kumar R, Bhattacharjee B. Study on some factors affecting the results in the use of MIP method in concrete research. Cement and Concrete Research. 2003;33(3):417-24.
[72] Kumarappa DB, Peethamparan S, Ngami M. Autogenous shrinkage of alkali activated slag mortars: Basic mechanisms and mitigation methods. Cement and Concrete Research. 2018;109:1-9.

[73] Kutti T. Hydration products of alkaliactivated slag. Proceedings of the 9th International on Congress on the Chemistry of Cement; New Delhi; 1992. p. 468–474.
[74] Lee HXD, Wong HS, Buenfeld NR. Potential of superabsorbent polymer for self-sealing cracks in concrete. Advances in Applied Ceramics. 2010;109(5):296-302.
[75] Li Z, Lu T, Liang X, Dong H, Ye G. Mechanisms of autogenous shrinkage of alkali-activated slag and fly ash pastes. Cement and Concrete Research. 2020;135:106107.
[76] Li Z, Nedeljković M, Chen B, Ye G. Mitigating the autogenous shrinkage of alkali-activated slag by metakaolin. Cement and Concrete Research. 2019;122:30-41.
[77] Li Z, Nedeljkovic M, Zuo Y, Ye G, editors. Autogenous shrinkage of alkali-activated slag-fly ash pastes. Proceedings of the 5th International Slag Valorisation Symposium, Leuven, Belgium; 2017.
[78] Li Z, Wyrzykowski M, Dong H, Granja J, Azenha M, Lura P, et al. Internal curing by superabsorbent polymers in alkali-activated slag. Cement and Concrete Research. 2020;135:106123.
[79] Li Z, Zhang S, Liang X, Granja J, Azenha M, Ye G. Internal curing of alkali-activated slag-fly ash paste with superabsorbent polymers. Construction and Building Materials. 2020;263:120985.
[80] Li Z, Zhang S, Liang X, Ye G. Cracking potential of alkali-activated slag and fly ash concrete subjected to restrained autogenous shrinkage. Cement and Concrete Composites. 2020;114:103767.
[81] Litvan GG. Variability of the nitrogen surface area of hydrated cement paste. Cement and Concrete Research. 1976;6(1):139-43.
[82] Liu J, Shi C, Ma X, Khayat KH, Zhang J, Wang D. An overview on the effect of internal curing on shrinkage of high performance cement-based materials. Construction and Building Materials. 2017;146:702-12
[83] Liu Z, Rempel G. Preparation of superabsorbent polymers by crosslinking acrylic acid and acrylamide copolymers. Journal of Applied Polymer Science. 1997;64:1345-53.
[84] Lura P. Compressive strength of cement pastes and mortars with superabsorbent polymers2006. 117-25 p.
[85] Lura P, Bisschop J. On the origin of eigenstresses in lightweight aggregate concrete. Cement and Concrete Composites. 2004;26(5):445-52.
[86] Lura P, Durand F, Jensen OM, editors. Autogenous strain of cement pastes with superabsorbent polymers. International RILEM conference on volume changes of hardening concrete: testing and mitigation; 2006: RILEM Publications SARL.
[87] Lura P, Durand F, Jensen OM. Autogenous strain of cement pastes with superabsorbent polymers. RILEM Proc PRO 52, Volume Changes of Hardening Concrete: Testing and Mitigation. 2006:57-65.
[88] Lura P, Pease B, Mazzotta GB, Rajabipour F, Weiss J. Influence of shrinkage-reducing admixtures on development of plastic shrinkage cracks. Aci Materials Journal. 2007;104(2):187-94.
[89] Luukkonen T, Abdollahnejad Z, Yliniemi J, Kinnunen P, Illikainen M. One-part alkali-activated materials: A review. Cement and Concrete Research. 2018;103:21-34.
[90] Ma X, Liu J, Shi C. Effects of SAP on the properties and pore structure of high performance cement-based materials. Construction and Building Materials. 2017;131:476-84.

[91] Mayfield B. CREEP AND SHRINKAGE IN CONCRETE STRUCTURES - BAZANT,ZP, WITTMAN,FH. Earthquake Engineering & Structural Dynamics. 1983;11(4):591-2.
[92] Mechtcherine V, Dudziak L, Hempel S. Mitigating early age shrinkage of Ultra-High Performance Concrete by using Super Absorbent Polymers (SAP). 2008:847-53.
[93] Mechtcherine V, Gorges M, Schroefl C, Assmann A, Brameshuber W, Ribeiro AB, et al. Effect of internal curing by using superabsorbent polymers (SAP) on autogenous shrinkage and other properties of a high-performance fine-grained concrete: results of a RILEM round-robin test. Materials and Structures. 2014;47(3):541-62.
[94] Mehta PK, Monteiro PJ. Concrete: microstructure, properties, and materials: McGraw-Hill Education; 2014.
[95] Neto AAM, Cincotto MA, Repette W. Drying and autogenous shrinkage of pastes and mortars with activated slag cement. Cement and Concrete Research. 2008;38(4):565-74.
[96] Nmai C, Tomita R, Hondo F, Buffenbarger J. Shrinkage-reducing admixtures. Concrete International. 1998;20:31-7.
[97] Nylander T, Samoshina Y, Lindman B. Formation of polyelectrolyte–surfactant complexes on surfaces. Advances in Colloid and Interface Science. 2006;123-126:105-23.
[98] Oh S, Choi YC. Superabsorbent polymers as internal curing agents in alkali activated slag mortars. Construction and Building Materials. 2018;159:1-8.
[99] P. Kumar Mehta PD, Paulo J. M. Monteiro PD. Concrete: Microstructure, Properties, and Materials, Fourth Edition. 4th ed. ed. New York: McGraw-Hill Education; 2014.
[100] Pacheco-Torgal F, Castro-Gomes J, Jalali S. Alkali-activated binders: A review. Part 2. About materials and binders manufacture. Construction and Building Materials. 2008;22(7):1315-22.
[101] Palacios M, Puertas F. Effect of shrinkage-reducing admixtures on the properties of alkali-activated slag mortars and pastes. Cement and Concrete Research. 2007;37(5):691-702.
[102] Pourjavadi A, Fakoorpoor SM, Hosseini P, Khaloo A. Interactions between superabsorbent polymers and cement-based composites incorporating colloidal silica nanoparticles. Cement and Concrete Composites. 2013;37:196-204.
[103] Powers T, editor Mechanisms of Shrinkage and Reversible Creep of Hardened Cement Paste, The Structure of Concrete1965.
[104] Powers TC, Brownyard TL. Studies of the Physical Properties of Hardened Portland Cement Paste. ACI Journal Proceedings.43(9).
[105] Provis JL, van Deventer JSJ. Geopolymerisation kinetics. 2. Reaction kinetic modelling. Chemical Engineering Science. 2007;62(9):2318-29.
[106] Puertas F, Fernández-Jiménez A, Blanco-Varela MT. Pore solution in alkali-activated slag cement pastes. Relation to the composition and structure of calcium silicate hydrate. Cement and Concrete Research. 2004;34(1):139-48.
[107] Rajabipour F, Sant G, Weiss J. Interactions between shrinkage reducing admixtures (SRA) and cement paste's pore solution. Cement and Concrete Research. 2008;38(5):606-15.
[108] Ranaivomanana H, Verdier J, Sellier A, Bourbon X. Toward a better comprehension and modeling of hysteresis cycles in the water sorption-desorption process for cement based materials. Cement and Concrete Research. 2011;41(8):817-27.
[109] Ravikumar D, Neithalath N. Reaction kinetics in sodium silicate powder and liquid activated slag binders evaluated using isothermal calorimetry. Thermochimica Acta. 2012;546:32-43.

[110] Renaudin G, Russias J, Leroux F, Cau-dit-Coumes C, Frizon F. Structural characterization of C s H and c A s H samples Part II: Local environment investigated by spectroscopic analyses. Journal of Solid State Chemistry. 2009;182:3320-9.
[111] Richardson I, Brough A, Brydson R, Groves GW, Dobson C. Location of Aluminum in Substituted Calcium Silicate Hydrate (c S H) Gels as Determined by 29Si and 27Al NMR and EELS. Journal of the American Ceramic Society. 1993;76:2285-8.
[112] Richardson IG, Groves GW. The structure of the calcium silicate hydrate phases present in hardened pastes of white Portland cement blast-furnace slag blends. Journal of Materials Science. 1997;32(18):4793-802.
[113] Richter A, Paschew G, Klatt S, Lienig J, Arndt K-F, Adler H-JP. Review on Hydrogel-based pH Sensors and Microsensors. Sensors. 2008;8(1):561-81.
[114] Ries HE. Physical Chemistry of Surfaces. Journal of the American Chemical Society. 1961;83(8):2028-9.
[115] Rongbing B, Jian S. Synthesis and evaluation of shrinkage-reducing admixture for cementitious materials. Cement and Concrete Research. 2005;35(3):445-8.
[116] Sakulich AR, Bentz DP. Mitigation of autogenous shrinkage in alkali activated slag mortars by internal curing. Materials and structures. 2013;46(8):1355-67.
[117] Schröfl C, Mechtcherine V, Gorges M. Relation between the molecular structure and the efficiency of superabsorbent polymers (SAP) as concrete admixture to mitigate autogenous shrinkage. Cement and Concrete Research. 2012;42(6):865-73.
[118] Schröfl C, Snoeck D, Mechtcherine V. A review of characterisation methods for superabsorbent polymer (SAP) samples to be used in cement-based construction materials: report of the RILEM TC 260-RSC. Materials and Structures. 2017;50(4):197.
[119] Schröfl C, Snoeck D, Mechtcherine V. A review of characterisation methods for superabsorbent polymer (SAP) samples to be used in cement-based construction materials: report of the RILEM TC 260-RSC. Materials and Structures. 2017;50(4):197.
[120] Schulz SG. The phase behavior of amphiphilic surfactants and polymers: A dissipative particles dynamics study: Dissertation, Essen, University of Duisburg-Essen; 2004.
[121] Scrivener K, Snellings, R., & Lothenbach, B. (Eds.). . A Practical Guide to Microstructural Analysis of Cementitious Materials (1st ed.). CRC Press. . 2016.
[122] Shen D, Wang X, Cheng D, Zhang J, Jiang G. Effect of internal curing with super absorbent polymers on autogenous shrinkage of concrete at early age. Construction and Building Materials. 2016;106:512-22.
[123] Shi C. Strength, pore structure and permeability of alkali-activated slag mortars. Cement and Concrete Research. 1996;26(12):1789-99.
[124] Shi CJ, Day RL. A CALORIMETRIC STUDY OF EARLY HYDRATION OF ALKALI-SLAG CEMENTS. Cement and Concrete Research. 1995;25(6):1333-46.
[125] Shoya M, Sugita S, Sugawara T, editors. IMPROVEMENT OF DRYING SHRINKAGE AND SHRINKAGE CRACKING OF CONCRETE BY SPECIAL SURFACTANTS. International Symp on Admixtures for Concrete : Improvement of Properties; 1990 May 14-17; Barcelona, Spain1990.
[126] Skibsted J, Andersen MD. The Effect of Alkali Ions on the Incorporation of Aluminum in the Calcium Silicate Hydrate (C-S-H) Phase Resulting from Portland Cement Hydration Studied by Si-29 MAS NMR. Journal of the American Ceramic Society. 2013;96(2):651-6.

[127] Snoeck D, Jensen OM, De Belie N. The influence of superabsorbent polymers on the autogenous shrinkage properties of cement pastes with supplementary cementitious materials. Cement and Concrete Research. 2015;74:59-67.
[128] Snoeck D, Schaubroeck D, Dubruel P, De Belie N. Effect of high amounts of superabsorbent polymers and additional water on the workability, microstructure and strength of mortars with a water-to-cement ratio of 0.50. Construction and Building Materials. 2014;72:148-57.
[129] Snoeck D, Steuperaert S, Van Tittelboom K, Dubruel P, De Belie N. Visualization of water penetration in cementitious materials with superabsorbent polymers by means of neutron radiography. Cement and Concrete Research. 2012;42(8):1113-21.
[130] Snyder KA, Feng X, Keen BD, Mason TO. Estimating the electrical conductivity of cement paste pore solutions from OH−, K+ and Na+ concentrations. Cement and Concrete Research. 2003;33(6):793-8.
[131] Song C, Choi YC, Choi S. Effect of internal curing by superabsorbent polymers – Internal relative humidity and autogenous shrinkage of alkali-activated slag mortars. Construction and Building Materials. 2016;123:198-206.
[132] Song C, Choi YC, Choi S. Effect of internal curing by superabsorbent polymers – Internal relative humidity and autogenous shrinkage of alkali-activated slag mortars. Construction and Building Materials. 2016;123:198-206.
[133] Stefan L, Boulay C, Torrenti J-M, Bissonnette B, Benboudjema F. Influential factors in volume change measurements for cementitious materials at early ages and in isothermal conditions. Cement and Concrete Composites. 2018;85:105-21.
[134] Thomas JJ, Jennings HM. A colloidal interpretation of chemical aging of the C-S-H gel and its effects on the properties of cement paste. Cement and Concrete Research. 2006;36(1):30-8.
[135] Thomas RJ, Lezama D, Peethamparan S. On drying shrinkage in alkali-activated concrete: Improving dimensional stability by aging or heat-curing. Cement and Concrete Research. 2017;91:13-23.
[136] Underwood E. Stereology, or the quantitative evaluation of microstructures. Journal of microscopy. 1969;89(2):161-80.
[137] Wang S-D, Scrivener KL. 29Si and 27Al NMR study of alkali-activated slag. Cement and Concrete Research. 2003;33(5):769-74.
[138] Wang S-D, Scrivener KL. Hydration products of alkali activated slag cement. Cement and Concrete Research. 1995;25(3):561-71.
[139] Wattebled L. Oligomeric surfactants as novel type of amphiphiles: structure-property relationships and behaviour with additives. 2006.
[140] Wehbe Y, Ghahremaninezhad A. Combined effect of shrinkage reducing admixtures (SRA) and superabsorbent polymers (SAP) on the autogenous shrinkage, hydration and properties of cementitious materials. Construction and Building Materials. 2017;138:151-62.
[141] Wyrzykowski M, Lura P. Effect of relative humidity decrease due to self-desiccation on the hydration kinetics of cement. Cement and Concrete Research. 2016;85:75-81.
[142] Ye G. Experimental Study and Numerical Simulation of the Development of the Microstructure and Permeability of Cementitious Materials. 2003.
[143] Ye H, Radlińska A. Shrinkage mechanisms of alkali-activated slag. Cement and Concrete Research. 2016a;88:126-35.

[144] Ye HL, Radlinska A. A Review and Comparative Study of Existing Shrinkage Prediction Models for Portland and Non-Portland Cementitious Materials. Advances in Materials Science and Engineering. 2016b.
[145] Ye H, Radlińska A. Shrinkage mitigation strategies in alkali-activated slag. Cement and Concrete Research. 2017;101:131-43.
[146] Ye HL, Radlinska A. Quantitative Analysis of Phase Assemblage and Chemical Shrinkage of Alkali-Activated Slag. Journal of Advanced Concrete Technology. 2016;14(5):245-60.
[147] Yuan B, Yu QL, Brouwers HJH. Reaction kinetics, reaction products and compressive strength of ternary activators activated slag designed by Taguchi method. Materials & Design. 2015;86:878-86.
[148] ZANA R. Introduction to surfactants and surfactant self-assemblies. Dynamics of Surfactant Self-Assemblies: CRC Press; 2005. p. 18-52.
[149] Zhang T, Yu Q, Wei J, Gao P, Zhang P. Study on optimization of hydration process of blended cement. Journal of Thermal Analysis and Calorimetry - J THERM ANAL CALORIM. 2012;107.
[150] Zhutovsky S, Kovler K. Hydration kinetics of high-performance cementitious systems under different curing conditions. Materials and Structures. 2013;46(10):1599-611.
[151] Zhutovsky S, Kovler K. Influence of water to cement ratio on the efficiency of internal curing of high-performance concrete. Construction and Building Materials. 2017;144:311-6.
[152] Altan E, Erdogan ST. Alkali activation of a slag at ambient and elevated temperatures. Cement & Concrete Composites. 2012;34(2):131-9.
[153] Alvarez-Ayuso E, Querol X, Plana F, Alastuey A, Moreno N, Izquierdo M, et al. Environmental, physical and structural characterisation of geopolymer matrixes synthesised from coal (co-)combustion fly ashes. Journal of Hazardous Materials. 2008;154(1-3):175-83.
[154] Aydin S, Baradan B. Effect of activator type and content on properties of alkali-activated slag mortars. Composites Part B-Engineering. 2014;57:166-72.
[155] Bakharev T. Durability of geopolymer materials in sodium and magnesium sulfate solutions. Cement and Concrete Research. 2005;35(6):1233-46.
[156] Ben Haha M, Le Saout G, Winnefeld F, Lothenbach B. Influence of activator type on hydration kinetics, hydrate assemblage and microstructural development of alkali activated blast-furnace slags. Cement and Concrete Research. 2011;41(3):301-10.
[157] Bernal SA, de Gutierrez RM, Provis JL. Engineering and durability properties of concretes based on alkali-activated granulated blast furnace slag/metakaolin blends. Construction and Building Materials. 2012;33:99-108.
[158] Brough AR, Atkinson A. Sodium silicate-based, alkali-activated slag mortars Part I. Strength, hydration and microstructure. Cement and Concrete Research. 2002;32(6):865-79.
[159] Chang JJ. A study on the setting characteristics of sodium silicate-activated slag pastes. Cement and Concrete Research. 2003;33(7):1005-11.
[160] Chen W, Brouwers HJH. The hydration of slag, part 1: reaction models for alkali-activated slag. Journal of Materials Science. 2007;42(2):428-43.
[161] Davidovits J. GEOPOLYMERS AND GEOPOLYMERIC MATERIALS. Journal of Thermal Analysis. 1989;35(2):429-41.
[162] El-Hassan H, Ismail N. Effect of process parameters on the performance of fly ash/GGBS blended geopolymer composites. Journal of Sustainable Cement-Based Materials. 2018;7(2):122-40.

[163] Escalante-Garcia JI, Fuentes AF, Gorokhovsky A, Fraire-Luna PE, Mendoza-Suarez G. Hydration products and reactivity of blast-furnace slag activated by various alkalis. Journal of the American Ceramic Society. 2003;86(12):2148-53.
[164] Fang GH, Bahrami H, Zhang MZ. Mechanisms of autogenous shrinkage of alkali-activated fly ash-slag pastes cured at ambient temperature within 24 h. Construction and Building Materials. 2018;171:377-87.
[165] FernandezJimenez A, Puertas F. Alkali-activated slag cements: Kinetic studies. Cement and Concrete Research. 1997;27(3):359-68.
[166] Gao X, Yu QL, Brouwers HJH. Assessing the porosity and shrinkage of alkali activated slag-fly ash composites designed applying a packing model. Construction and Building Materials. 2016;119:175-84.
[167] Gorhan G. The evaluation with anova of the effect of lime admixture and thermal cure time on fly ash paste activated with sodium silicate solution. Construction and Building Materials. 2015;94:228-
[168] Krizan D, Zivanovic B. Effects of dosage and modulus of water glass on early hydration of alkali-slag cements. Cement and Concrete Research. 2002;32(8):1181-8.
[169] Li N, Shi CJ, Zhang ZH. Understanding the roles of activators towards setting and hardening control of alkali-activated slag cement. Composites Part B-Engineering. 2019;171:34-45.
[170] Li YP, Shen L, Mirmoghtadaei R, Ai L. A Design of Experiment Approach to Study the Effects of Raw Material on the Performance of Geopolymer Concrete. Advances in Civil Engineering Materials. 2017;6(1):526-49.
[171] McLellan BC, Williams RP, Lay J, van Riessen A, Corder GD. Costs and carbon emissions for geopolymer pastes in comparison to ordinary portland cement. Journal of Cleaner Production. 2011;19(9-10):1080-90.
[172] Mohammed BS, Fang OC, Hossain KMA, Lachemi M. Mix proportioning of concrete containing paper mill residuals using response surface methodology. Construction and Building Materials. 2012;35:63-8.
[173] Radlinska A, Rajabipour F, Bucher B, Henkensiefken R, Sant G, Weiss J. Shrinkage Mitigation Strategies in Cementitious Systems A Closer Look at Differences in Sealed and Unsealed Behavior. Transportation Research Record. 2008(2070):59-67.
[174] Ravikumar D, Neithalath N. Reaction kinetics in sodium silicate powder and liquid activated slag binders evaluated using isothermal calorimetry. Thermochimica Acta. 2012;546:32-43.
[175] Sarker PK, Kelly S, Yao ZT. Effect of fire exposure on cracking, spalling and residual strength of fly ash geopolymer concrete. Materials & Design. 2014;63:584-92.
[176] Shi CJ. Strength, pore structure and permeability of alkali-activated slag mortars. Cement and Concrete Research. 1996;26(12):1789-99.
[177] Sindhunata, van Deventer JSJ, Lukey GC, Xu H. Effect of curing temperature and silicate concentration on fly-ash-based geopolymerization. Industrial & Engineering Chemistry Research. 2006;45(10):3559-68.
[178] Song S, Sohn D, Jennings HM, Mason TO. Hydration of alkali-activated ground granulated blast furnace slag. Journal of Materials Science. 2000;35(1):249-57.
[179] Thomas RJ, Lezama D, Peethamparan S. On drying shrinkage in alkali-activated concrete: Improving dimensional stability by aging or heat-curing. Cement and Concrete Research. 2017;91:13-23.

[180] Turner LK, Collins FG. Carbon dioxide equivalent (CO2-e) emissions: A comparison between geopolymer and OPC cement concrete. Construction and Building Materials. 2013;43:125-30.
[181] Wang GS, Ma YW. Drying shrinkage of alkali-activated fly ash/slag blended system. Journal of Sustainable Cement-Based Materials. 2018;7(4):203-13.
[182] Wang SD, Scrivener KL, Pratt PL. FACTORS AFFECTING THE STRENGTH OF ALKALI-ACTIVATED
[183] Yip CK, Lukey GC, van Deventer JSJ. The coexistence of geopolymeric gel and calcium silicate hydrate at the early stage of alkaline activation. Cement and Concrete Research. 2005;35(9):1688-97.
[184] Yip CK, Van Deventer JSJ. Microanalysis of calcium silicate hydrate gel formed within a geopolymeric binder. Journal of Materials Science. 2003;38(18):3851-60.
[185] Turner LK, Collins FG. Carbon dioxide equivalent (CO2-e) emissions: a com[1]parison between geopolymer and OPC cement concrete. Constr Build Mater. 2013; 43:125–130
[186] Bilim C, Karahan O, Atis CD, Ilkentapar S. Influence of admixtures on the properties of alkali-activated slag mortars subjected to different curing conditions. Materials & Design. 2013;44:540-7.
[187] Ye HL, Radlinska A. Effect of Alkalis on Cementitious Materials: Understanding the Relationship between Composition, Structure, and Volume Change Mechanism. Journal of Advanced Concrete Technology. 2017;15(4):165-77.
[188] Yuan XH, Chen W, Lu ZA, Chen HG. Shrinkage compensation of alkali-activated slag concrete and microstructural analysis. Construction and Building Materials. 2014;66:422-8.
[189] Zhang R, Cheng X, Hou PK, Ye ZM. Influences of nano-TiO2 on the properties of cement-based materials: Hydration and drying shrinkage. Construction and Building Materials. 2015;81:35-41.